AN ABSTRACT OF THE DISSERTATION OF

Ross Mitchell Warner for the degree of Doctor of Philosophy in Chemical Engineering presented on November 19, 2020.

Title: Mathematical and Experimental Approaches for Designing Less Toxic Cryopreservation Methods

Abstract approved:

Adam Z. Higgins

Successful cryopreservation of all biological specimens would have an untold positive impact on medicine and scientific research. However, cryopreservation of the most complex biological specimens, such as tissues and organs, remains elusive. Vitrification, or ice-free cryopreservation, is promising for cryopreservation of complex specimens. The biggest challenge, though, is the toxicity imparted by the large concentration of cryoprotectant(s) (CPAs) required to suppress ice formation. There are several approaches to overcome toxicity that have been proposed in the field, but our group has proposed the use of mathematical modeling to minimize toxicity. The optimization strategy revolves around design of a vitrification protocol that minimizes the toxicity cost function. In a previous work, this approach was used to identify a vitrification protocol using glycerol as the CPA that was less toxic for endothelial cells when compared to conventional protocols used in the field. This previous work serves as a foundation for the current work presented here, which seeks to expand the utility of the toxicity cost function approach. In the first research chapter of this work, an automated liquid handling methodology is proposed to characterize CPA toxicity, and five of the most common CPAs and their binary and ternary combinations are characterized. This approach lays the foundation for future high-throughput screening of CPA toxicity, and the data set that was obtained will inform future models for predicting the toxicity of multi-CPA mixtures. To apply the toxicity cost function approach to tissues and organs, more complicated mass transfer models are required to predict the flow of CPAs and calculate the toxicity imparted. In the second research chapter of this work, a general mass transfer model is proposed for tissues. This model augments an acellular cartilage-based model in the literature by adding cells and accounting for their effects on mass transfer within tissues. We show that this modeling approach is applicable to the two very different tissues of cartilage and pancreatic islets. Moving to the organ regime and the third and final research chapter of this work, mass transfer within kidneys is investigated. Specifically, slaughterhouse porcine kidneys are perfused with various CPA solutions and the overall mass response is compared to that of a single cell. Also, an experimental method is proposed to measure the CPA concentration within the kidney as a function of space and time using computed tomography (CT). Another experimental method utilizing a lactate dehydrogenase (LDH) assay is also proposed that could measure damage imparted from CPA addition and removal. The third research chapter provides a basis for informing organ-based mass transfer models in the future. Overall, it is the hope that the chapters of this work provide a solid foundation for future research of furthering the toxicity cost function approach within all specimen regimes of cryopreservation.

Mathematical and Experimental Approaches for Designing Less Toxic Cryopreservation Methods

by
Ross Mitchell Warner

A DISSERTATION

submitted to

Oregon State University

in partial fulfillment of
the requirements for the
degree of

Doctor of Philosophy

Presented November 19, 2020
Commencement June 2021

Doctor of Philosophy dissertation of Ross Mitchell Warner presented on November 19, 2020

APPROVED:

Major Professor, representing Chemical Engineering

Head of the School of Chemical, Biological, and Environmental Engineering

Dean of the Graduate School

I understand that my dissertation will become part of the permanent collection of Oregon State University libraries. My signature below authorizes release of my dissertation to any reader upon request.

Ross Mitchell Warner, Author

ACKNOWLEDGEMENTS

I would like to thank my advisor, Dr. Adam Higgins, for countless hours of good discussions. His guidance kept me on track, and I owe many thanks to him for my professional development. I believe we accomplished good work and were able to share it with the cryobiology community.

I would also like to thank those that helped me accomplish lab work. Thank you Jun Yang, Andrew Drake, and Youngjoo Lee for driving with me across the Willamette Valley and harvesting porcine kidneys from numerous sources. To Stanton's Slaughter House and Mohawk Valley Meats, thank you for accommodating my acquisition of porcine kidneys, as well as the Pacific Northwest Transplant Bank allowing me to acquire human kidneys. I am also very grateful for the help I received at the Oregon State University College of Veterinary Medicine. The help of Dr. Sarah Nemanic, Jason Wiest, and Cynthia Viramontes was instrumental in conducting the CT experiments of porcine kidneys. For my high throughput screening work, I am indebted to Dylan Nelson who helped me become a proficient operator of the liquid handler. I am also very much indebted to Emi Ampo who helped facilitate the experimental work of the high throughput screening project.

Thank you to my committee members: Dr. Joe Baio, Dr. Kate Schilke, Dr. Brian Wood, and Dr. Frank Chaplen. My discussions with Dr. Brian Wood about transport modeling were truly insightful.

The Johnson Hall third floor group provided great conversations and always made the best group to go to lunch with.

Finally, I would like to thank my parents, Steve and Brenda Warner, for their unwavering support during my graduate school experience. My weekly phone calls with them were always a bright spot during the week. Last but not least, thank you to

my partner, Ashley Berninghaus, for being an inspiration, confidant, and adventure buddy.

CONTRIBUTION OF AUTHORS

Chapter 2: Emi Ampo and Dylan Nelson assisted with experiment execution. Drs. James Benson and Ali Eroglu assisted with manuscript review.

TABLE OF CONTENTS

TABLE OF CONTENTS (Continued)

Page

TABLE OF CONTENTS (Continued)

Page

TABLE OF CONTENTS (Continued)

Page

LIST OF FIGURES

LIST OF FIGURES (Continued)

LIST OF TABLES

LIST OF APPENDICES

1. GENERAL INTRODUCTION

1.1 Cryopreservation Background and Limitations

Cryopreservation stands at the forefront of the long-term storage of biological specimens. The ability to cryopreserve any specimen, from single cells to tissues to organs, would forever change the face of medicine and have far-reaching implications for many scientific fields. This is not the current situation, but many strides have been made in the research of each specimen regime. Single cell cryopreservation has been applied successfully for many different bacterial and mammalian cell types and has been instrumental in reproductive medicine in both animal breeding and assisting human reproduction [9,34,68,92,107,115]. At the tissue level, impacts can be again seen within the field of reproductive medicine with the successful cryopreservation of ovarian tissue [113,120]. Also, we can see the successful cryopreservation of articular cartilage, which has applications for tissue banking and subsequent transplantation [76]. Moving to the most complex specimen regime of organs, we can see the demonstrated feasibility of successfully cryopreserving a rabbit kidney from Fahy [49]. Despite these successes in the field, it is still an immense challenge to successfully cryopreserve complex three-dimensional tissues and organs; successful examples are few [47,48]. There is a gap in our knowledge when it comes to successfully cryopreserving complex specimens. Breakthroughs in complex specimen cryopreservation would have far-reaching implications for 1) transplantation medicine of donor and engineered specimens, and 2) banking specimens for numerous research endeavors [48,61,90].

The difficulties in preserving the most complex specimens stem from the biggest problem incurred during cryopreservation, which is ice formation [47,105]. There are two general methods to cryopreservation—slow cooling and vitrification—and they refer to if extracellular ice is formed, as excessive intracellular ice cannot be tolerated by any specimen. Slow cooling involves the formation of extracellular ice and is ubiquitous when discussing the cryopreservation of suspension-phase cells. However, vitrification eliminates ice formation in general by holding a specimen in the glassy state and is especially promising for specimens that are damaged by extracellular ice formation such as the complex specimens of adherent cells, tissues, and organs [49,76,94,121]. In order to overcome ice formation, a large concentration of foreign chemicals—designated as CPAs—need to be introduced to the specimen. As most complex specimens are heat transfer limited due to their large thermal mass when compared to suspension-phase cells (e.g. a 1 mL suspension of cells compared to an entire kidney), a higher CPA concentration is needed in order to increase the crystallization time and give the specimen a chance to reach its glass transition temperature. However, such a large concentration of CPAs introduces both mechanical (osmotic) damage and chemical (toxicity) damage. For osmotic damage, large osmotic gradients are induced due to the high concentration of CPAs, and the resulting fluxes of multiple species in the fluid phase can cause a cell or tissue space to shrink or swell beyond physiological limits [29,38,40,47,86]. Osmotic damage can be overcome, though, with a CPA addition and removal protocol that slowly manipulates the CPA concentration of the specimen in either a stepwise or continuous fashion. This prevents excessive volume excursions [29,38,59,86,98]. Toxicity is a more challenging problem and is considered the biggest hurdle to successful vitrification [5,46,47,75]. In the end, vitrification trades the ice formation problem for a toxicity problem.

The problem of toxicity is a challenging one as there are several variables of a CPA addition and removal protocol that can influence toxicity. CPA mixture type, CPA concentration, temperature, and exposure time can be varied across multiple steps. There are some general rules of thumb that can be applied in order to get an idea about the toxicity of a protocol. For example, toxicity tends to increase with increasing temperature as well as exposure time [29,36,46,85]. However, one can increase temperature in order to increase mass transfer rates which would result in a shorter exposure time required in order to meet a concentration of interest. Thus, it becomes difficult to develop an intuition about the toxicity of a protocol when multiple variables are changed. To overcome this, large data sets characterizing toxicity need to be collected in order to develop intuition about a specimen and make predictions.

Some studies in the field serve as good examples of obtaining large data sets that seek to characterize toxicity for a given specimen. One of the big challenges of obtaining a sound data set is to make sure that the toxicity results are not confounded by osmotic damage. As mentioned previously, osmotic damage can be overcome by slowly manipulating the CPA concentration a specimen is exposed to. However, some studies have not taken this approach and have exposed their specimens directly to peak CPA concentrations, making interpretation difficult [4,130]. Some of the largest data sets that seek to isolate toxicity and eliminate osmotic damage come from two groups, one researching chondrocytes [5,38,75] and the other researching rabbit kidneys [46]. Although both groups present some of the most comprehensive toxicity characterization attempts in the field, their data sets are still lacking. This lack stems from minimal dependency of the data set on exposure time and temperature. Their data sets have a large dependency on CPA mixture type and CPA concentration but at very few exposure times and temperatures. These data sets serve to move the understanding of toxicity forward but do lack the ability to provide a comprehensive understanding of toxicity kinetics, as they account for a narrow range of CPA mixture type, CPA concentration, exposure time, and temperature combinations.

Large data sets serve as a foundation to understand toxicity, and predictive capabilities can start to be developed from them. Going back to the large data set examples, the chondrocyte studies [5,38,75] leveraged regression models with interactions to predict toxicity as a function of CPA mixture type and concentration. Fahy and colleagues [46] looking at rabbit kidneys also proposed an empirically driven relationship where they predicted the toxicity of vitrification solutions based on simple concentration properties of the solution. These relationships highlight promising attempts at predicting the toxicity of vitrification solutions based on the composition of the solution. However, as discussed previously, these relationships are limited due to a lack of exposure time and temperature dependence. Also, these relationships can be classified as empirically-based approaches to toxicity reduction, and there is a good chance they will have limited value at some point outside of the direct data sets from which they were formed from. There will always be more CPA solution compositions or equilibration techniques to test in the laboratory in order to expand the applicability of empirical relationships. As such, empirically-based approaches can never exhaustively test all possible combinations of CPA mixture type, CPA concentration, exposure time, and temperature. Successes can be found with an empirical approach such as the work of Fahy and colleagues [49] who showed the feasibility of vitrifying a lone rabbit kidney, but the odds are stacked against such an approach in the face of so many variables to choose from. One must take a large data set and start to create a more comprehensive mathematical model rooted in physical phenomena that can make many predictions outside of the data set.

1.2 A Potential Solution Strategy

As has been stated, there are several potential avenues to address toxicity, from empirical to mathematical and the area in between the two. We have taken a mathematical optimization approach to toxicity minimization, and in previous works, we developed a toxicity cost function that we hope to expand [11,28,29]. This cost function approach takes a CPA addition and removal protocol as an input and outputs a toxicity cost. The inputs are number of protocol steps, as well as the duration, temperature, and CPA composition used for the steps—we account for all of the variables influencing toxicity kinetics. The toxicity cost output is a metric of the viable cells remaining. We implemented the toxicity cost function approach at the single cell level for bovine pulmonary artery endothelial cells (BPAEC) to begin with and were able to mathematically iterate through the protocol inputs in order to minimize the toxicity cost output. Starting at the single cell level allows us to develop the algorithm in the simplest specimen regime both physiologically and mathematically, while providing knowledge that can be applied to more complicated specimen regimes. Overall, we implemented an algorithm where we sought to minimize toxicity cost while operating under the constraints of introducing enough CPA for vitrification and staying within the physiological cell volume limits.

Our approach relies on mathematical modeling to generate the toxicity minimization algorithm, where we need to have a mass transport description of the system coupled to a damage description. We laid the mass transport groundwork in earlier work where we measured the permeability of BPAEC [56] within the two-parameter (2P) model formalism [79]. The 2P model provides cell volume predictions to keep a protocol within cell volume constraints. It also provides intracellular CPA concentration predictions if a toxicity description is to be dependent on the intracellular composition. Toxicity predictions are harder to make, however. Mechanisms of toxicity are research fields unto themselves and fully applying such knowledge for cryopreservation applications is challenging and inherently CPA dependent. For example, glycerol inhibits the glycerol phosphate cycle [70], and dimethyl sulfoxide interferes with ion channels [73] among other proposed mechanisms. For the toxicity cost function approach to be most effective, we need simple toxicity relationships for a wide variety of solutions—a systems biology perspective is required. A mechanistic/reductionist description of toxicity would increase the complexity of the models employed and would inevitably increase computational time for optimization. In a previous work [29], we described the simplest form of toxicity kinetics, where we assumed that BPAEC had a constant cell death (toxicity) rate. We modeled this toxicity rate as a function of CPA concentration and temperature for an exposure of the BPAEC to glycerol. In the end, we were able to predict a novel protocol for glycerol addition and removal that greatly improved cell yield above conventional protocols. Through this success, there are many avenues of research to expand upon within the toxicity cost function approach.

We could find the best cryopreservation protocol for BPAEC if the entire protocol input space was available for the algorithm. Of course, it is not, since we only have data for glycerol, and the biggest variable to explore for a protocol is that of the CPA mixture type. Outside of conventional CPAs, there are many potential candidates for CPAs that have not been historically treated as such, all with presumptive varying toxicities. Not only are there single compounds that could be potential CPAs and have lower toxicity, but there are combinations of compounds. Most vitrification protocols use multi-CPA cocktails in an attempt to mitigate toxicity [47,76]. The sheer number of experiments that must be conducted to characterize the toxicity of libraries of compounds is incredibly vast, though. For each CPA mixture type, CPA concentration, exposure time, and temperature need to be varied in an experiment, in conjunction with the multiple steps probably required to avoid osmotic damage. In order for the toxicity cost function approach to become more robust and move forward, the CPA mixture type input needs to be expanded.

CPA mixture type is the biggest variable to explore for BPAEC, but as has been mentioned, our goal is the cryopreservation of complex specimens. We believe that the toxicity cost function approach will eventually be able to describe and hopefully predict successful vitrification protocols for the most complex specimens of interest. That being said, we can have exhaustive predictive capabilities of any CPA mixture type for BPAEC, but we are still a long way from applying the toxicity cost function approach to an organ. As such, the specimen type is limited within the current toxicity cost function approach. Benson et al [13] described a way to calculate the toxicity cost within three-dimensional tissue structures, which would include organs, but to calculate the toxicity cost, we need a mass transfer model to predict the CPA distribution within the specimen as a function of time and space. The development of adequate mass transfer models in complex specimens is a very challenging problem. The complex geometry of a three-dimensional specimen is challenging in and of itself, but there are several physical phenomena that also need to be considered. Within a complex specimen, we need to consider mass transfer in the extracellular space which becomes very difficult with non-dilute vitrification solutions, the coupled effects of mass transfer in the extracellular space with mass transfer across the cell membrane (2P model for example), the mechanical properties of the specimen that can lead to volume changes due to mass transfer, and fixed electrical charges within the tissue that can impact mass transfer and volume changes.

The future of the toxicity cost function approach can be thought of as having two main research fronts. The first is expanding along the protocol complexity front, and we have discussed the need to be comprehensive within that front by including CPA mixture type, CPA concentration, exposure time, and temperature within a protocol. We have also discussed that CPA mixture type is the biggest variable to explore for a protocol and large data sets need to be obtained in order to characterize the toxicity of a large library of potential CPAs. By characterizing the toxicity and generating toxicity models for many CPAs, the toxicity cost function approach becomes more robust and we have a greater probability of finding the best CPA addition and removal protocol for a specimen. The second front is to consider more complex mass transfer models to adequately describe the flow of CPAs within three-dimensional specimens. These two research fronts expand upon the applicability of the toxicity cost function approach and have set the stage for my graduate research studies within cryopreservation.

1.3 Current Work and Organization

The research portion of this dissertation is broken up into three chapters that delve into extending the applicability of the toxicity cost function approach, and two of these chapters are motivated directly from the work of Davidson et al [29]—application of the toxicity cost function for BPAEC. The chapters will also be divided based on one of the two research fronts that expand upon the toxicity cost function approach, which have been mentioned previously.

1.3.1 Chapter 2

To start, Chapter 2 builds off of Davidson et al [29] and investigates the protocol complexity front, specifically CPA mixture type. The work presents an accepted manuscript that characterizes the toxicity of five of the most common CPAs as well as their binary and ternary mixtures for the model system of BPAEC. In doing so, we developed a methodology to measure toxicity using automated liquid handling on a Hamilton Microlab STARlet system. This methodology improved the accuracy of the data obtained and allowed for higher throughput than the manual methods of Davidson et al [29]. This work generated a large toxicity data set that serves as our first large data set acquisition, but we have developed methods using automated liquid handling to create a high-throughput CPA toxicity screening pipeline in the future. The current toxicity data set can also be used for future vitrification solution optimization and provides key learnings for how multiple CPAs within a solution impact toxicity. As a future work, we are investigating ways to predict the toxicity rates as a function of CPA mixture type, as our previous toxicity rate description from Davidson et al [29] only predicted toxicity rate as a function of glycerol concentration and exposure temperature. Our first toxicity data set was acquired at the room temperature isotherm and we focused on CPA mixture type as our biggest variable of interest, but in the future, we can also investigate many CPA mixture types as a function of temperature with our high-throughput methodology.

1.3.2 Chapter 3

In Chapter 3, we depart from the protocol complexity research front and the work of Davison et al [29]. Instead, we look at the mass transfer research front and more complicated specimens than single cells. Specifically, we seek to build off of the most comprehensive mass transfer model presented in the cryobiology literature. The work of Abazari et al [1] presents a model for the flow of CPA within articular cartilage and treats cartilage as a four-component system: water, CPA, salt, and solids. The continuum description of cartilage checks most of the boxes for the physical phenomena that could be important for CPA addition and removal protocol design: a non-dilute mass transfer description for the extracellular space, a mechanical representation of the tissue that allows for volume changes, and fixed electrical charges. However, the model does not account for the coupling between extracellular mass transfer and mass transfer across the cell membrane. This is an adequate assumption for the low cell density of cartilage but does not apply to tissues in general, specifically high cell density tissues. We hypothesize that such a continuum description of a tissue, though, can be applied to any tissue, not just cartilage. As such, the model proposed by Abazari et al [1] could be extended to a general tissue. To model a specific tissue, one would just have to change a few specific parameters for that given tissue. In order to move the model of Abazari et al [1] to the general case, we must first address the inherent coupling between extracellular mass transfer and mass transfer across the cell membrane. Chapter 3 presents a draft manuscript of the augmentation of the model of Abazari et al [1] and a first attempt at applying the general framework to a tissue outside of cartilage—pancreatic islets.

1.3.3 Chapter 4

In Chapter 4, we move back to the foundation of Davidson et al [29] but continue on the specimen complexity research front. In particular, we move to the most complex specimen regime of organs. As has been mentioned, we seek to be able to successfully vitrify the most complex specimens, and organs stand as the holy grail of the field. In this work, though, we do not investigate mass transfer modeling but investigate some experimental methods that can inform models in the future. To initially probe the organ regime, we completed some preliminary perfusion experiments using porcine kidneys where we manipulated the tonicity of the perfusate used. Manipulating tonicity was identified in Davidson et al [29] as a key variable when designing a less toxic protocol when compared to conventional methods. For example, it is conventional to load CPAs in isotonic buffer, but it was found in Davidson et al [29] that loading CPA in hypotonic buffer—leveraging cell swelling—led to a novel protocol that was less toxic. As such, the question becomes whether this technique can be applied to more complex specimens. We found similar qualitative trends between kidneys and single cells (BPAEC) when perfused with CPA in hypotonic buffer compared to CPA in isotonic buffer. From this, the questions of perfusion uniformity and osmotic damage also arose. To address these questions, we developed methods using CT to investigate the distribution of CPA within the kidney and we developed a LDH assay to assess osmotic damage of the hypotonic treatment.

RAPID QUANTIFICATION OF MULTI-CRYOPROTECTANT TOXICITY USING AN AUTOMATED LIQUID HANDLING METHOD

Ross M. Warner[a], Emi Ampo[a], Dylan Nelson[b], James D. Benson[c], Ali Eroglu[d], and Adam Z. Higgins[a]

[a]School of Chemical, Biological and Environmental Engineering, Oregon State University, Corvallis, Oregon, USA.

[b]College of Pharmacy, Oregon State University, Corvallis, Oregon, USA.

[c]Department of Biology, University of Saskatchewan, Saskatoon, SK, Canada.

[d]Department of Neuroscience and Regenerative Medicine, Medical College of Georgia - Augusta University, Augusta, Georgia, USA.

Cryobiology

C/O Paracorp
245 W Chase St
Baltimore, MD 21201
United States

Accepted

2. RAPID QUANTIFICATION OF MULTI-CRYOPROTECTANT TOXICITY USING AN AUTOMATED LIQUID HANDLING METHOD

2.1 Abstract

Cryopreservation in a vitrified state has vast potential for long-term storage of tissues and organs that may be damaged by ice formation. However, the toxicity imparted by the high concentration of cryoprotectants (CPAs) required to vitrify these specimens remains a hurdle. To address this challenge, we previously developed a mathematical approach to design less toxic CPA equilibration methods based on the minimization of a toxicity cost function. This approach was used to design improved methods for equilibration of bovine pulmonary artery endothelial cells (BPAEC) with glycerol. To fully capitalize on the toxicity cost function approach, it is critical to describe the toxicity kinetics of additional CPAs, including multi-CPA mixtures that are commonly used for vitrification. In this work, we used automated liquid handling to characterize the toxicity kinetics of five of the most common CPAs (glycerol, dimethyl sulfoxide (DMSO), propylene glycol, ethylene glycol, and formamide), along with their binary and ternary mixtures for BPAEC. In doing so, we developed experimental methods that can be used to determine toxicity kinetics more quickly and accurately. Our results highlight some common CPA toxicity trends, including the relatively low toxicity of ethylene glycol and a general increase in toxicity as the CPA concentration increases. Our results also suggest potential new approaches to reduce toxicity, including a surprising toxicity neutralization effect of glycerol on formamide. In the future, this dataset will serve as the basis to expand our CPA toxicity model, enabling application of the toxicity cost function approach to vitrification solutions containing multiple CPAs.

2.2 Introduction

The ability to cryopreserve living biological samples has had far-reaching implications in many fields. For example, cryopreservation is routinely used to store bacterial and mammalian cells, making thousands of cell types available to the research community [9,34,92]. In addition, cryopreservation of gametes and embryos has dramatically improved animal breeding, and expanded options and improved outcomes for human assisted reproduction as well [68,107,115]. However, not all biological samples can be successfully cryopreserved. In particular, it remains a challenge to cryopreserve complex three-dimensional samples such as tissues and organs [47,48]. Breakthroughs in complex specimen cryopreservation would have far-reaching implications for medicine and public health including organ transplantation, banking tissues for research including drug discovery, and banking skin, blood vessels, and bone marrow for emergency preparedness [48,61,90].

Cryopreservation methods can be divided into two main categories: slow cooling and vitrification. Slow cooling involves formation of extracellular ice and is often successful for cryopreservation of suspension-phase cells. Vitrification is particularly promising for preserving specimens that are damaged by extracellular ice formation, such as adherent cells, tissues, and organs [49,76,94,121]. The main challenge with vitrification methods is that a high concentration of CPA(s) must be added to prevent ice formation. Exposure to high CPA concentrations can cause damage by two mechanisms: 1) mechanical (osmotic) damage from specimen volume excursions, and 2) chemical (toxicity) damage from unfavorable CPA interactions with the specimen [29,38,40,47,86]. Osmotic damage can be overcome by slowly adding and removing CPA to prevent excessive volume excursions [29,38,59,86,98]. However, toxicity is more challenging and is considered the single biggest hurdle to vitrification [5,46,47,75].

Before toxicity can be reduced, it first needs to be characterized. One of the biggest challenges with measuring toxicity is decoupling it from osmotic damage. Several previous studies involve direct exposure to high CPA concentrations [4,130]. This can cause osmotic damage, making it impossible to distinguish whether a corresponding loss of viability is due to toxicity or osmotic damage. Studies that have attempted to decouple toxicity from osmotic damage include the chondrocyte studies of Jomha et al [75], Almansoori et al [5], and Fahmy et al [38]. These studies provide an in-depth analysis of the toxicity of CPAs to chondrocytes, including development of a mathematical model that enables prediction of toxicity as a function of CPA mixture composition. However, the model does not allow prediction of CPA toxicity as a function of exposure time or temperature. The work of Fahy and colleagues [46] serves as another example of a large data repository that decouples osmotic damage from toxicity but for rabbit kidneys. They propose an interesting empirical relationship linking the toxicity of a vitrification solution to its composition, which may facilitate selection of less toxic compositions for vitrification, but again, the relationship lacks a time and temperature dependency. Overall, current data sets are lacking, and there is a need for a more comprehensive understanding of toxicity kinetics for design of CPA equilibration methods in which exposure time and temperature are varied.

The vast majority of previous efforts to reduce CPA toxicity have used an empirical approach. For example, Fahy and colleagues chose to iteratively exploit CPA solution compositions and the corresponding perfusion pressure, temperature, and duration as a way to overcome CPA toxicity, and thus to vitrify rabbit kidneys [39-44,47-52]. Others have explored the use of additives in an attempt to reduce CPA toxicity [106,134,135]. While these empirical approaches have led to some promising results, including the long-term survival of a lone rabbit kidney after vitrification [49], there are too many potential solution compositions and/or equilibration methods to exhaustively test experimentally.

Mathematical modeling can potentially address this limitation by exploring the range of possible CPA equilibration methods in silico and identifying promising approaches toward reducing CPA toxicity. A recent example is the use of diffusion predictions to design methods for equilibration of articular cartilage with CPAs [74,76,119]. The predictions were used to design a multistep vitrification protocol with the goal of reaching a desired minimum CPA concentration in the shortest amount of time [119]. Karlsson and colleagues also used mathematical modeling to minimize the duration of CPA equilibration in an attempt to reduce CPA toxicity [77]. However, minimizing CPA equilibration time does not necessarily correspond to minimizing toxicity [13]. Another example comes from Lawson et al [86] where heat and mass transfer were modeled as well as CPA toxicity. Lawson et al [86] used their model to predict cell viability for several protocols of interest, but they stopped short of using their model for optimization of CPA equilibration methods to minimize toxicity.

In previous studies, we sought to minimize toxicity through the development of a toxicity cost function [11,28,29]. This cost function approach enables the estimation of toxicity during CPA equilibration, making it possible to mathematically optimize methods that minimize toxicity. We implemented the toxicity cost function approach for adherent BPAEC and were able to predict a novel protocol for glycerol addition and removal that greatly improved cell viability compared to conventional equilibration protocols [29]. To date, the toxicity cost function approach has only been used to design methods involving a single CPA. However, many vitrification protocols use multi-CPA mixtures in an attempt to mitigate toxicity [47,76], highlighting the need for development of a toxicity model that can account for multiple CPAs. Without new experimental methods that ease the workload burden over previous manual methods [29], the task of conducting the large set of experiments needed to assess multi-CPA toxicity would be cumbersome and difficult.

In this work, we quantified the toxicity of five of the most common CPAs (glycerol, DMSO, propylene glycol, ethylene glycol, and formamide), as well as their binary and ternary mixtures, using BPAEC as a model system. For these CPA mixture types, we varied CPA concentration and exposure time at room temperature. In order to carry out these experiments, we developed methods leveraging automated liquid handling using a Hamilton Microlab STARlet system. The Hamilton system features a 96-channel head that can manipulate fluid in every well of a 96-well plate at the same time, and it has 8 independently moving channels that we used to prepare CPA solution reservoirs. As a result, automated liquid handling allowed us to randomize CPA treatment locations in the 96-well plate format, as well as improve the accuracy of our experiments and increase throughput when compared to our previous manual methods [29]. The resulting comprehensive toxicity data set provides a foundation for future expansion of the toxicity cost function approach to vitrification using CPA mixtures.

2.3 Methods and Materials

2.3.1 Experimental Overview

This work is a direct extension of our previous work [29] where we measured the viability of an adherent monolayer of BPAEC after exposure to glycerol while varying exposure time, temperature, and glycerol concentration. By varying these experimental conditions, we were able to characterize the toxicity rate of glycerol as a function of concentration and temperature. In this work, we again seek to characterize CPA toxicity but for more CPA types and for mixtures containing multiple CPAs. Table 2.1 details the experimental conditions tested.

Table 2.1. CPA exposure conditions tested.

CPA Mixture Type	**Single CPA**	**Binary Mixture**	**Ternary Mixture**
CPAs	Glycerol, DMSO, propylene glycol, ethylene glycol, formamide	10 binary combinations of the 5 CPAs	10 ternary combinations of the 5 CPAs
Total CPA Concentrations (molal)	1, 3, 5, 7, 10	1, 3, 5, 7, 10 (equi-molal split between CPAs)	7 (equi-molal split between CPAs)
Times (min)	5, 10, 30, 60		
Temperature (ºC)	Room temperature (25 ± 2.1)		

Table 2.1 highlights that we tested a total of 340 experimental conditions. For each condition, multiple solution exchange steps are required, including washing the cells at the beginning and end of the protocol, as well as multi-step addition and removal of CPA to avoid osmotic damage. This results in thousands of pipetting operations, many of which need to be timed precisely. To facilitate these pipetting operations, we utilized an automated liquid handling instrument at the Oregon State University High Throughput Screening Services Laboratory. In our previous work, we conducted CPA exposure experiments manually, and we will discuss later on the benefits of moving to an automated liquid handling methodology.

Although we changed our liquid handling methodology, the core principles of the experiment remained the same. Namely, we cultured the BPAEC in 96-well plates, exposed the BPAEC to various solutions through repeated aspirate/dispense operations, and measured viability before and after CPA exposure using the PrestoBlue assay.

2.3.2 Cell Culture

BPAEC were purchased from Cell Applications, Inc. (San Diego, CA). The cells were received at passage 2 and subsequently expanded to passage 5 using culture methods described previously [29,56], at which point they were cryopreserved in 90% culture medium (Dulbecco's Modified Eagle Medium augmented with 5% fetal bovine serum, 100 U/mL penicillin, and 100 µg/mL streptomycin [29,56]) and 10% DMSO (Corning Inc., Corning, NY). These cryopreserved cells were used for all experiments. For each experiment, a vial of cells was thawed (~10^6 cells/vial), seeded into a T-75 flask containing 15 mL of culture medium, and cultured for 24-30 h, at which point the cells had reached about 80% confluency. At that time, the cells were harvested and seeded into black clear bottom 96-well plates (Greiner Bio-One, Monroe, NC) at a density of 1500 cells/well. The cells were cultured in the well plates for two days, at which point an initial PrestoBlue assay was performed. The cells were then treated with CPA solutions and cultured for an additional 20-24 h before performing the final PrestoBlue assay. This approach allowed us to maximize confluency to increase the signal in the PrestoBlue assay, while making sure that confluency did not reach 100% at the end of the experiment on the third day.

2.3.3 Experimental Solutions for CPA Addition and Removal

We employed multi-step CPA addition and removal to mitigate osmotic damage, as described in our previous study [29]. Table 2.2 shows the necessary steps for maximum CPA concentrations ranging between 1 and 10 molal, including the time the cells were exposed to each solution (see Appendix A for how CPA addition and removal steps were designed). Solutions were prepared in a similar fashion to our previous work [29]. The following chemicals were used to prepare the buffer solutions: $MgCl_2 \cdot 6H_2O$ (VWR Chemicals BDH, Radnor, PA), $CaCl_2 \cdot 2H_2O$ (Fisher Chemical, Waltham, MA), NaCl (VWR Chemicals BDH, Radnor, PA), KCl (EMD Millipore, Burlington, MA), and HEPES (VWR Chemicals BDH, Radnor, PA). The following CPAs were used: glycerol (Macron Fine Chemicals, Radnor, PA), DMSO (Fisher Chemical, Waltham, MA), propylene glycol (VWR Chemicals BDH, Radnor, PA), ethylene glycol (Macron Fine Chemicals, Radnor, PA), and formamide (Sigma-Aldrich, St. Louis, MO).

Table 2.2. Multi-step methods for CPA exposure. For each step, the solution composition is listed first followed by the exposure time in parentheses.

Max CPA Conc.	**Step 1**	**Step 2**	**Step 3**	**Step 4**	**Step 5**	**Step 6**	**Step 7**	**Step 8**	**Step 9**
1 molal	Isotonic Buffer (2.5 min)	**1 molal CPA in Isotonic Buffer (Variable)**	Hypertonic Buffer (3 min)	Isotonic Buffer (5 min)	Media (20-24 h)				
3 molal	Isotonic Buffer (2.5 min)	1 molal CPA in Isotonic Buffer (4 min)	**3 molal CPA in Isotonic Buffer (Variable)**	1 molal CPA in Hypertonic Buffer (4.5 min)	Hypertonic Buffer (4.5 min)	Isotonic Buffer (5 min)	Media (20-24 h)		
5 molal	Isotonic Buffer (2.5 min)	1 molal CPA in Isotonic Buffer (4 min)	3 molal CPA in Isotonic Buffer (2 min)	**5 molal CPA in Isotonic Buffer (Variable)**	3 molal CPA in Hypertonic Buffer (6.5 min)	1 molal CPA in Hypertonic Buffer (4.5 min)	Hypertonic Buffer (4.5 min)	Isotonic Buffer (5 min)	Media (20-24 h)
7 molal	Isotonic Buffer (2.5 min)	1 molal CPA in Isotonic Buffer (4.5 min)	3 molal CPA in Isotonic Buffer (4.5 min)	**7 molal CPA in Isotonic Buffer (Variable)**	3 molal CPA in Hypertonic Buffer (7 min)	1 molal CPA in Hypertonic Buffer (7 min)	Hypertonic Buffer (5 min)	Isotonic Buffer (5 min)	Media (20-24 h)
10 molal	Isotonic Buffer (2.5 min)	1 molal CPA in Isotonic Buffer (4.5 min)	3 molal CPA in Isotonic Buffer (10.5 min)	**10 molal CPA in Isotonic Buffer (Variable)**	3 molal CPA in Hypertonic Buffer (12.5 min)	1 molal CPA in Hypertonic Buffer (7 min)	Hypertonic Buffer (5 min)	Isotonic Buffer (5 min)	Media (20-24 h)

As shown in Table 2.2, CPA solutions were prepared in either isotonic or hypertonic buffer, at CPA concentrations ranging from 1 molal to 10 molal. This results in a total of 155 distinct CPA solutions. Rather than make 155 solutions from scratch, we prepared the solutions by diluting stock solutions as described in our previous work [29]. To make all of the 155 unique solutions, we only had to make 7 different stocks: isotonic HEPES buffered saline, hypertonic HEPES buffered saline, and 10 molal isotonic stocks of each of the 5 CPAs. All stock solutions were pH-adjusted to 7.3 ± 0.1 and sterile filtered.

Isotonic HEPES buffered saline was made as in our previous work [29]. The osmolality was measured to be within 2% of 300 mOsm on an Advanced Micro Osmometer Model 3300 (Advanced Instruments, Norwood, MA). The water mass concentration was determined by measuring the density of the solution and multiplying by the known water mass fraction, resulting in a value of 1 kg/L. The hypertonic HEPES buffered saline was made in the same way as its isotonic counterpart, but extra NaCl was added to bring the osmolality to 1200 mOsm, assuming a dissociation factor of 1.68 [29]. The measured osmolality was within 5% of 1200 mOsm. The water mass concentration of the hypertonic HEPES buffered saline was 0.97 kg/L.

For the CPA solutions in isotonic buffer, the concentration of nonpermeating solute was adjusted to ensure that the equilibrium cell volume was equal to the normal physiological volume. This nonpermeating solute concentration was calculated as before [29], and the 10 molal stocks were made by adding pure CPA to isotonic HEPES buffered saline with an additional amount of NaCl to reach the desired nonpermeating solute concentration. The necessary calculations for dilution of the stock solutions were made using their water mass concentrations, as described in our previous study [29]. The water mass concentrations of the 10 molal CPA stock solutions were measured to be 0.59 kg/L for glycerol, 0.60 kg/L for DMSO, 0.58 kg/L for propylene glycol, 0.66 kg/L for ethylene glycol, and 0.72 kg/L for formamide.

To make a CPA solution in isotonic buffer, 10 molal CPA stock solutions were diluted with isotonic HEPES buffered saline. The resulting CPA solution has a nonpermeating solute concentration that allows the cells to equilibrate at the normal physiological volume. For the CPA solutions in hypertonic buffer, the same dilution strategy was used but with hypertonic HEPES buffered saline. The hypertonic nature of the solution is not intended to allow the cell to equilibrate at its physiological volume but to counteract cell swelling during CPA removal.

2.3.4 Automated Liquid Handling

2.3.4.1 Overview

For the CPA exposure experiments, a Hamilton Microlab STARlet liquid handler (Hamilton Company, Reno, NV) was employed. The Hamilton system has both a 96-channel head and 8 independently moving channels that were used to conduct experiments. To carry out the experimental steps shown in Table 2.2, fluid was transferred from a source plate to the cell-seeded assay plate using the 96-channel head. Multiple source plates were needed that contained the necessary solutions for each step of the CPA addition and removal process. These source plates were prepared using the 8 independently moving channels. Figure 2.1 shows a picture of the Hamilton system and highlights its key features, along with demonstrating the fluid transfer scheme.

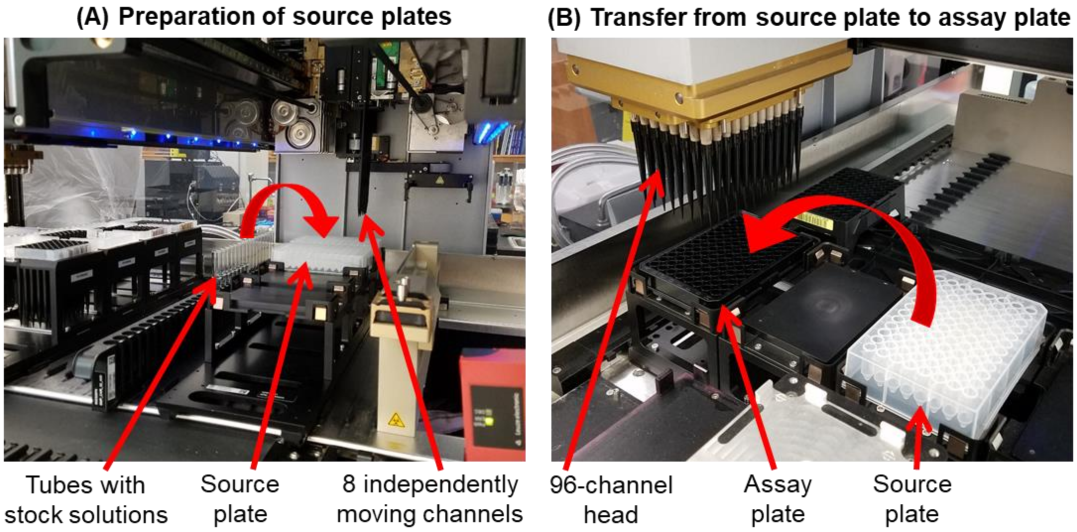

Figure 2.1. Pictures showing the key features of the Hamilton Microlab STARlet liquid handler. The 8 independently moving channels were used to fill source plates (A), and the 96-channel head was used to transfer fluid from a source plate to an assay plate (B).

2.3.4.2 Treatment Layouts on a 96-Well Assay Plate

With the capabilities of the Hamilton system, we were able to randomize the experimental conditions on a well-by-well basis on the assay plate. Plate layout maps were generated with a custom MATLAB script. We included 5 replicates per experimental condition, allowing us to have a total of 19 experimental conditions on a plate. Fifteen experimental conditions were dedicated to different CPA treatments, with one treatment having a randomly assigned 6th replicate. The remaining four experimental conditions were used for a positive control, negative control, and two different background media controls (see Fig. 2.3 in Results and Discussion for a plate layout example).

The positive control was subjected to the same liquid handling as a CPA treatment, but the fluid used at every step was isotonic buffer, with the exception of the media wash in the final step. The negative control was washed with isotonic buffer during the first step and then had no liquid handling until the penultimate step, at which point 70% ethanol in water was introduced. The media control wells were not seeded with cells and were kept in the same position on every plate to streamline the seeding process. One media control was subjected to the same liquid handling as the positive control. The other media control was only subjected to a water wash, and fresh culture medium was only added right before the PrestoBlue assay was conducted. The first media control served as the background fluorescence to subtract off for the assay, and the second media control serves as a check for contamination. The Hamilton system is open to the atmosphere, and the experiment takes place in semi-sterile conditions. If contamination were an issue and a resazurin reducing contaminant was present, we would expect a difference in the fluorescence signal to be seen between the two media controls. In our experiments, we did not see any spikes in the fluorescence signal of the second media control when compared to the first, nor did we see any evidence of contamination from random well checks under the microscope.

2.3.4.3 Preparation of 96-Well Source Plates

To enable the appropriate solution to be dispensed into each well at each step of the CPA addition and removal process, deep well plates were prepared containing solutions that mapped to the randomized treatment conditions of the assay plate. We refer to these deep well plates as source plates. A separate source plate was needed for each step in the CPA addition and removal process. The wash steps that do not include a CPA have a simple enough layout to fill source plates by manual pipetting, which was done under sterile conditions. However, source plates that require a CPA solution are nearly impossible to fill by hand because 16 different solutions with 5-6 replicates each must be dispensed into a randomized well. To overcome this challenge, we used the Hamilton system to fill the source plates that contained CPA solutions. The Hamilton system has 8 channels that can move individually, allowing automated control of well-by-well filling, and the 8 channels provide the means to successfully execute an experiment with randomized treatment locations. A custom MATLAB script was written that takes a plate map and generates the necessary commands for the Hamilton to fill a randomized source plate.

2.3.4.4 Automated Addition and Removal of CPA

After the initial PrestoBlue assay, the assay plate was immediately moved to the Hamilton system to carry out the subsequent liquid handling steps. For every experimental step, the following core operations were performed for every well: 1) aspirate, 2) dispense 250 µL, 3) aspirate, and 4) dispense 250 µL. We optimized the settings on the Hamilton system to minimize the amount of dead volume after aspiration while not disturbing the cell monolayer, which resulted in using an aspirate and dispense flowrate of 20 µL/s and a tip height offset from the bottom of the well of 500 µm.

Due to the nature of automated liquid handling, the pipette tip has to approach normal to the bottom of the well, resulting in a larger dead volume when compared to manual pipetting where the user can tilt the plate and slide the pipette tip down the side of the well. We measured a high-end well dead volume of 40 µL after aspiration, with the majority of dead volumes falling in the range of 20-40 µL. Using the high-end dead volume, the cells are exposed to approximately 86% of the intended change in fluid composition (by volume) after the first dispense and approximately 98% after the second dispense. We recorded the time the cells were exposed to a given fluid as the time between the first dispense from one source plate to the first dispense from the subsequent source plate. In the final dispense step on the Hamilton system, we transferred 180 µL of media (rather than 250 µL). This was done to achieve a total media volume of about 200 µL, the desired volume for the PrestoBlue assay.

2.3.5 Cell Viability Assay

Cell viability was assessed using PrestoBlue (Invitrogen, Waltham, MA) right before CPA exposure and then 20-24 h after CPA exposure. The 20-24 h recovery period in culture before the second PrestoBlue assay was included to allow time for apoptosis induced by CPA exposure to occur [8,26]. The assay was conducted in 200 μL of culture medium and 20 μL of PrestoBlue reagent. We measured fluorescence on a Synergy 4 plate reader (BioTek, Winooski, VT) using excitation and emission filters of 528 nm and 600 nm, respectively. The plate reader was pre-heated to 37 °C and held at this temperature throughout the assay. PrestoBlue was first added to the assay plate at room temperature, and then the plate was transferred to the plate reader and given 5 min to reach 37 °C, at which point the fluorescence was measured. After an additional 20 min the fluorescence was measured again, giving a 20 min development time. As in our previous study [29], we defined the cell viability as the final fluorescence after CPA exposure divided by the initial fluorescence before CPA exposure, normalized to the average fluorescence ratio for the positive control:

$$\text{viability} = \frac{F_\mathrm{f} F_\mathrm{i}^\mathrm{P}}{F_\mathrm{i} F_\mathrm{f}^\mathrm{P}} \qquad 2.1$$

where F is the background-corrected fluorescence signal from the plate reader, the subscripts i and f denote the initial and final PrestoBlue assays, and superscript P denotes the positive control.

2.3.6 Cell Viability Data Analysis

2.3.6.1 Determination of Toxicity Rates

As in our previous work [29], we used a first-order kinetic model for analysis of our viability data to determine the toxicity rate. In particular, we modeled the change in the number of viable cells N as follows:

$$\frac{dN}{dt} = \lambda N \qquad 2.2$$

where λ is the sum of growth and toxicity rates. From the initial time t_i to the final time t_f, we assumed a constant cell growth rate. The toxicity rate was assumed to vary depending on the CPA type and concentration. As an example of our data analysis method, consider an experiment with a maximum CPA concentration of 3 molal (see Fig. 2.2). This experiment involves exposure to a 1 molal CPA concentration during CPA addition and removal. Our data analysis method accounts for the different toxicity rates during exposure to each of these CPA concentrations.

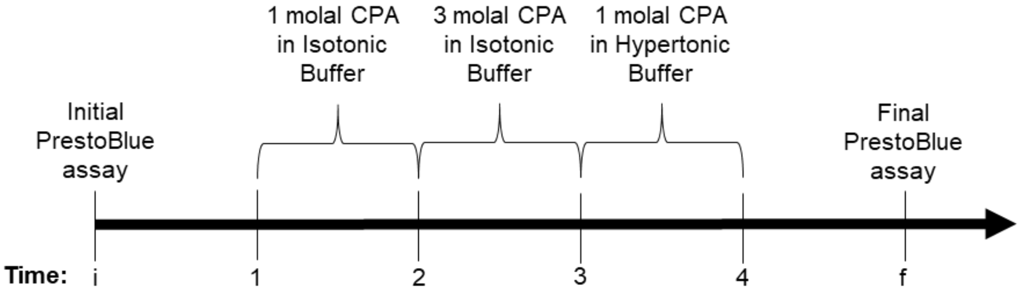

Figure 2.2. Timeline for an experiment with a maximum CPA concentration of 3 molal, showing the CPA addition and removal steps in relation to the PrestoBlue assays.

Figure 2.2 details that we have five distinct time periods, three of which are CPA exposure time periods. If we integrate Equation 2.2 for the five time periods with the convention $t_\mathrm{i} = 0$, we produce the following equations:

$$\frac{N_1}{N_\mathrm{i}} = \exp(\alpha t_1), \tag{2.3a}$$

$$\frac{N_2}{N_1} = \exp\big((\alpha - k_1)(t_2 - t_1)\big), \tag{2.3b}$$

$$\frac{N_3}{N_2} = \exp\big((\alpha - k_3)(t_3 - t_2)\big), \tag{2.3c}$$

$$\frac{N_4}{N_3} = \exp\big((\alpha - k_1)(t_4 - t_3)\big), \tag{2.3d}$$

$$\frac{N_{\mathrm{f}}}{N_4} = \exp\big(\alpha(t_{\mathrm{f}} - t_4)\big), \qquad 2.3e$$

where α is the growth rate, k_1 is the toxicity rate for 1 molal CPA exposure, and k_3 is the toxicity rate for 3 molal CPA exposure. To isolate k_3, we must first eliminate the growth rate. To do this, we can use the positive control, which is not exposed to CPA and hence does not exhibit CPA toxicity. For the positive control, we have from t_{i} to t_{f}:

$$\frac{N_{\mathrm{f}}^{\mathrm{P}}}{N_{\mathrm{i}}^{\mathrm{P}}} = \exp(\alpha t_{\mathrm{f}}). \qquad 2.4$$

If we multiply Equations 2.3a-2.3e and divide by Equation 2.4, we arrive at

$$\frac{N_{\mathrm{f}} N_{\mathrm{i}}^{\mathrm{P}}}{N_{\mathrm{i}} N_{\mathrm{f}}^{\mathrm{P}}} = \exp\big(-k_1(t_4 - t_3 + t_2 - t_1) - k_3(t_3 - t_2)\big). \qquad 2.5$$

The left-hand side of Equation 2.5 is equivalent to the cell viability as defined in Equation 2.1, since the fluorescence signal F is expected to be proportional to the number of viable cells N. The above equation includes two toxicity rates: k_1 and k_3. The value of k_1 was first determined from experiments with a maximum CPA concentration of 1 molal (see Table 2.2), leaving k_3 as the only unknown toxicity rate.

To find the toxicity rate k_3, we performed non-linear regression in MATLAB utilizing a least squares approach. Specifically, Equation 2.6 was used for the regression, which is a rearrangement of Equation 2.5:

$$\frac{N_{\mathrm{f}} N_{\mathrm{i}}^{\mathrm{P}}}{N_{\mathrm{i}} N_{\mathrm{f}}^{\mathrm{P}}} \exp\big(k_1(t_4 - t_3 + t_2 - t_1)\big) = \exp\big(-k_3(t_3 - t_2)\big). \qquad 2.6$$

We refer to the quantity on the left-hand side of Equation 2.6 as the adjusted cell viability. The adjusted viability was plotted versus the duration of exposure to 3 molal CPA (i.e., $t_3 - t_2$), which we varied according to the exposure times of Table 2.2 (5, 10, 30, and 60 min). The adjusted cell viability is a convenient quantity for examining toxicity during exposure to the maximum CPA concentration, as its value always starts at 1.

For higher CPA concentration exposures (5, 7, and 10 molal), the same approach was used but the value of k_3 in conjunction with k_1 is needed to find the corresponding toxicity rate. For the most toxic CPA treatments, where cell viability was less than 1% for even the 5 min CPA exposure, the toxicity rate could not be accurately determined.

In many cases, exposure to 1 molal or 3 molal CPA did not appreciably decrease cell viability, resulting in a best-fit toxicity rate that was not statistically different from zero. In these cases, we set the toxicity rate to zero for subsequent analysis. To assess this, we performed an F-test to estimate the p-value for the null hypothesis that the toxicity rate was equal to zero. Toxicity rates were only assumed significant for $p \leq 0.05$.

2.3.6.2 Outlier Analysis

For outlier analysis, we employed Tukey's (boxplot) method [125]. Outliers are identified if they are outside of the following range:

$$Q_1 - (k * IQR) \leq x \leq Q_3 + (k * IQR) \qquad 2.7$$

where Q_1 is the first quartile, Q_3 is the third quartile, IQR is the inter-quartile range which is the difference between the third and first quartiles, k is a constant, and x represents a specific sample value. Quartiles are found through the standard fourths method presented by Tukey. The value of k has been historically presented as 1.5 as a general rule of thumb. We opted to use of value of 2.5, which is more conservative and identifies less data points as outliers [20,55,71,125].

There are several samples in our data set that show ~0% average viability (e.g., exposure to 10 molal formamide). These samples are prone to erroneous identification of outliers. As such, we implemented outlier analysis only for samples that showed at least 1% average viability. If an outlier was identified in a positive control, the CPA treatments were normalized against the positive control sample excluding the outlier. Overall, 3.9% of the entire data set was labeled as outliers. This is comparable to the work of Hoaglin et al [71], which found approximately 8.6% of data to be labeled as outliers for $k = 1.5$ and 3.3% of data to be labeled as outliers for $k = 3$.

2.4 Results and Discussion

2.4.1 Benefits of Automated Liquid Handling

The use of automated liquid handling afforded us several benefits over our past work [29] that utilized manual pipetting. These benefits can be broken down into three main categories: 1) consistency of pipetting, 2) increased throughput for faster data generation, and 3) the ability to increase the complexity of the experimental workflow, including randomization of the experimental groups within the well plate.

One of the biggest changes we made to our experimental setup was randomizing the locations of experimental conditions on a 96-well assay plate. This required preparation of multiple source plates containing appropriate wash solutions in randomized locations, a task that would have been very challenging to accomplish manually. Figure 2.3 (top left panel) shows a schematic of a representative 96-well plate where we tested 15 different CPA treatments. By randomizing locations on the well plate, we can distribute any systematic bias associated with location between treatments. Systematic bias has been reported due to higher rates of evaporation near the edges of the well-plate [91,131], and can also occur due to pipetting inconsistencies when using a multi-channel pipette. Overall, randomization of treatments within a well plate helps to improve results by mitigating location bias [83,84,96,117].

The automated liquid handling system also enables improved consistency compared to manual pipetting. Pipetting operations can yield erroneous results through accidental mechanical damage to cultured cells and/or imprecise aspirate/dispense volumes [65,87]. In some cases, there can even be doubt if the pipetting operation was carried out [93]. With the automated liquid handling system, we know the exact location of the pipette tip in relation to the cell monolayer, and the aspirate/dispense flowrate is precisely controlled. This enabled us to optimize settings to ensure that cells were not sheared from the surface during pipetting, as illustrated in Figure 2.3 (top right panel). In addition, there is a digital record that the pipetting operation was carried out, and the timing of each pipetting operation is controlled.

Taken together, plate randomization and improved pipetting consistency are expected to reduce variability and lead to more accurate results. These improvements are illustrated in the bottom panels of Figure 2.3, which compare viability data we obtained in the current work to the corresponding results from our previous work [29]. A noticeable difference can be seen in the error bars: the average standard deviation in our previous work was 12.9% [29], compared to 6.0% for our current work. In addition, we observed a more substantial decrease in viability after exposure to high glycerol concentrations in our previous work, especially at early time points [29]. One explanation for this difference is the removal of viable cells through manual pipetting, either due to accidental contact between the pipette tip and the culture surface or excessive aspirate/dispense rates. As a result, in our current work, we have measured toxicity rates for glycerol to be about one-half of those in our previous work [29]. Overall, increased pipetting consistency and the ability to randomize the location of treatments has allowed us to develop a more accurate methodology for measuring CPA toxicity.

As a final benefit of automated liquid handling over manual liquid handling, we not only can conduct more complicated experiments with higher precision, but we can conduct them more quickly resulting in higher throughput. As a simple comparison between the two liquid handling approaches, we can compare the number of pipetting operations between a manual 12-channel pipette and the 96-channel head of the Hamilton system. With the 96-channel head, we can perform about ~8x as many pipetting operations in the same amount of time as a 12-channel pipette, which by itself, would be expected to increase throughput ~8x. However, with manual pipetting, the user also has to manipulate the assay plate and source plates, perform multiple tip changes during a step, and manually keep track of pipetting operations and their timing—all of which takes more time than automated liquid handling. Over the course of an experimental day, we also have to consider an increase in user fatigue from having to carry out so many manual operations, which could further slow the process towards the latter part of a workday. In the end, automated liquid handling provides a platform to conduct CPA exposure experiments in a faster, more precise, and more robust manner when compared to manual pipetting.

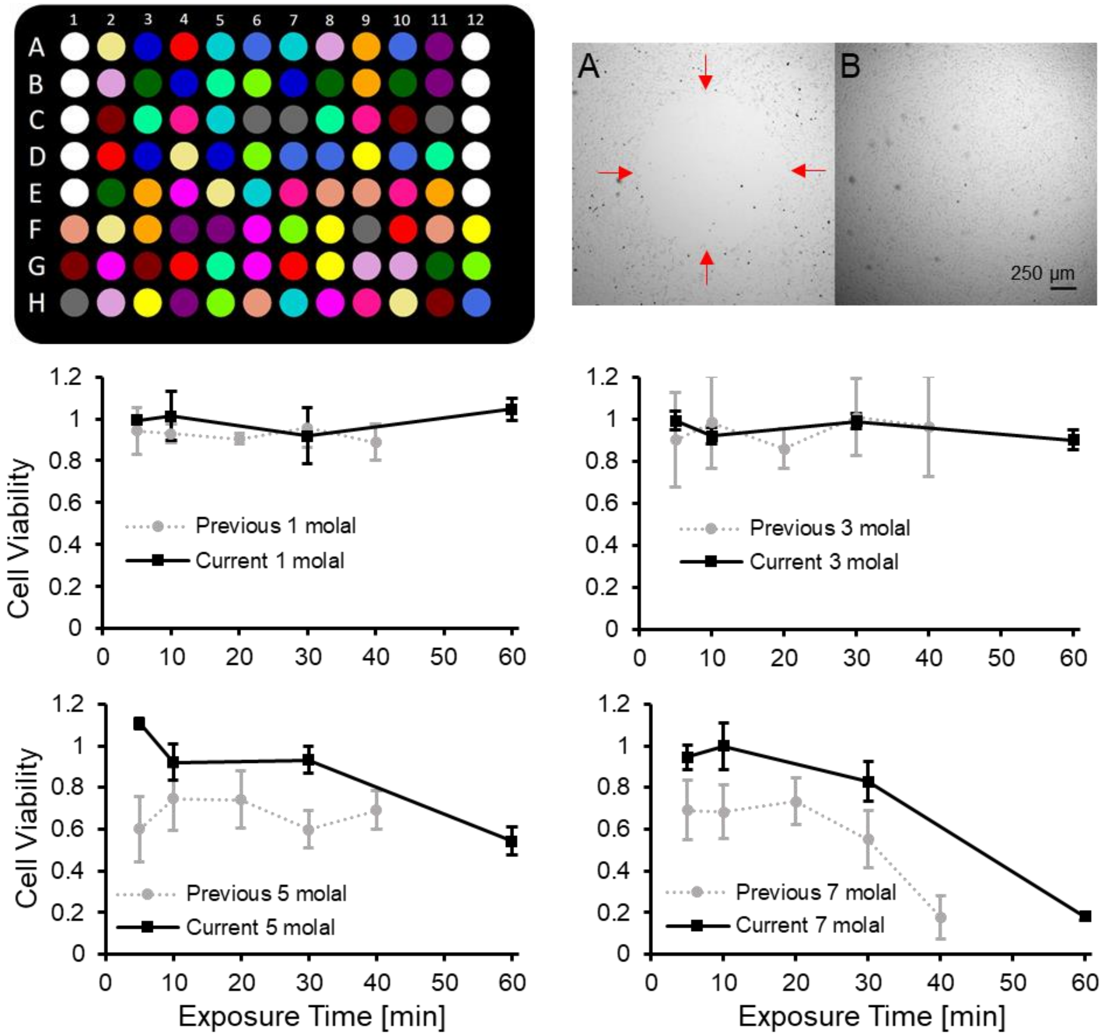

Figure 2.3. Automated liquid handling reduces experimental variability and enables high-throughput measurement of CPA toxicity. Top left panel: schematic of a randomized 96-well plate map. The cell-free media controls (white wells) are in A1-E1 and A12-E12. The remaining wells are seeded with cells and treatments are

randomly distributed throughout the rest of the plate. These include the positive controls (dark green), negative controls (red), and CPA treatments (15 unique colors). Top right panel: side by side comparison of a cell monolayer before (A) and after (B) optimizing the pipetting settings. There is a distinct hole in the monolayer in the before image with red arrows indicating the boundary. The images were taken under different lighting conditions and have been contrast enhanced. Bottom panels: comparison of the cell viability data between our previous [29] and current work for exposure to 1, 3, 5, and 7 molal glycerol. Error bars represent the standard deviation. We subjected our previous data set to the outlier analysis described in the methods section of the current study.

2.4.2 Cell Viability Decreases after Exposure to CPA

The goal of this study was to quantify the toxicity of five of the most common CPAs: glycerol, DMSO, ethylene glycol, propylene glycol, and formamide. The bottom panels of Figure 2.3 show representative cell viability data after exposure to glycerol. Cell viability decreased as the glycerol concentration increased and as exposure time increased. Similar trends were observed for the other CPAs. While this loss of cell viability is consistent with CPA toxicity, there are other potential explanations, including cell detachment from the culture surface and osmotic damage.

2.4.3 Are Cell Losses Caused by Cell Detachment?

Although we have confirmed that negligible cell detachment from the culture surface occurs in the positive control wells, it is possible that exposure to CPA weakens cell adhesion leading to loss of viable cells into the wash solution during liquid handling. To test this, we collected the cells in the solution phase in each of the CPA removal steps after exposure to 7 molal CPA for 60 min. These cells were collected into a new well plate which mapped to the original assay plate containing the cultured cells. We refer to this new well plate as the solution plate. After each wash step, the recovered solution was added to the solution plate and centrifuged to pellet the cells, and the excess fluid was then removed before the fluid from the next step was added. This process ensures that the cells still received the intended CPA removal procedure (which was designed to prevent osmotic damage). After completing the CPA removal process, the pelleted cells in the solution plate were resuspended in media and placed alongside the original assay plate in the incubator for recovery in culture. Figure 2.4 shows that there is no viability signal for the solution plate for any treatment, whereas the viability of the original plate ranged from 0% to around 80%. We also examined the wells under the microscope, which revealed that cells were present in the solution plate. This indicates that cells were collected into the solution phase during the CPA removal process, but that the cells were not viable or the number of viable cells was below the detection threshold. Overall, our results show that cell losses after CPA exposure cannot be attributed to detachment of viable cells from the culture surface.

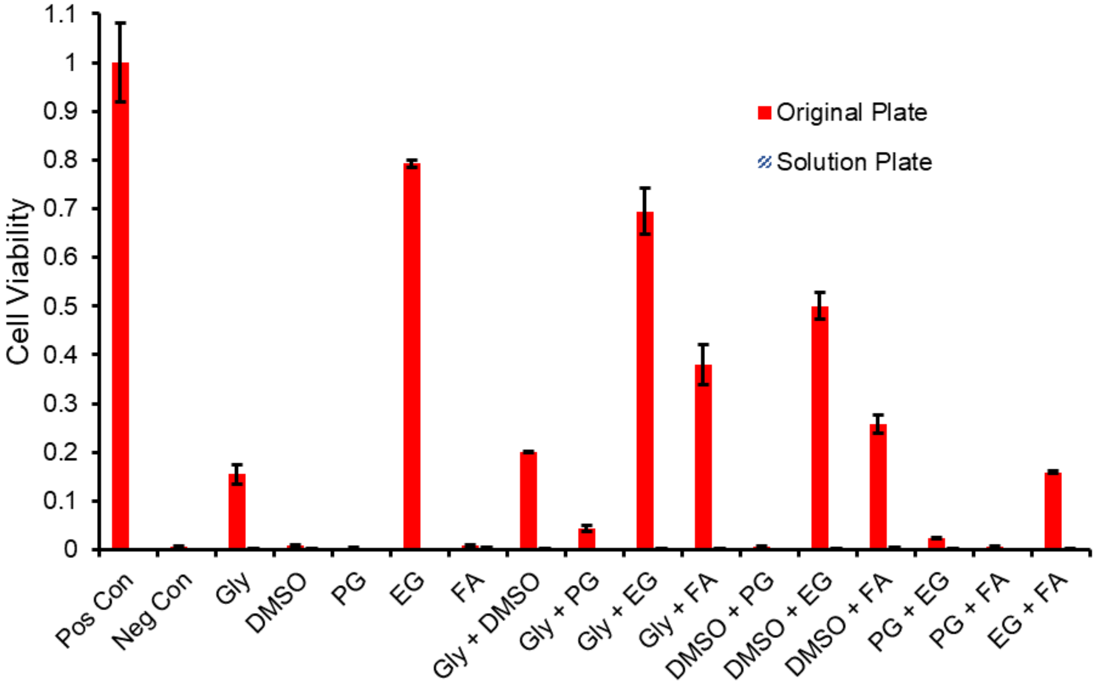

Figure 2.4. Comparison of viability between cells in the original well plate and those lost into the solution phase during CPA removal after exposure to 7 molal CPA solutions for 60 min. CPAs are abbreviated as follows: glycerol (Gly), propylene glycol (PG), ethylene glycol (EG), and formamide (FA). Solution from each wash step during CPA removal was collected into a new well plate (solution plate), which was cultured alongside the original plate for the assessment of viability. The viability of solution phase cells was negligible. Error bars represent the standard error of the mean.

2.4.4 Are Cell Losses Caused by Osmotic Damage?

CPA exposure can cause osmotic damage due to cell volume changes resulting from the flow of water and CPA across the cell membrane. Out of the five CPAs tested, glycerol has by far the lowest membrane permeability [56,62,110,116,129] and consequently is expected to cause the largest volume changes. As such, we designed our loading and removal procedures around cell volume predictions for glycerol. In particular, we designed multi-step procedures to ensure that the predicted cell volumes did not exceed the osmotic tolerance limits [29] (see Appendix A for more details). We assessed the potential for osmotic damage in both the CPA loading and removal regimes from an experimental and theoretical point of view, as described below.

2.4.4.1 CPA Loading

CPA loading typically causes cell shrinkage because water leaves the cells faster than CPA can enter. In our experiments, the conditions most likely to result in osmotic damage during CPA loading are exposure to either 7 molal or 10 molal glycerol. Figure 2.5 shows the predicted cell volume response during each of the loading steps for maximum glycerol concentrations of 7 and 10 molal (solid lines of panels A and B, respectively). For both glycerol concentrations, the minimum predicted volume is about 30% of the physiological cell volume, which is well above the osmotic tolerance limit. Also shown in Figure 2.5 are conservative predictions using a glycerol permeability 2x lower than the published value (dashed lines) [56]. While more extensive shrinkage is predicted in this case, the minimum predicted volume still exceeds the osmotic tolerance limit. These theoretical predictions demonstrate that the CPA loading methods that we used in our experiments are not expected to cause osmotic damage.

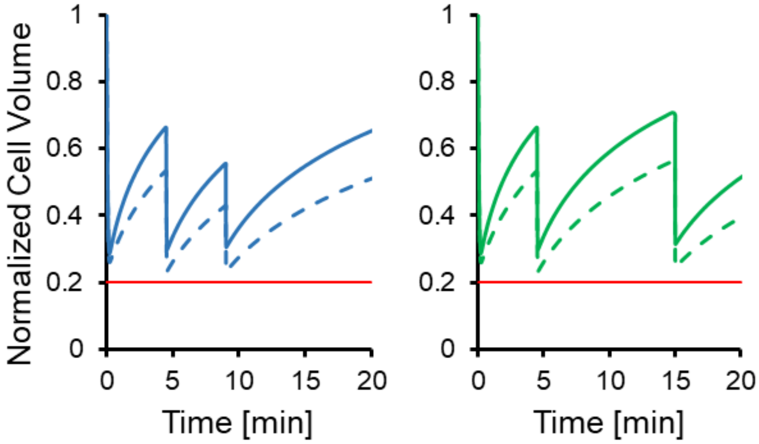

Figure 2.5. Cell volume predictions for multi-step glycerol loading procedures for exposure to 7 and 10 molal glycerol. Solid lines show predictions using published permeability values [56], while the dashed lines show predictions using a 2x lower glycerol permeability. The red line in both panels shows the lower osmotic tolerance limit [29]. In all simulations, a temperature of 25 °C was used.

Our experimental data also suggests that osmotic damage does not occur during CPA loading. Cell viability remained high (>87%) after exposure to 7 molal or 10 molal glycerol for up to 10 min, using the multi-step CPA addition processes depicted in Figure 2.5. Since the maximum cell shrinkage after exposure to 7 or 10 molal glycerol is predicted to occur in less than 1 min, osmotic damage from CPA loading should manifest itself in both 5 and 10 min exposures to glycerol. Therefore, the high cell viability observed for the 5 and 10 min glycerol exposures provides strong evidence that osmotic damage during CPA loading is negligible.

2.4.4.2 CPA Removal

During CPA removal, osmotic damage due to excessive cell swelling is the main concern. The potential for osmotic damage depends on the amount of CPA in the cell, which increases with the CPA concentration and exposure time. In our experiments, the condition most likely to cause osmotic damage during CPA removal is exposure to 10 molal glycerol for 60 min. This condition completely killed the cells, resulting in a viability of less than 1%. The condition next most likely to cause osmotic damage is exposure to 7 molal glycerol for 60 min, which resulted in a viability of 18%. In order to rule out osmotic damage as the main contributor to this loss in viability, we evaluated the 7 molal 60 min treatment using a more conservative CPA removal process in which the duration of each step was increased to 15 min (2-3 times longer than the standard procedure). As shown in Figure 2.6, the conservative CPA removal procedure is predicted to decrease the amount of cell swelling (panel B) compared to the standard procedure (panel A), which would be expected to reduce osmotic damage. However, the cell viability after CPA removal using the conservative method was only 15.5% ± 2%, which is nearly identical to the viability of 18.0% ± 0.7% obtained using the standard method (p-value of 0.27 for a two-sample t-test). This suggests that the loss of viability after 60 min exposure to 7 molal glycerol is due to toxicity and not osmotic damage.

Comparison of the results for 30 min and 60 min exposure to 7 molal glycerol provides further evidence that the observed cell losses cannot be attributed to osmotic damage. The viability was relatively high at 83% after a 30 min exposure to 7 molal glycerol but reduced to 18% after exposure to glycerol for 60 min. Cell volume predictions suggest that this reduction in viability is not caused by osmotic damage. As shown in Figure 2.6, the maximum predicted cell volume was actually higher after 30 min exposure to glycerol (using the standard CPA removal procedure) than after 60 min exposure using the more conservative CPA removal procedure. This indicates that 60 min exposure to glycerol is actually expected to result in less osmotic damage (when the conservative CPA removal process is used) and rules out osmotic damage as the cause of the lower viability.

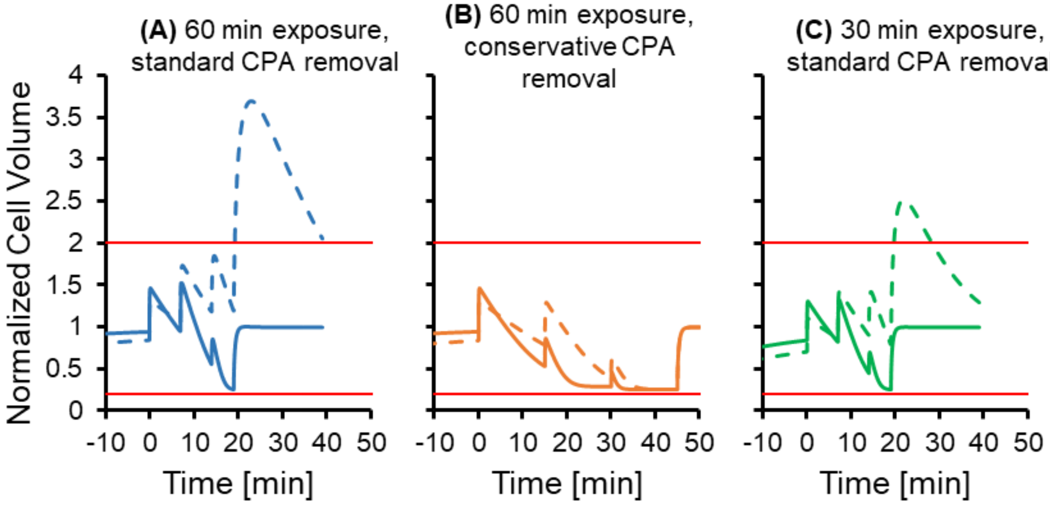

Figure 2.6. Cell volume predictions for multi-step CPA removal after exposure to 7 molal glycerol. Solid lines show predictions using published permeability values [56], while the dashed lines show predictions using a 2x lower glycerol permeability. Red lines show the osmotic tolerance limits [29]. Panel A shows the cell volume predictions after 60 min exposure to glycerol using standard hold times for each CPA removal step, while Panel B shows predictions when the step times are increased to 15 min each. In Panel C, cell volume predictions are shown after a 30 min exposure using standard hold times during CPA removal. In all simulations, a temperature of 25 °C was used.

The analysis above demonstrates that glycerol toxicity, rather than osmotic damage, is the most likely cause of the reduced cell viability after exposure to 7 molal glycerol for 60 min. Therefore, toxicity is likely the major cause of the reduced viability after exposure to 10 molal glycerol as well. To evaluate the potential for osmotic damage after exposure to 10 molal glycerol, we examined cell volume predictions during CPA removal (not shown). The maximum predicted cell volume after 30 min exposure to 10 molal glycerol is less than the maximum predicted cell volume after exposure to 7 molal glycerol for 60 min, which suggests that osmotic damage is negligible in this case. This only leaves the experimental group with 60 min exposure to 10 molal glycerol with potential osmotic damage. We cannot conclusively rule out osmotic damage in this case because the maximum predicted cell volume is higher than that for 60 min exposure to 7 molal glycerol. It is also difficult to experimentally assess osmotic damage after 60 min exposure to 10 molal glycerol because the resulting viability was very low (<1%), probably as a result of glycerol toxicity. Nonetheless, osmotic damage is unlikely because the glycerol removal process was designed to maintain cell volumes within the osmotic tolerance limits based on predictions using the published glycerol permeability [56]. Since the other CPAs have a much higher permeability than glycerol, osmotic damage is even less likely for the other CPAs.

2.4.5 Cell Losses are Caused by CPA Toxicity

Our results suggest that CPA toxicity is the main cause for the observed reduction in cell viability after exposure to CPA. We quantified toxicity by fitting a first-order kinetic model to the cell viability data, resulting in best-fit toxicity rates for each CPA mixture type at various concentrations. Figure 2.7 presents viability data and the corresponding toxicity rate fits for solutions containing a single CPA and for binary CPA mixtures (see Research Data section for the full data set). Overall, the fits are a reasonable match for the data, and the best-fit toxicity rate provides a convenient metric for comparing the toxicity of different CPA solutions.

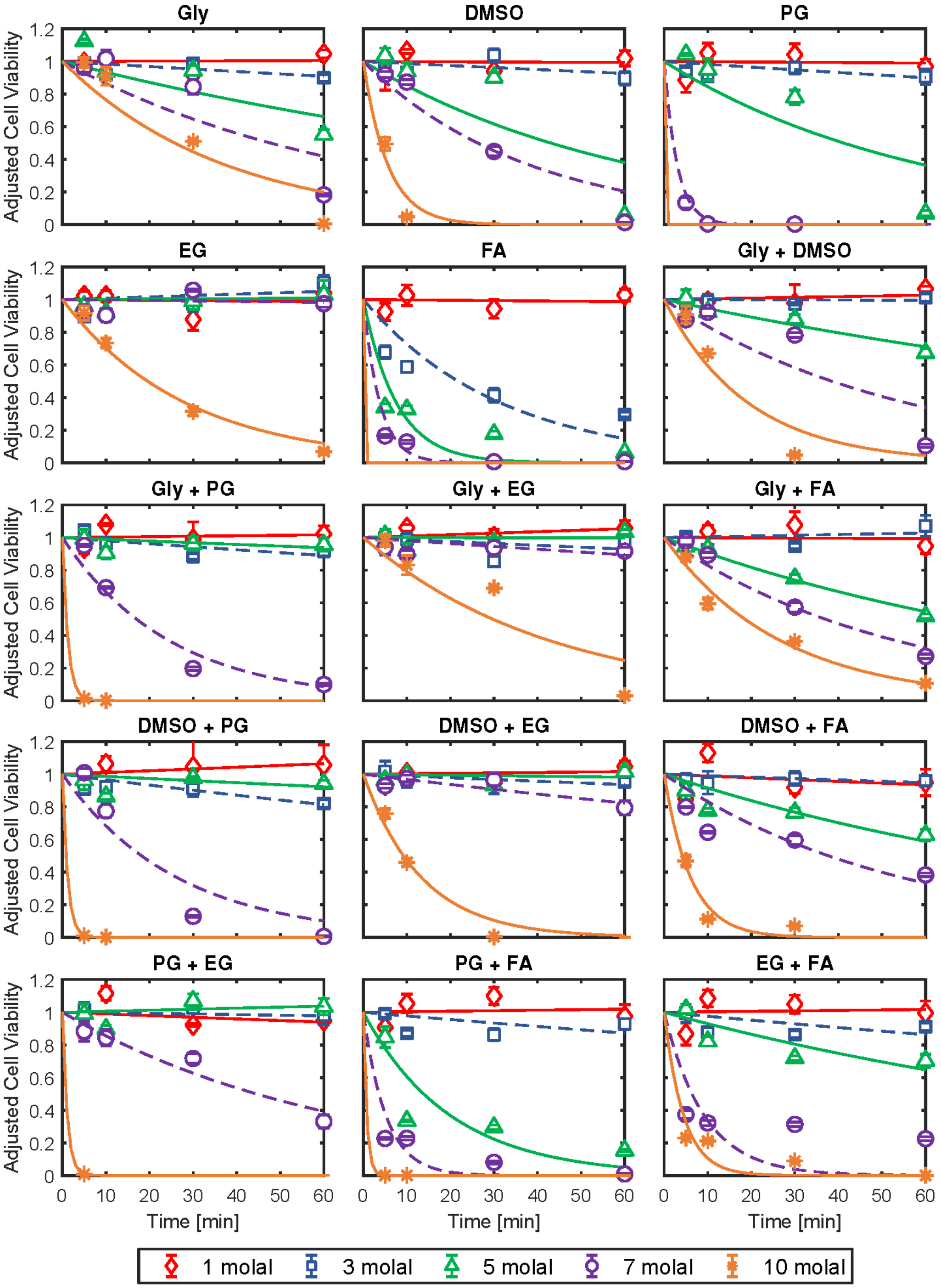

Figure 2.7. Cell viability after exposure to single CPA solutions and binary CPA mixtures. Lines show the best-fit toxicity rate models. Error bars represent the standard error of the mean. CPAs are abbreviated as follows: glycerol (Gly), propylene glycol

(PG), ethylene glycol (EG), and formamide (FA). Viability was adjusted to account for toxicity during CPA addition and removal as described in the methods section (see Eq. 2.6).

From the toxicity rate data, some common trends in CPA toxicity can be seen. Figure 2.8 compares the toxicity rates for solutions containing a single CPA. Our results show that ethylene glycol is one of the least toxic CPAs and formamide is one of the most toxic, which are common findings in previous studies of CPA toxicity [5,22,38,75,130]. However, there is a strong concentration dependence of the toxicity rates that is more nuanced. Formamide is the most toxic CPA up to a concentration of 5 molal, but at higher concentrations, propylene glycol toxicity increases dramatically and actually exceeds that of formamide. High propylene glycol toxicity has been reported in the oocyte and chondrocyte studies of Szurek and Eroglu [122], Jomha et al [75], and Almansoori et al [5]. Comparison of our results for propylene glycol and formamide reveals differing effects of concentration on the toxicity rate, which may reflect different mechanisms of CPA toxicity.

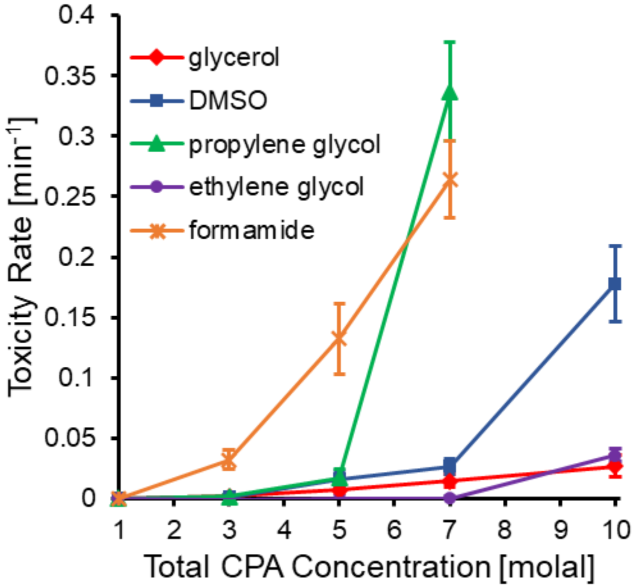

Figure 2.8. Best-fit toxicity rates for solutions containing a single CPA as a function of CPA concentration. It was not possible to measure a toxicity rate for propylene glycol or formamide at a concentration of 10 molal, as no viability was measured for any exposure time. Error bars represent the 95% confidence intervals of the best-fit toxicity rates.

Examination of the toxicity rates for the binary CPA mixtures also revealed some interesting trends, as shown in Figure 2.9. We split Figure 2.9 into two panels, with one panel showing all of the binary mixtures without propylene glycol and the other panel showing the mixtures with propylene glycol. The binary mixtures with propylene glycol exhibited a dramatic increase in toxicity at higher concentrations, similar to the spike in toxicity that was observed for propylene glycol on its own. In Almansoori et al [5], they also show that multi-CPA mixtures with propylene glycol are particularly toxic. Figure 2.9 also shows that glycerol + ethylene glycol is a favorable binary mixture, which has also been shown in Jomha et al [75].

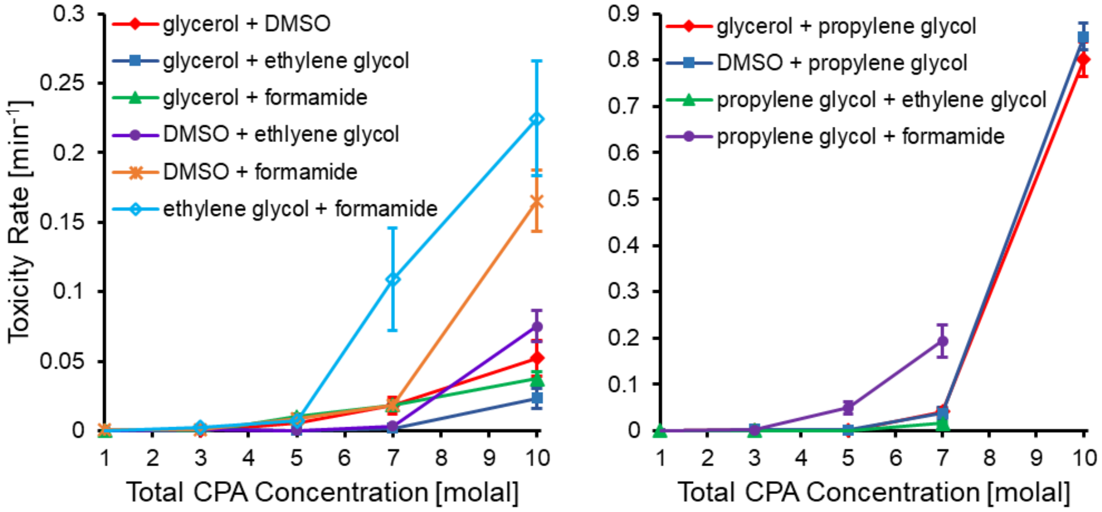

Figure 2.9. Best-fit toxicity rates for binary CPA mixtures. Left panel: binary CPA mixtures not containing propylene glycol. Right panel: binary CPA mixtures containing propylene glycol. Propylene glycol mixtures were the most toxic, and the toxicity rate axis scales are adjusted accordingly between the two panels. In the right panel, no viability was measured after exposure to 10 molal mixtures of propylene glycol + ethylene glycol and propylene glycol + formamide for any of the exposure times and therefore no toxicity rate could be measured. Error bars represent the 95% confidence intervals of the best-fit toxicity rates.

Figure 2.10 compares toxicity rates for single CPA solutions, binary mixtures, and ternary mixtures at a total CPA concentration of 7 molal. Our results highlight the general decrease in toxicity as more CPAs make up a mixture, as has been observed in several previous studies [4,5,46,47,50,75]. Figure 2.10 also showcases that some CPA interactions in a mixture are more beneficial than others. Within the ternary combinations shown in Figure 2.10, glycerol + DMSO + ethylene glycol was found to be the least toxic. This ternary CPA mixture was also found to be favorable in Jomha et al [75] and Almansoori et al [5].

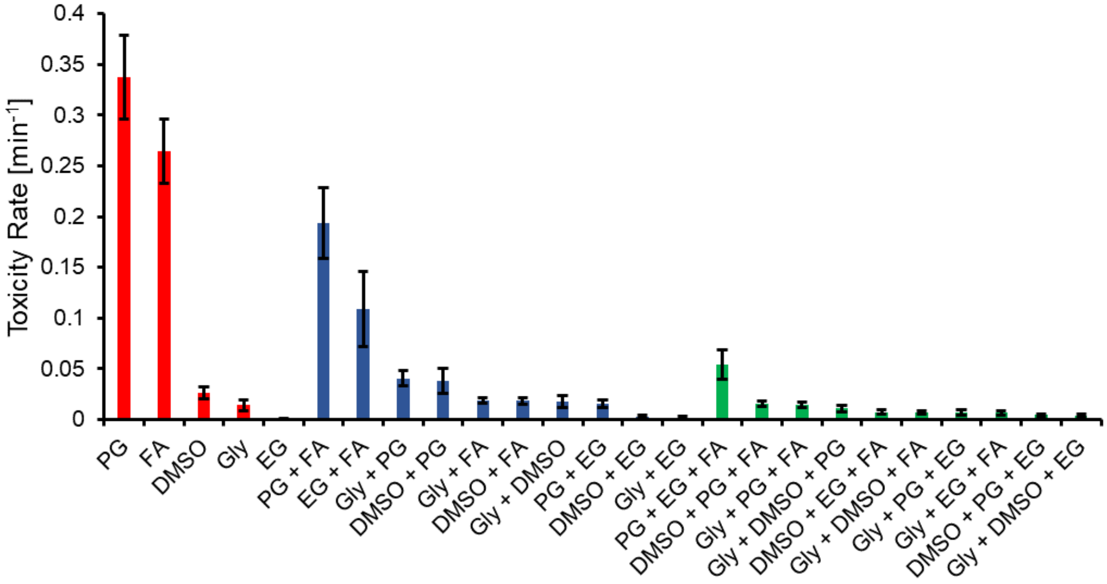

Figure 2.10. Best-fit toxicity rates for single CPA solutions, binary mixtures, and ternary mixtures at a total CPA concentration of 7 molal. CPAs are abbreviated as follows: glycerol (Gly), propylene glycol (PG), ethylene glycol (EG), and formamide (FA). To determine the toxicity rates for the ternary solutions it was assumed that toxicity was negligible during exposure to 1 molal and 3 molal solutions during CPA addition and removal. This is a reasonable assumption considering that none of the 1 molal toxicity rates were found to be statistically significant in this study, and the majority of 3 molal toxicity rates for binary solutions were not statistically significant. Moreover, even in cases where the 3 molal toxicity rate was significant, there is a negligible decrease in cell viability for relatively short exposure times of ~10 min (see Fig. 2.7), which is the case for the total time of the 3 molal CPA addition and removal steps. Error bars represent the 95% confidence intervals of the best-fit toxicity rates.

We can further investigate toxicity in multi-CPA mixtures through the lens of toxicity neutralization, as described by Fahy. In particular, Fahy [45,50] has described the neutralization of formamide toxicity by DMSO. Fahy showed the neutralization of formamide toxicity in rabbit renal cortical slices by adding various concentrations of DMSO to fixed formamide concentrations. Even though the total CPA concentration was higher in the resulting mixtures, Fahy observed that the mixtures were less toxic than the original formamide solutions on their own. As shown in Figure 2.11, we observed the same phenomenon in DMSO + formamide mixtures at some concentrations, but we observed even more substantial toxicity neutralization in glycerol + formamide mixtures. In particular, Figure 2.11 shows that a mixture containing 5 molal formamide and 5 molal glycerol is much less toxic than a solution containing 5 molal formamide on its own. A favorable glycerol + formamide interaction can be inferred from the model fit of Jomha et al [75], but to our knowledge, we are the first to report such a comprehensive case of formamide toxicity neutralization by glycerol.

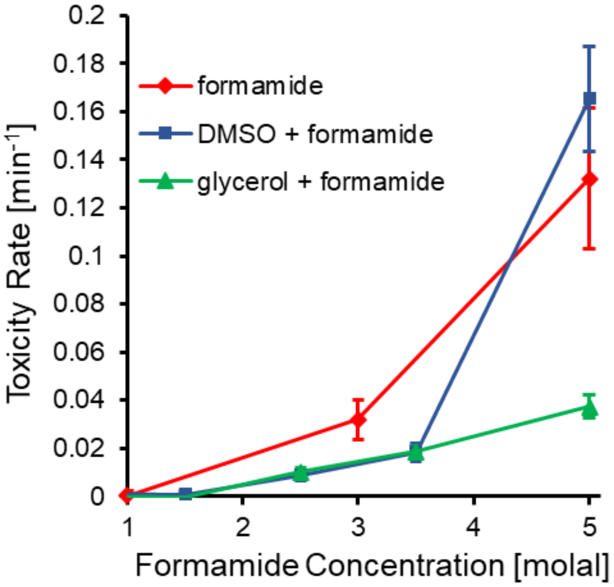

Figure 2.11. Synergistic effects of glycerol and DMSO on formamide toxicity. The toxicity rates for the three CPA compositions are plotted against formamide concentration. In the glycerol and DMSO mixtures, formamide makes up half the CPA concentration on a molal basis, resulting in a total CPA concentration that is twice what is reported on the x-axis. Error bars represent the 95% confidence intervals of the best-fit toxicity rates.

2.5 Conclusions and Future Directions

In this work, we have established an automated liquid handling methodology for high-throughput measurement of CPA toxicity in a 96-well plate format. This new approach makes it possible to randomize treatment locations on the well plate and precisely control the aspirate/dispense flow rate and timing, resulting in less experimental variability and more accurate results. Automated liquid handling also enables much higher throughput compared to manual pipetting, enabling faster generation of CPA toxicity data sets.

Using this new high-throughput approach, we were able to rapidly test 340 unique experimental conditions, including CPA mixtures containing glycerol, DMSO, propylene glycol, ethylene glycol, and formamide at various concentrations. Our results are consistent with some commonly observed trends, including the observation that ethylene glycol and glycerol are relatively non-toxic CPAs, formamide is a relatively toxic CPA, and that overall toxicity decreases as the number of CPAs in the mixture increases. Our results also confirm previous observations that the toxicity of formamide can be neutralized by addition of DMSO to the solution. Surprisingly, we observed even more significant neutralization of formamide toxicity from glycerol.

In the end, our goal is to create a robust toxicity model for multi-CPA vitrification solutions that can be implemented in our toxicity cost function approach for designing minimally toxic CPA equilibration methods [29]. In future work, we plan to use the data presented here to develop a multi-CPA toxicity model that accounts for multiple mechanisms of toxicity, including toxicity neutralization. In addition, we plan to carry out experiments at various temperatures, which will allow us to account for the temperature-dependence of CPA toxicity. We are currently integrating third-party hardware with the automated liquid handling system in order to control the temperature of the assay and source plates. Overall, the novel high-throughput approach described here is expected to enable quantification of CPA toxicity over a wide range of conditions, leading to the development of a comprehensive toxicity model that can be used for design of less toxic cryopreservation methods.

2.6 Conflicts of Interest

The authors have no conflicts of interest.

2.7 Acknowledgements

This work was supported from funding from the Hirsch Foundation and the National Institutes of Health (R01 EB027203).

2.8 Research Data

The full data sets (cell viability and adjusted cell viability) are made available in two Excel files in the Supplementary Material (see actual publication in *Cryobiology*).

GENERAL MASS TRANSFER MODEL OF TISSUES FOR CRYOPRESERVATION APPLICATIONS

In-Preparation

3. GENERAL MASS TRANSFER MODEL OF TISSUES FOR CRYOPRESERVATION APPLICATIONS

3.1 Abstract

Successful cryopreservation of complex specimens, such as tissues and organs, would greatly benefit both the medical and scientific research fields. Vitrification is one of the most promising techniques for complex specimen cryopreservation, but toxicity remains a major challenge due to the high concentration of cryoprotectants (CPAs) needed to vitrify. Our group has approached toxicity through mathematical optimization, and in previous works, we developed less toxic CPA equilibration methods for single cells by minimizing a toxicity cost function. We also have proposed a way to write a toxicity cost function at the tissue level. However, in that work, the toxicity cost function was informed by a mass transfer model based on the framework of Fick's law. Fick's law can be an adequate model for some tissues, but it is not applicable to tissues in general mainly due to its dilute assumption and not accounting for tissue size changes. Our goal is to develop a general approach to minimizing the toxicity of tissue vitrification protocols. In this work, we propose a general model for mass transfer in tissues. To accomplish this, we accounted for cellular effects by augmenting an acellular mixture theory model in the literature for articular cartilage. We show that the augmented model can accurately predict mass transfer within cartilage and pancreatic islets, two tissue types with vastly different properties. This demonstrates the general utility of the model, providing a promising foundation for future efforts to design improved tissue cryopreservation methods.

3.2 Introduction

The field of cryopreservation has had many successes in preserving biological specimens over long time scales. Successful cryopreservation of single cells, both bacterial and mammalian, has provided a variety of specimens to the research community and has also helped to facilitate animal breeding and human reproduction [9,34,68,92,107,115]. Single cells represent the simplest specimens that can be cryopreserved, but their successful cryopreservation protocols are not. Decades have been spent by the cryobiology community to understand the intricacies of cryopreserving the simplest specimens. Moving on from single cells, more complex biological specimens such as tissues and organs prove to be much more challenging to successfully cryopreserve [47,48]. The task of cryopreserving these specimens is exceptionally challenging, but their successful cryopreservation would have untold benefits for the public health by allowing for the banking of tissues and organs. Successful complex specimen banking would immensely improve the effectiveness of transplantations, research, and emergency preparedness [48,61,90].

Successful suspension-phase single cell cryopreservation usually relies on the technique of slow cooling. Slow cooling, likes its name suggests, involves slow cooling rates with the addition of low concentrations of permeating CPAs. Extracellular ice is allowed to form and the CPAs counteract excessive cell shrinkage. However, it is thought that more complex specimens (adherent cells, tissues, and organs), which cannot tolerate extracellular ice formation, need the promising technique of vitrification to be employed [49,76,94,121]. Vitrification eliminates the extracellular ice problem but poses two new problems stemming from the high concentration of CPAs required to suppress ice formation. The high concentrations of CPAs can induce excessive volume excursions (osmotic damage) of the specimen and impart unacceptable toxicity [29,38,40,47,86]. Osmotic damage can be successfully prevented by incrementally adding and removing CPA do reduce the extent of the volume excursions [29,38,59,86,98], but toxicity is not as straightforward and proves to be the single greatest challenge for successful vitrification [5,46,47,75].

The problem of toxicity reduces down to a toxicity minimization problem, as the conventional CPAs used in the field will inevitably have some detrimental effects to the specimen. CPA toxicity can be minimized by finding trends within large toxicity data repositories (empirical approach) or mathematical models can be generated that minimize a function representing toxicity. In this work, we will be focusing on mathematical modeling of tissues, and the crux of any modeling approach is a mass transfer model that predicts both the spatial and temporal distribution of CPAs, as toxicity is dependent on the distribution. However, there are many tissue-based phenomena that need to be considered when developing a mass transfer model, and the large concentration of CPAs used for vitrification poses an immense challenge by squarely placing the mass transfer within the non-dilute regime. In a previous discussion of tissue modeling [132], we highlighted some of the major considerations that need to be addressed: 1) non-dilute mass transfer in the extracellular space, 2) coupling between extracellular and cell membrane mass transfer, 3) fixed electrical charges on the extracellular matrix (generates an unequal ion distribution between the intra- and extra-tissue space, influencing the flux of all fluid phase species), and 4) tissue volume changes. The current state of mass transfer modeling of tissues within cryobiology is lacking because there is not one model that accounts for all of the phenomena. Some phenomena are more or less important depending on the tissue but they are nevertheless present, and our goal is to develop a general mass transfer model that accounts for all phenomena. If a tissue's complete response to any CPA addition and removal protocol cannot be predicted, the least toxic protocol can never be determined from a mathematical standpoint.

In the literature, the most common way to model mass transfer is using Fick's second law. However, Fick's law is based on a dilute framework and does not account for cell membrane transfer, fixed charges, or tissue size changes. Fick's law can serve as the mass transfer model for successful cryopreservation of tissues, such as a recent series of papers for articular cartilage [74,76,119], but the approach is limited to only the vitrification of cartilage, since the diffusion coefficients were fit for the CPA concentrations used and cartilage has small volume changes. Fick's law has also been coupled with cell membrane transport but this only accounts for one extra phenomenon [14,27,32,67]. Benson et al [12] has taken this approach a step further by also accounting for tissue size changes, but the approach was only applicable to pancreatic islets under the assumption that there was a constant volume ratio between the intra- and extracellular space. Fick's law has the potential to be molded for a specific tissue but some phenomena will be lacking and the model is not general. Other modeling approaches have focused primarily on non-dilute extracellular transfer [137], while others have focused on non-dilute extracellular and cell membrane transfer with tissue size change predictions [30]. Altogether, there is not one modeling paradigm that describes all of the phenomena nor can be applied outside of a limited application window.

The closest modeling paradigm to describing all of the phenomena comes from the articular cartilage model presented by Abazari et al [1]. The model is rooted in the triphasic theory of articular cartilage as proposed by Lai et al [82] and subsequently modified by Shaozhi and Pegg [118] for applications in cryopreservation by adding CPA as a fourth phase. Abazari et al [1] furthers the work of Shaozhi and Pegg [118] by incorporating the non-dilute chemical potential expressions of Elliot et al [35] and Elmoazzen et al [37]. Overall, Abazari et al [1] represents cartilage as a four-component system, which is comprised of the solid matrix, water, CPA, and salt (NaCl). However, as they are considering mass transfer in the low cell density tissue of cartilage, they do not account for cells. To address this limitation for applications of this model for tissues in general, we have augmented their model by adding cells and accounting for transport of both water and CPA across the cell membrane.

With the model outlined in this work, we can address each tissue-based phenomenon, which all have impacts on the design of CPA addition and removal protocols. As such, we postulate that a model that accounts for all of the phenomena can be applied to any tissue, as moving from one tissue to another is just a matter of changing parameters. To show the feasibility of such an approach we have applied our cell augmented model to pancreatic islets, and we show that our model can match islet predictions found in the literature. As such, we have shown that our modeling approach can be used for two very different tissues—a stiff low cell density tissue in articular cartilage and an elastic high cell density tissue in pancreatic islets. This model will allow us to more accurately predict the least toxic CPA addition and removal protocol for a tissue. Moving forward, we can use this model within our toxicity cost function approach, where we have shown a mathematical framework that can minimize toxicity for single cells [11,28,29]. In a past work, we proposed a toxicity cost function for tissues, but the mass transfer model was based on Fick’s law [13]. With the model presented in this work used within the toxicity cost function framework, we can create a more robust approach to minimizing toxicity of tissues in general.

3.3 Model Formalism

3.3.1 Model Description and Definition of State Variables

We consider one-dimensional transport in a thin slab of tissue. One side of the tissue is insulated to mass transport and the opposite side is exposed to a bath solution. The insulated side of the tissue is fixed in space and the bath side is free to move as governed by the fluid fluxes and mechanical properties of the tissue. As such, this model is a classical one-dimensional moving boundary problem. Figure 3.1 shows the general geometry of the model.

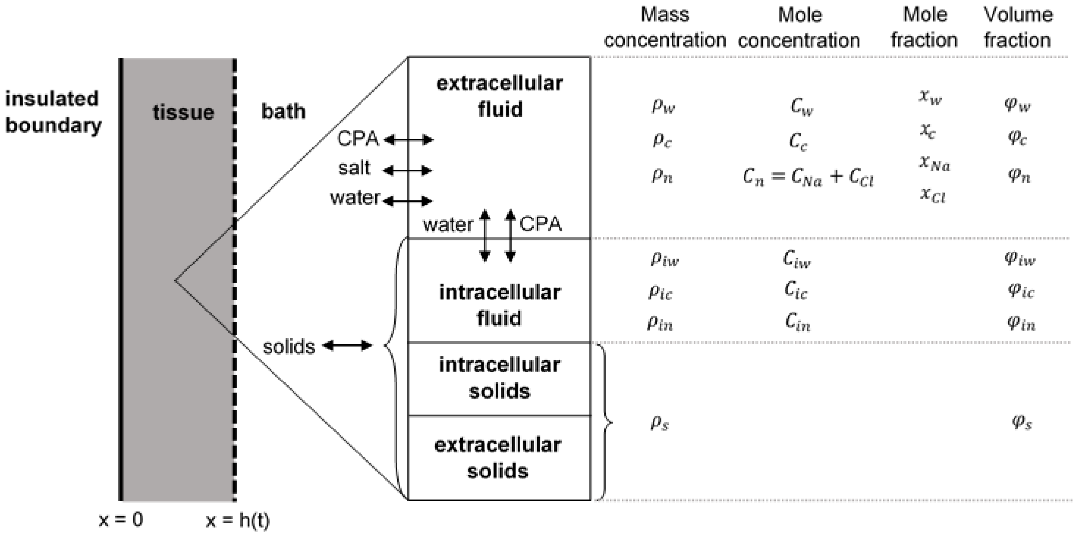

Figure 3.1. Schematic illustrating modeling approach.

As shown in the Figure 3.1, the tissue is divided into four compartments: extracellular fluid, intracellular fluid, intracellular solids, and extracellular solids. Water, CPA, and salt can move through the interstitial space in the x-direction, and this can result in movement of solids in the x-direction as well. The cells are considered to be embedded in the extracellular solids and hence move with the solids. The intracellular fluid can exchange water and CPA with the extracellular fluid.

Various variables are used to describe the state of each of these compartments, as depicted in Figure 3.1. Subscripts are used to specify the chemical species and the compartment: iw, ic, s, n, w, and c represent intracellular water, intracellular CPA, solids, extracellular salt, extracellular water, and extracellular CPA, respectively.

The mass concentration and volume fraction are defined per tissue volume and are used to write the continuity equations. The volume fraction of species i can be calculated from the mass concentration as follows:

$$\varphi_{\mathrm{i}} = \frac{\rho_i}{\bar{\rho}_i} \tag{3.1}$$

where $\bar{\rho}_i$ is the density of pure i. The volume fractions of extracellular and intracellular salt were considered to be negligible.

The mole concentrations and mole fractions are used to represent driving forces for transport and are defined based on the fluid volume in which the chemical species is dissolved. For the extracellular fluid, the mole concentrations of water and CPA can be calculated from the mass concentrations as follows:

$$C_w = \frac{\rho_w}{M_w(\varphi_w + \varphi_c)} \tag{3.2a}$$

$$C_c = \frac{\rho_c}{M_c(\varphi_w + \varphi_c)} \tag{3.2b}$$

where M_i represents the molecular weight of species i. For the intracellular fluid, the mole concentrations of water and CPA can be expressed similarly:

$$C_{iw} = \frac{\rho_{iw}}{M_w(\varphi_{iw} + \varphi_{ic})} \tag{3.2c}$$

$$C_{ic} = \frac{\rho_{ic}}{M_c(\varphi_{iw} + \varphi_{ic})} \tag{3.2d}$$

The concentration expressions for the salt are slightly more complicated. The extracellular matrix (solids) is negatively charged and contains fixed positively charged sodium counterions that also contribute to the driving forces for transport. However, these fixed charges cannot move freely through the extracellular fluid and move with the matrix. The mole concentration of chloride ions can be calculated from the mass concentration as follows:

$$C_{Cl} = \frac{\rho_n}{M_n(\varphi_w + \varphi_c)} \tag{3.2e}$$

The mole concentration of sodium ions includes the counterions for the chloride ions, as well as the fixed charges:

$$C_{Na} = C_{Cl} + C_{fc} \tag{3.3}$$

The total mole concentration of salt ions is then the sum of the sodium and chloride concentrations:

$$C_n = C_{Cl} + C_{Na} \tag{3.4}$$

While the concentration of fixed charges can change as the tissue shrinks and swells, the number of fixed charges per volume of solids does not change. This allows us to express the fixed charge concentration at any time in terms of a reference fixed charge concentration (C_{fc}^{o}):

$$C_{fc} = C_{fc}^{o}\left(\frac{\varphi_w^o + \varphi_c^o}{\varphi_s^o}\right)\left(\frac{\varphi_s}{\varphi_w + \varphi_c}\right) \tag{3.5a}$$

The mole concentration of intracellular salt can be expressed in a similar manner. Since we consider salt to be impermeable to the cell membrane, the moles of intracellular salt per solids volume remains constant. This allows the intracellular salt concentration at any time to be expressed in terms of a reference initial concentration (C_{in}^{o}):

$$C_{in} = C_{in}^{o}\left(\frac{\varphi_{iw}^{o} + \varphi_{ic}^{o}}{\varphi_{s}^{o}}\right)\left(\frac{\varphi_{s}}{\varphi_{iw} + \varphi_{ic}}\right) \qquad 3.5b$$

Finally, we can express the mole fraction of species i in the extracellular fluid in terms of the mole concentrations as follows:

$$x_i = \frac{C_i}{C_w + C_c + C_n} \qquad 3.6$$

3.3.2 Transport Equations

We begin by writing continuity equations based on the six mass concentrations shown in Figure 3.1. Movement of each component in the x-direction is expressed in terms of its average velocity (u), while exchange of water and CPA across cell membranes is expressed in terms of the two-parameter membrane transport model, as described below. This yields the following continuity equations:

$$\frac{\partial \rho_w}{\partial t} + \frac{\partial(\rho_w u_w)}{\partial x} + \frac{\partial V_{iw}}{\partial t}\eta\varphi_s\bar{\rho}_w = 0 \qquad 3.7a$$

$$\frac{\partial \rho_c}{\partial t} + \frac{\partial(\rho_c u_c)}{\partial x} + \frac{\partial V_{ic}}{\partial t}\eta\varphi_s\bar{\rho}_c = 0 \qquad 3.7b$$

$$\frac{\partial \rho_n}{\partial t} + \frac{\partial(\rho_n u_n)}{\partial x} = 0 \qquad 3.7c$$

$$\frac{\partial \rho_{iw}}{\partial t} + \frac{\partial(\rho_{iw} u_s)}{\partial x} - \frac{\partial V_{iw}}{\partial t}\eta\varphi_s\bar{\rho}_w = 0 \qquad 3.7d$$

$$\frac{\partial \rho_{ic}}{\partial t} + \frac{\partial(\rho_{ic} u_s)}{\partial x} - \frac{\partial V_{ic}}{\partial t}\eta\varphi_s\bar{\rho}_c = 0 \qquad 3.7e$$

$$\frac{\partial \rho_s}{\partial t} + \frac{\partial(\rho_s u_s)}{\partial x} = 0 \qquad 3.7f$$

where V_{iw} is the intracellular water volume per cell, V_{ic} is the intracellular CPA volume per cell, and η is a constant term describing the cell density in the tissue (as defined in more detail below). These continuity equations follow from those given by Abazari et al [1], with the addition of intracellular components and terms describing cell membrane transport. These terms are based on the classic two-parameter membrane transport model [79], which gives the rate of change of intracellular water volume and intracellular CPA volume for a single cell in terms of concentration driving forces:

$$\frac{\partial V_{iw}}{\partial t} = L_p A_{cell} RT(C_{ic} + C_{in} - C_c - C_n) \qquad 3.8a$$

$$\frac{\partial V_{ic}}{\partial t} = P_c A_{cell} \bar{v}_c (C_c - C_{ic}) \qquad 3.8b$$

In these equations, L_p is the hydraulic conductivity, P_c is the CPA permeability, A_{cell} is the cell membrane surface area, $\bar{v}_c$ is the CPA molar volume, R is the universal gas constant, and T is temperature. The intracellular salt concentration (C_{in}) represents the net osmotic contributions of all intracellular salts. In the two-parameter formalism, salt is considered to be impermeable to the cell membrane.

To use these membrane transport equations in the continuity equations, it was necessary to relate the volume changes for a single cell to the corresponding rate of transport between the intracellular fluid and extracellular fluid per tissue volume. This was accomplished by defining a constant term η to describe the cell density, which represents the number of cells per volume of solids. This term is constant because the cells are embedded in the solids and move with the solids. The number of cells per tissue volume can then be calculated as $\eta\varphi_s$. Also, η is used to interconvert between intracellular volume fractions and single cell volumes as follows:

$$V_{iw} = \frac{\varphi_{iw}}{\eta\varphi_s} \qquad 3.9a$$

$$V_{ic} = \frac{\varphi_{ic}}{\eta\varphi_s} \qquad 3.9b$$

If we look back at the continuity expressions, we notice that the only unknowns left are the component velocities. To describe the velocity field, we relate the velocities to component chemical potential gradients, as described by Abazari et al [1]. The resulting multicomponent momentum balance is given below:

$$-\rho_w \frac{\partial \mu_w}{\partial x} = f_{cw}(u_w - u_c) + f_{ws}(u_w - u_s) + f_{nw}(u_w - u_n) \qquad 3.10a$$

$$-\rho_c \frac{\partial \mu_c}{\partial x} = f_{cw}(u_c - u_w) + f_{cs}(u_c - u_s) \qquad 3.10b$$

$$-\rho_n \frac{\partial \mu_n}{\partial x} = f_{nw}(u_n - u_w) \qquad 3.10c$$

where μ_i is the chemical potential of component i, and f_{ij} is the frictional coefficient between components i and j. It should be noted that we only have three equations and four unknown velocities. A volume balance can be used to define a fourth expression:

$$u_s(\varphi_s + \varphi_{iw} + \varphi_{ic}) + u_c\varphi_c + u_w\varphi_w = 0 \qquad 3.11$$

However, one still has to define the frictional coefficients in the above momentum balances, as well as the chemical potential gradients. The frictional coefficients are defined by Abazari et al [1] as follows, where D_{cw} and D_{nw} are the diffusivities of CPA and salt in water, and K_{cs} and K_{sw} are the permeabilities of CPA and water in the tissue:

$$f_{cw} = \frac{RT(\varphi_w + \varphi_c)C_c}{D_{cw}} \qquad 3.12a$$

$$f_{nw} = \frac{RT(\varphi_w + \varphi_c)C_{Cl}}{D_{nw}} \qquad 3.12b$$

$$f_{cs} = \frac{\varphi_c^2}{K_{cs}} \qquad 3.12c$$

$$f_{ws} = \frac{\varphi_w^2}{K_{sw}} \qquad 3.12d$$

Chemical potential expressions follow from Abazari et al [1] and are defined below:

$$\mu_w = \mu_w^* + \frac{P}{\bar{\rho}_w} - \frac{RT}{M_w}(1 - x_w)(1 + B_c x_c) \qquad 3.13a$$

$$\mu_c = \mu_c^* + \frac{P}{\bar{\rho}_c} + \frac{RT}{M_c}\left(\ln(x_c) + 0.5x_w^2 - B_c x_w (1 - x_c)\right) \qquad 3.13b$$

$$\mu_n = \mu_n^* + \frac{RT}{M_n}(\ln(x_{Na} x_{Cl}) + x_w^2 + 2B_c x_w x_c) \qquad 3.13c$$

In the above expressions, B_c is the second osmotic virial coefficient which is a constant, and we do not need to define the reference chemical potentials (μ_i^*) as only the chemical potential gradients are needed.

The last unknown in the chemical potential expressions is the pressure (P). This pressure is the gauge pressure defined relative to the pressure in the bath. The pressure in the tissue can be expressed in terms of a reference gauge pressure (P^o) and an elastic pressure that develops due to tissue strain:

$$P = P^o + P_{elastic} \qquad 3.14$$

Assuming a linear stress/strain relationship for compressive and tensile deformations yields:

$$P_{elastic} = H_A e \tag{3.15}$$

where the aggregate modulus of elasticity (H_A) is defined as a constant for both compressive and tensile deformations. The strain (e) can be related to the deviation in the solids volume fraction from the reference point:

$$e = \frac{\varphi_s^o}{\varphi_s} - 1 \tag{3.16}$$

3.3.3 Variable Transform to Fix the Size of the Spatial Domain

To numerically solve the system of equations defined above, it is necessary to address the moving tissue boundary. Such a problem can be classified as a mass transfer analog to a classical one-dimensional Stefan problem where several solution strategies have been proposed [58,80,81]. We adopted a boundary immobilization method which fixes the domain size through coordinate transform [81]. The transform is defined below:

$$\alpha = \frac{x}{h} \tag{3.17}$$

where h is the location of the tissue/bath interface (see Fig. 3.1). Transforming the problem is rather straightforward as there are only two unique spatial derivatives of first order: the chemical potential gradients and the flux gradients. These spatial gradients can be transformed through product rule as shown below:

$$\frac{\partial \mu_i}{\partial x} = \frac{1}{h}\frac{\partial \mu_i}{\partial \alpha} \tag{3.18a}$$

$$\frac{\partial(\rho_i u_i)}{\partial x} = \frac{1}{h}\frac{\partial(\rho_i u_i)}{\partial \alpha} \tag{3.18b}$$

The temporal gradient is more complicated but follows from the definition of the total derivative in both x and α space:

$$\frac{\partial \rho_i}{\partial t}_x = \frac{\partial \rho_i}{\partial t}_\alpha - \frac{\alpha}{h}\frac{dh}{dt}\frac{\partial \rho_i}{\partial \alpha} \qquad 3.19$$

It should be noted that the cell volume derivatives do not need to be transformed into the new domain. This is because the cell volume derivatives are only used to describe flux between the intracellular and extracellular fluid in the continuity equations and are not solved directly to determine cell volumes as a function of time. Since these cell volume derivatives are represented by concentration variables that are already transformed, the derivatives are already described in the new domain.

Looking at the transformed equations, we see that we need an expression for the domain width (h), as well as its derivate (dh/dt). The derivative, or labeled as the Stefan condition [57] in classical problems, provides closure, and for our problem, is governed by a mass balance at the boundary:

$$\frac{dh}{dt} = u_s(\alpha = 1) \qquad 3.20$$

With the Stefan condition defined, h follows from the integration of Equation 3.20:

$$h(t + \Delta t) = h(t) + u_s(\alpha = 1, t)\Delta t \qquad 3.21$$

However, Equation 3.21 is prone to greater tissue size changes than expected, as we see double the expected tissue shrinkage upon CPA addition when comparing results to Abazari et al [1] (see Fig. 3.2 in Results and Discussion). Instead, we defined h using a mass balance on solids within the entire tissue:

$$h = \frac{\rho_s^o h^o}{\int \rho_s \partial \alpha} \qquad 3.22$$

3.3.4 The Physiological Reference State

Typically, tissue properties are measured and reported in the literature under normal physiological conditions. Thus, we define a physiological reference state in which the tissue is in equilibrium with a normal physiological solution and use this as a basis for the mass transfer simulations. We begin by defining the following physiological tissue properties (superscript naught): tissue thickness (h^o), fixed charge concentration (C_{fc}^o), solids volume fraction (φ_s^o), and intracellular water volume fraction (φ_{iw}^o). The values of these parameters can be estimated from experimental data reported in the literature. Given these parameters, we can determine the state of the extracellular water, extracellular salt, and intracellular salt, as described below.

Since the tissue and physiological bath are at equilibrium, we can equate the water and salt chemical potentials:

$$\mu_w^{tissue} = \mu_w^* + \frac{P^o}{\bar{\rho}_w} - \frac{RT}{M_w}(1 - x_w^o) = \mu_w^{bath} \qquad 3.23a$$

$$\mu_n^{tissue} = \mu_n^* + \frac{RT}{M_n}\left(\ln(x_{Na}^o x_{Cl}^o) + {x_w^o}^2\right) = \mu_n^{bath} \qquad 3.23b$$

We assume that the physiological bath is an aqueous solution with sodium and chloride concentrations both equaling 150 mM. As such, the bath chemical potentials can be calculated. Note that the bath chemical potential expressions lack the pressure term because the bath is at a gauge pressure of zero, and the reference chemical potentials cancel out between the tissue and the bath. To solve these equations, we first rewrite the mole fractions in terms of concentrations:

$$x_i^o = \frac{C_i^o}{C_w^o + C_{Cl}^o + C_{Na}^o} \qquad 3.23c$$

The concentration of sodium can be expressed in terms of the fixed charge concentration:

$$C_{Na}^{o} = C_{Cl}^{o} + C_{fc}^{o} \qquad 3.23d$$

We can find the concentration of extracellular water directly through Equation 3.2a:

$$C_{w}^{o} = \frac{\bar{\rho}_{w}}{M_{w}} \qquad 3.23e$$

This reduces the number of unknowns to two (P^{o} and C_{Cl}^{o}), and Equations 3.23a and 3.23b can be solved directly for the unknowns. The final unknown in the extracellular space is the volume fraction of extracellular water, which can be found through a volume fraction balance:

$$\varphi_{s}^{o} + \varphi_{iw}^{o} + \varphi_{w}^{o} = 1 \qquad 3.23f$$

Lastly, we finish defining our physiological reference state by describing the intracellular salt. At equilibrium, the intracellular and extracellular salt concentrations must be equal, resulting in:

$$C_{in}^{o} = C_{n}^{o} = 2C_{Cl}^{o} + C_{fc}^{o} \qquad 3.23g$$

3.3.5 Initial Conditions

Initially, we assume that the tissue is in equilibrium with a bath of known composition. In our simulations we used a bath composition that was identical to a normal physiological solution, but with a small amount of CPA. This small amount of CPA was included because the chemical potential expression for CPA contains the natural logarithm of the CPA mole fraction, which is undefined for a mole fraction of zero. Specifically, we used a bath composition with sodium and chloride concentrations again equaling 150 mM and a CPA concentration of 0.1 mM. Below, we present a general strategy for determining the initial conditions within the tissue that can be applied for any initial bath composition.

We can equate the chemical potentials in the tissue and the bath, but this time we must consider the chemical potential of CPA in addition to water and salt:

$$\mu_w^{tissue} = \mu_w^* + \frac{P}{\bar{\rho}_w} - \frac{RT}{M_w}(1 - x_w)(1 + B_c x_c) = \mu_w^{bath} \qquad 3.24a$$

$$\mu_c^{tissue} = \mu_c^* + \frac{P}{\bar{\rho}_c} + \frac{RT}{M_c}\left(\ln(x_c) + 0.5x_w^2 - B_c x_w (1 - x_c)\right) = \mu_c^{bath} \qquad 3.24b$$

$$\mu_n^{tissue} = \mu_n^* + \frac{RT}{M_n}(\ln(x_{Na} x_{Cl}) + x_w^2 + 2B_c x_w x_c) = \mu_n^{bath} \qquad 3.24c$$

Mole fractions can be written in terms of concentrations as shown in Equation 3.6, and the concentration of sodium is dependent on the chloride and fixed charge concentration, as shown in Equation 3.3. The fixed charge concentration can be defined in terms of the physiological reference state as follows (see Eq. 3.5a):

$$C_{fc} = C_{fc}^o \left(\frac{\varphi_w^o}{\varphi_s^o}\right)\left(\frac{\varphi_s}{\varphi_w + \varphi_c}\right) \qquad 3.24d$$

The concentrations of extracellular water and CPA can be written in terms of their volume fractions using Equations 3.2a and 3.2b, with Equation 3.1 substituted in for the mass concentration:

$$C_i = \frac{\bar{\rho}_i \varphi_i}{M_i(\varphi_w + \varphi_c)} \qquad 3.24e$$

The pressure can be written in terms of the solids volume fraction by using Equations 3.14-3.16:

$$P = P^o + H_A\left(\frac{\varphi_s^o}{\varphi_s} - 1\right) \qquad 3.24f$$

At this point, we have written Equations 3.24a-3.24c in terms of φ_s, φ_w, φ_c, and C_{Cl}, resulting in 3 equations and 4 unknowns. To solve this problem, we must describe the state of the intracellular components. At equilibrium, the extracellular and intracellular concentration for both the CPA and salt must be equal. For the CPA, we can express the concentrations in terms of volume fractions (e.g. Eq. 3.24e) and set them equal, resulting in:

$$\frac{\varphi_c}{(\varphi_w + \varphi_c)} = \frac{\varphi_{ic}}{(\varphi_{iw} + \varphi_{ic})} \qquad 3.24g$$

For the salt, we write the extracellular concentration by combining Equations 3.3 and 3.4, and set that equal to the intracellular salt concentration defined using Equation 3.5b:

$$2C_{Cl} + C_{fc} = C_{in}^{o}\left(\frac{\varphi_{iw}^{o}}{\varphi_s^{o}}\right)\left(\frac{\varphi_s}{\varphi_{iw} + \varphi_{ic}}\right) \qquad 3.24h$$

Finally, we write the overall volume fraction balance as:

$$\varphi_s + \varphi_w + \varphi_c + \varphi_{iw} + \varphi_{ic} = 1 \qquad 3.24i$$

This results in six equations (Eqs. 3.24a-c and Eqs. 3.24g-i) and six unknowns (φ_s, φ_w, φ_c, C_{Cl}, φ_{iw} and φ_{ic}). After the unknowns are found, the final part is to define the initial tissue thickness by using Equation 3.22:

$$h = \frac{\varphi_s^{o} h^{o}}{\varphi_s} \qquad 3.24j$$

3.3.6 Boundary Conditions

Within the one-dimensional domain, we have two boundaries to consider: the insulated boundary and the bath boundary. The insulated boundary is the most straightforward to describe since it is an insulated surface to mass transfer. As such, there is no flux of any species i across the boundary and therefore each velocity u_i is equal to zero (no penetration boundary condition):

$$u_i = 0 \tag{3.25}$$

For the bath boundary, we notice that the addition of cells complicates calculations, since there is a finite transport time across the cell membrane. We examined two possibilities for the bath boundary conditions. The first is an instantaneous equilibration between the extracellular and intracellular space. In this case, the bath boundary conditions can be found in exactly the same way as the initial conditions by applying Equations 3.24a-3.24i and solving for the six unknowns simultaneously.

For the second case, we considered time-dependent transport across the cell membrane, which renders the boundary conditions a function of time. For the boundary conditions at t = 0, we consider the intracellular concentrations and cell volumes to be the same as the initial conditions, and we also consider the extracellular components to instantaneously equilibrate with the bath. For this transient boundary condition, the intracellular space approaches equilibrium according to the two-parameter membrane transport model. The two-parameter model predicts the volume for individual cells, which can be related to the volume fractions of intracellular water and CPA (see Eqs. 3.9a and 3.9b):

$$\varphi_{iw} = V_{iw}\eta\varphi_s \tag{3.26a}$$

$$\varphi_{ic} = V_{ic}\eta\varphi_s \tag{3.26b}$$

With the intracellular volume fractions defined in terms of single cell volumes and the solids volume fraction, we are left with the familiar unknowns of φ_s, φ_w, φ_c, and C_{Cl} for every time point. These unknowns are solved for in a similar manner as with the initial conditions.

To advance in time, we solve for new single cell volumes after a given time step by solving Equations 3.8a and 3.8b. This results in the calculation of new single cell volumes at the boundary for each time step, enabling the full set of state variables at the tissue boundary to be updated with time as the cells change size.

For the purposes of this work, we employed the instantaneous boundary condition, as there is no appreciable difference between the results of either boundary approach for global variables. Specifically, we looked at average CPA concentration within the tissue as our convergence criterion as we will discuss later.

3.3.7 Numerical Methods

The model was written and solved in MATLAB. For temporal discretization, we employed MATLAB’s ODE 23 algorithm, an explicit variable-step Runge-Kutta method of third order accuracy. As a variable-step algorithm, ODE 23 adjusts the time step to keep the estimated error in any dependent variable within a given tolerance. We used ODE 23 as it has the potential to provide greater efficiency and stability at cruder tolerances than higher order Runge-Kutta methods [18]. As such, there is potential to reduce runtimes for simulations, which will be especially important if this model is to be applied for optimization work in CPA addition and removal protocol design. For this analysis, default tolerances were used. One drawback of ODE 23 and the MATLAB ODE suite in general is that the time differential must be written in explicit function form. Of course, we cannot write our mass concentration differential equations as an explicit function of mass concentration and time. To solve this problem, we can either implement a function stack to call upon when we interface with ODE 23, or we can implement the necessary ODE 23 source code in our own program. We opted for the latter approach, as the former could substantially increase runtime.

For spatial discretization, we used central finite differencing with even spacing between nodes. For the model, we do need to define the chemical potential gradient at the bath boundary and the flux gradient at the insulated boundary, for which we used backward differencing and forward differencing, respectively. We chose central differencing due to its ease of implementation in multi-species flow over upwind methods and its second order accuracy. In a diffusion-dominant situation, central differencing is in line with the physics of the problem. We conducted a mass transfer Péclet number analysis using the following definition:

$$Pe = \frac{Lu}{D} \tag{3.27}$$

where Pe is the Péclet number, L is the characteristic length for mass transfer, u is the convective velocity, and D is the diffusion coefficient. We can write the characteristic length as $\partial\alpha h^o$, where $\partial\alpha$ is dependent on the number of nodes we break our domain in to. With the convective velocity, we note that the model formalism treats velocity as a net velocity composed of a diffusive and convective contribution. In the non-dilute mixture, convection becomes difficult to define, but we can use the net velocity as an estimate on the upper bound of convection. Each species has its individual net velocity, but the net velocity of each species is most often on the same order of magnitude at a given location. During early simulation times at the bath boundary, the net velocity is about 10^{-3} m/s to 10^{-2} m/s depending on the number of nodes employed. Past early simulation times, though, the net velocity decreases several orders of magnitude to about 10^{-6} m/s throughout the tissue. The diffusion coefficient is also difficult to define given the mixture representation of the problem, but we can use the diffusion coefficients of salt and CPA used in the model which range from 10^{-10} m^2/s to 10^{-9} m^2/s.

To obtain consistency with central differencing, we must keep the Péclet number less than two [128]. As such, at the bath boundary at early times, the smallest $\partial\alpha$ we can obtain to meet this criterion is about 2 x 10^{-5}. If we translate $\partial\alpha$ into the necessary number of nodes, we obtain 50,001 nodes, as the number of nodes is found by taking the inverse of $\partial\alpha$ and adding one as to account for nodes at both boundaries. For the entire tissue past early times, the smallest $\partial\alpha$ becomes 0.2, which translates to 6 nodes. As such, there is a wide range in the estimate of the number of nodes needed. Both the low- and high-end node estimates seem unreasonable from inspection, and we expect the number of nodes to be somewhere in between. Given that the net velocity is an upper bound estimate on convection and we expect the physical situation to be diffusion dominant, the number of nodes will be closer to the lower estimate. As will be described later, the number of nodes used in simulations is on the order of 10 to 10^2, which gives us confidence that $\partial\alpha$ is small enough to accurately describe the physics over most simulation times. For the bath boundary at early times, the $\partial\alpha$ employed allows for a stable solution to be obtained due to the large velocities encountered.

For grid convergence, we looked at the global variable of average CPA concentration within the tissue. We conducted a grid convergence study for our base simulations, which included the model presented above for both articular cartilage and pancreatic islets, as well as an acellular version of the model (model variants are discussed in detail later). In every case, we conducted a grid convergence analysis using the classic grid convergence index (GCI) presented by Roache [111,112]. We conducted three successive levels of grid refinement using a coarse, medium, and fine grid. The coarse grid was set at 26 nodes, with the medium grid at 51 nodes, and the fine grid at 101 nodes. The GCI for the fine grid was calculated as follows:

$$GCI^{fine} = 1.25 * \left(\frac{|\varepsilon|}{r^p - 1}\right) \qquad 3.28$$

where ε is the relative error between the average CPA concentration for the medium and fine grid, r is the grid refinement ratio (two in our case), and p is the observed order of the numerical scheme. Both ε and p are defined below:

$$\varepsilon = \frac{f_2 - f_1}{f_1} \qquad 3.29$$

$$p = \frac{ln\left(\frac{f_3 - f_2}{f_2 - f_1}\right)}{ln(r)} \qquad 3.30$$

where f is the average CPA concentration, with subscript 1 representing the finest grid, 2 representing the medium grid, and 3 representing the coarse grid. Given the transient nature of the problem, the GCI was calculated for every minute time point of a cartilage simulation and every 20 seconds for the islet simulation due to a difference in the time scale of mass transfer. At every time point, we also checked to make sure that we were in the asymptotic range of convergence where the following relationship should be true:

$$\frac{GCI^{coarse}}{r^{p}GCI^{fine}} \cong 1 \qquad 3.31$$

where GCI^{coarse} is found just like GCI^{fine} in Equation 3.28, but the relative error is calculated between the coarse and medium grid. All results are reported using the fine grid. We found higher GCI values at early time points, with the GCI decreasing as the simulation progressed, since the average CPA concentration is asymptotically approaching its steady-state value through time. GCI values higher than 5% were found for simulation times ≤ 5 min, with high-end values of ~30% for the cartilage simulations. No GCI values above 5% were found for the islet simulations. The use of the fine grid was deemed adequate for this study, but tighter tolerances for the average CPA concentration could be investigated for short CPA addition and removal steps. We also found that $f_1 > f_2 > f_3$ or $f_3 > f_2 > f_1$ is not always the case at very early times for the cartilage case, indicating that a finer mesh is needed for the average CPA concentration to show asymptotic approach behavior at the earliest times. Such a fine grid is computationally intensive and most likely unnecessary for future optimization work in CPA addition and removal protocol design, with the absolute value of the relative error (Eq. 3.29) being less than 3% for all times. If necessary though, the minimum number of nodes to obtain a threshold GCI of interest can be calculated according to Roache [112].

3.3.8 Tissue Specific Parameters

3.3.8.1 Articular Cartilage

The inclusion of cells within the articular cartilage model of Abazari et al [1] requires the inclusion of new parameters. We define the new parameters necessary for our augmented model in Table 3.1, as well as the original model parameters from Abazari et al [1].

Table 3.1. Parameters used in the cell-augmented cartilage model, and CPA specific parameters are for dimethyl sulfoxide (DMSO).

Parameter	**Description**	**Value**
	Parameters from Abazari et al [1]	
h^o	Cartilage thickness [m]	1e-3
C_{fc}^o	Fixed charge concentration [mol/m^3]	200
φ_s^o	Solids volume fraction	0.2
W_b	Dry weight fraction of cartilage[a]	0.227
D_{nw}	Diffusivity of salt in water [m^2/s][b]	5e-10
D_{cw}	Diffusivity of DMSO in water [m^2/s][c]	2.25e-10
K_{cs}	Permeability of DMSO in cartilage [m^4/N/s][c]	4.7e-17
K_{sw}	Permeability of water in cartilage [m^4/N/s][c]	4.98e-16
H_A	Modulus of elasticity [Pa][c]	2.4e6
	New Parameters	
ζ	Cell density of cartilage [cells/m^3]	1e14 [124]
V_{it}^o	Chondrocyte isotonic volume [m^3]	1e-15 [95]
V_b	Chondrocyte solids volume fraction	0.41 [95]
L_p	Hydraulic Conductivity [m/Pa/s] DMSO, 21 °C	2.68e-14 [136]
P_s	CPA Permeability [m/s] DMSO, 21 °C	7.88e-8 [136]
	Derived Parameters	
φ_{iw}^o	Intracellular water volume fraction $\zeta * V_{it}^o * (1 - V_b)$	0.059
η	Cell density per volume of solids [cells/m^3] ζ/φ_s^o	5e14
A_{cell}	Chondrocyte surface area [m^2] $6^{2/3} * \pi^{1/3} * V_{it}^{o\,2/3}$	4.84e-10

[a] Dry weight fraction is needed to calculate the pure component density of the solids in order to interconvert between mass concentration and volume fraction of solids.

[b] Constant effective diffusivity used by Abazari et al [1].

[c] Best-fit values as presented in Figures 7-10 of Abazari et al [1] for DMSO at 22 °C.

3.3.8.2 Pancreatic Islets

To adapt our model to pancreatic islets, we must first address the framework of the model before addressing tissue specific parameters. We start by addressing the spherical nature of islets, and a switch to spherical coordinates is the easiest way to deal with the new geometry. We again only consider one-dimensional transport but in the radial direction (r). With this change in coordinate system, the definition of state variables remains the same, as the variables are scalar field quantities. However, there are several changes that need to be made to the transport equations and the subsequent variable transform. Starting with continuity, the accumulation and generation terms do not change, but the divergence of the flux does. Taking the continuity equation for extracellular water (see Eq. 3.7a) as an example, we have:

$$\frac{\partial \rho_w}{\partial t} + \frac{1}{r^2}\frac{\partial (r^2(\rho_w u_w))}{\partial r} + \frac{\partial V_{iw}}{\partial t}\eta \varphi_s \bar{\rho}_w = 0 \qquad 3.32a$$

Expanding the flux term results in:

$$\frac{\partial \rho_w}{\partial t} + \frac{\partial (\rho_w u_w)}{\partial r} + \frac{2}{r}\rho_w u_w + \frac{\partial V_{iw}}{\partial t}\eta \varphi_s \bar{\rho}_w = 0 \qquad 3.32b$$

The flux and chemical potential gradients remain in the same form as in the cartilage case (see Eqs. 3.7a-3.7f and Eqs. 3.10a-3.10c, respectively), just with a radial dependence. The last change to the transport equations deals with a change in the stress/strain relationship. To address this, we turn back to the derivation of triphasic theory [82,118] and note that the divergence of the mixture stress is equal to zero. Following Albro et al [3] for the fluid pressure, we can write the relationship between stress and strain in a porous sphere for our case as:

$$P_{elastic} = H_A\left(\frac{2}{r}v + \frac{\partial v}{\partial r}\right) \qquad 3.33$$

where v is the radial displacement. For the purposes of this islet investigation to simplify the model, we will consider the modulus of elasticity to equal zero, thus rendering $P_{elastic}$ also equal to zero. The mechanical properties of islets are not as well studied for cartilage, and we expect a 1000-fold reduction in its modulus when compared to cartilage [100]. In cartilage simulations, we see no appreciable difference between volume predictions when the modulus is reduced 1000-fold and when the modulus is zero. Also, Benson et al [12] reports a Boyle van't Hoff relationship for islets that can be used to predict the intracellular solids volume fraction, indicating a negligible modulus. As will be discussed later, a modulus of zero also provides a better replication of the islet model of Benson et al [12].

At this point, we have moved the transport equations to a spherical geometry, and we apply a similar variable transform strategy (see Eq. 3.17) to fix the size of the spatial domain:

$$\alpha = \frac{r}{R} \tag{3.34}$$

where R is the location of the moving tissue/bath interface as before and is measured from the static center of the spherical islet ($r = 0$). To apply the transform, the temporal gradient (accumulation term) in continuity follows from the same procedure as Equation 3.19:

$$\frac{\partial \rho_i}{\partial t}_r = \frac{\partial \rho_i}{\partial t}_\alpha - \frac{\alpha}{R}\frac{dR}{dt}\frac{\partial \rho_i}{\partial \alpha} \tag{3.35}$$

The flux term follows similarly from Equation 3.18b:

$$\frac{\partial(\rho_w u_w)}{\partial r} + \frac{2}{r}\rho_w u_w = \frac{1}{R}\frac{\partial(\rho_w u_w)}{\partial \alpha} + \frac{2}{\alpha R}\rho_w u_w \tag{3.36}$$

The chemical potential gradient follows from Equation 3.18a:

$$\frac{\partial \mu_i}{\partial r} = \frac{1}{R}\frac{\partial \mu_i}{\partial \alpha} \tag{3.37}$$

To handle the Stefan condition, we again apply our previous strategy as in Equation 3.20:

$$\frac{dR}{dt} = u_s(\alpha = 1) \tag{3.38}$$

However, the switch to spherical coordinates proves more challenging for defining R, as we need to account for the differential volume element in spherical coordinates before we apply the variable transform. The analog for Equation 3.22 becomes:

$$R = \sqrt[3]{\frac{\rho_s^o {R^o}^3}{3\int \rho_s \alpha^2 \partial\alpha}} \tag{3.39}$$

Defining the physiological reference state follows from the cartilage case, as do the initial conditions when we consider $P_{elastic}$ to be equal to zero. For the boundary conditions, the bath boundary follows from the cartilage case, but the boundary condition at the center of the islet slightly changes. With the move to spherical coordinates, the insulated boundary is now the center of the islet. We still apply the no penetration boundary condition for the center of the islet due to the radial axisymmetric nature of the problem. At the center of the islet ($\alpha = 0$) we must contend with an indeterminate form in the flux though. In Equation 3.36 we note that the second term of the flux reduces to 0/0 at the center of the islet. To write this term in a determinate form at the center of the islet, we applied L'Hôpital's rule:

$$\lim_{\alpha\to 0}\frac{2}{\alpha R}\rho_w u_w = \lim_{\alpha\to 0}\frac{2\frac{\partial(\rho_w u_w)}{\partial\alpha}}{R\frac{\partial\alpha}{\partial\alpha}} = \frac{2}{R}\frac{\partial(\rho_w u_w)}{\partial\alpha} \tag{3.40}$$

With the geometry and transport equations set, we applied the model to a small hamster islet as described by Benson et al [12]. Specifically, we investigated an islet of ~82 µm exposed to a 1.5 molal DMSO solution at 22 °C, and the change in the size of this islet is reported in the second panel of Figure 3 of Benson et al [12]. As such, we performed a literature search for islet specific parameters but also fit some parameters based on the size change data of Benson et al [12]. Table 3.2 shows the parameters used in the islet model and is broken down into parameters found in the literature, subsequently derived parameters, and fitted parameters.

Table 3.2. Parameters used for the pancreatic islet model. As many parameters as possible were taken from the model of Benson et al [12], and three parameters were fit based on the islet size change data of the second panel of Figure 3 of Benson et al [12].

Parameter	Description	Value
Literature Parameters		
φ_s^o	Solids volume fraction	0.4 [12]
φ_w^o	Extracellular water volume fraction	0.2 [12]
V_{it}^o	Islet cell isotonic volume [m^3]	970e-18 [12]
V_b	Islet cell solids volume fraction	0.4 [12]
L_p	Hydraulic Conductivity [m/Pa/s][a] DMSO, 22 °C	3.28e-14 [10,12]
P_s	CPA Permeability [m/s][a] DMSO, 22 °C	1.84e-7 [10,12]
A_{cell}	Islet cell surface area [m^2]	408e-12 [12]
R^o	Islet radius [m]	82.2e-6 [12]
D_{nw}	Diffusivity of salt in water [m^2/s][b]	5.18e-10 [12]
D_{cw}	Diffusivity of DMSO in water [m^2/s][b]	5.31e-10 [12]
Derived Parameters		
φ_{iw}^o	Intracellular water volume fraction $1-\varphi_s^o-\varphi_w^o$	0.4
ζ	Cell density of islet [cells/m^3] $\varphi_{iw}^o/(V_{it}^o*(1-V_b))$	6.87e14
η	Cell density per volume of solids [cells/m^3] ζ/φ_s^o	1.72e15
W_b	Dry weight fraction of islet[c]	0.298

H_A	Modulus of elasticity [Pa]	0
Fitted Parameters		
C_{fc}^{o}	Fixed charge concentration [mol/m^3][d]	53.3
K_{cs}	Permeability of DMSO in cartilage [m^4/N/s][d]	6.45e-19
K_{sw}	Permeability of water in cartilage [m^4/N/s][d]	5.40e-17

[a] The membrane permeabilities of the two-parameter membrane transport model were fit from the three parameters of the Kedem-Katchalsky formalism that are reported by Benson et al [10]. A least squares fitting approach was employed for an islet cell exposed to 1.5 molal DMSO at 22 °C.

[b] An effective diffusivity of salt found in the literature [12] was used as done by Abazari et al [1]. The effective diffusivity of DMSO in an islet at 22 °C as presented by Benson et al [12] was used rather than fitting for the effective diffusivity. In Abazari et al [1] they fit for the diffusivity, but we tried to reduce the number of fitted parameters.

[c] The dry weight fraction of an islet is needed to calculate the pure component density of the solids in order to interconvert between mass concentration and volume fraction of solids. The dry weight fraction was calculated by using the small islet dry weight estimate of Parman [102] in conjunction with the initial islet size and water fraction of Benson et al [12].

[d] As with Abazari et al [1], the permeabilities of DMSO and water at 22 °C were kept as fitted parameters. However, we also moved the fixed charge concentration to a fitted parameter.

One of the biggest changes from our cartilage model was fitting the reference fixed charge concentration rather than using a literature value. Finding information on fixed charges outside of cartilage, or a few other tissues such as cornea [72], is challenging. The glycosaminoglycan (GAG) content of a tissue is a good proxy for the prevalence of fixed charges [132], though, and is easier to find in the literature. We initially attempted to estimate the reference fixed charge concentration by establishing a linear relationship between the fixed charge concentration and tissue GAG content [mol fixed charges/mass GAG]. By using the fixed charge concentration of Abazari et al [1] combined with average cartilage GAG content found in the literature [7,21], we established a point on the fixed charge vs. GAG content line. We then used the GAG content reported by Theocharis et al [123] for the pancreas to estimate the fixed charge concentration, resulting in a concentration estimate of 8.12 [mol/m^3]. However, allowing the fixed charge concentration to be fit allows us to better match the osmotic response of Benson et al [12]. All of the fitted parameters of Table 3.2 were found by employing a least squares approach using the coarse mesh of 26 nodes. The coarse mesh was used due to program runtime constraints. All simulation results are reported with the fine mesh of 101 nodes.

3.4 Results and Discussion

3.4.1 Model Validation

For model validation, we compared the results of our model directly with the results of the model given by Abazari et al [1]. To do so, we created an entirely separate acellular model that mirrors Abazari et al [1] in conjunction with the cell augmented model detailed above. Both our acellular model and the model incorporating cells, for the limit of cell density approaching zero, yielded the same results. The biggest difference between our model and that of Abazari et al [1] is the numerical methods. Abazari et al [1] solved the model in COMSOL and it is unknown exactly how the moving boundary was represented. We also have a different equation for calculating the fixed charge concentration when comparing to Equation 23 of Abazari et al [1]. Figure 3.2 shows a comparison between our acellular model and that of Abazari et al [1] for a 6.5 M DMSO exposure of a cartilage slab. The two main predictions of normalized fluid weight and average DMSO concentration of the cartilage from Abazari et al [1] are compared against. The normalized fluid weight tracks the change in mass of both water and DMSO upon exposure of the cartilage with DMSO and is a good proxy for overall size change. Our results are a reasonable match with Abazari et al [1] considering our modeling approaches.

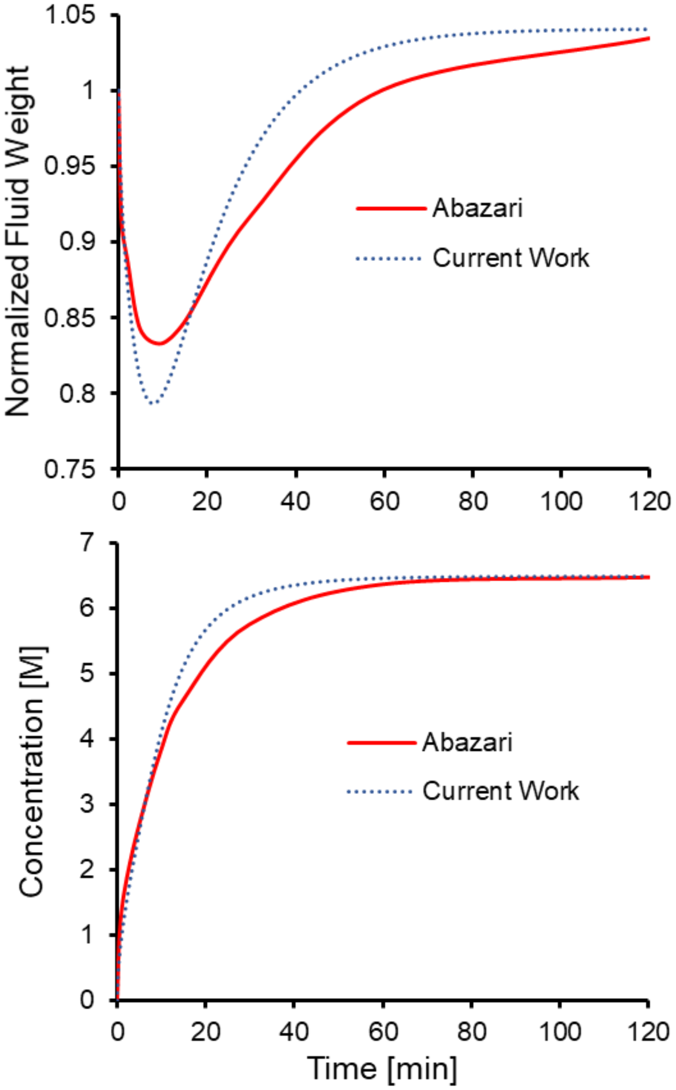

Figure 3.2. A direct comparison between our current work and that of Abazari et al [1] for a slab of cartilage exposed to a 6.5 M DMSO bath. All parameters and constants are kept the same as in Abazari et al [1] (see Table 3.1). Both panels detail overall tissue predictions as a function of time, with the bottom panel detailing the average DMSO concentration within the cartilage.

3.4.2 Parametric Analysis and the Impact of Cells

Abazari et al [1] did conduct a parametric analysis of the modified triphasic theory of articular cartilage, and the parameters investigated were their fitted parameters of D_{cw}, K_{cs}, K_{sw}, and H_A. For the design of CPA addition and removal protocols, it is necessary to understand the transient volume response of a specimen to compare against osmotic tolerance limits, as well as the CPA concentration to calculate toxicity and to know when to end a protocol [29]. The parameters of K_{cs}, K_{sw}, and H_A have little impact on CPA concentration predictions as shown by Abazari et al [1], but D_{cw} has a large impact on concentration predictions as expected, with CPA concentration predictions increasing with increasing D_{cw}. When we look at volume responses, greater tissue shrinking (as evidenced by the normalized fluid weight predictions of Abazari et al [1]) is seen with increasing D_{cw}, decreasing K_{cs}, increasing K_{sw}, and decreasing H_A. A parameter that was not investigated by Abazari et al [1] and one that we hypothesize has a large impact on predictions is that of the fixed charge concentration. In Figure 3.3, we show both the CPA concentration response and volume response for a cartilage slab (no cells) exposed to 6.5 M DMSO with varying fixed charge concentrations. We show these predictions for two different values of H_A as well, because the mechanical properties of the tissue offer resistance to an osmotic response influenced by fixed charges.

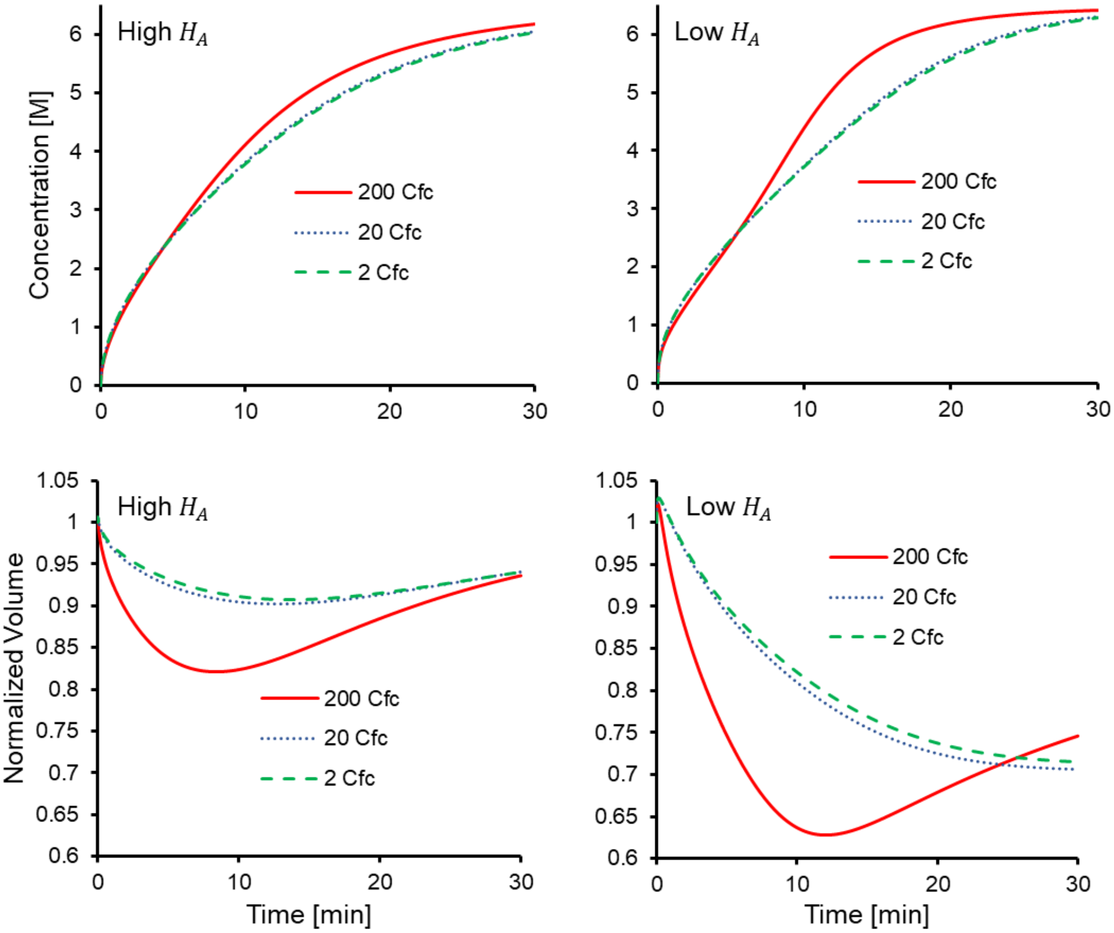

Figure 3.3. A parametric analysis on the CPA concentration and volume response of a cartilage slab exposed to a 6.5 M DMSO solution when changing both the fixed charge concentration and the modulus of elasticity. The panels with a high H_A indicate a modulus of 2.4e6 [Pa] and the panels with a low H_A indicate a modulus of 2.4e4 [Pa]. The fixed charge concentrations [mol/m^3] are also varied by orders of magnitude in each panel. Parameters are kept the same as in Abazari et al [1] (acellular case, see Table 3.1), unless otherwise noted.

As can be seen in Figure 3.3, fixed charge concentration has a small impact on the CPA concentration predictions but does have a large impact on the volume response. As the fixed charge concentration increases, so too does the osmotic pressure of the model and subsequent chemical potential gradients, driving a more pronounced osmotic response of the tissue. On the other hand, the modulus of elasticity serves as a counter to the osmotic response induced by the fixed charges. As shown by Figure 3.3, a higher modulus decreases the extent of the osmotic response (shrinking) of the tissue. Overall, there is an interplay between fixed charges and the modulus of elasticity on the osmotic response of the tissue.

Cartilage has both a high fixed charge concentration and a high modulus of elasticity, but of course, this is not the case for all tissues. For the first adaption of our model from cartilage, we are investigating pancreatic islets which have a relatively low fixed charge concentration and a low modulus of elasticity (see Table 3.2). In the bottom right panel of Figure 3.3, we see no rebound in the tissue volume for a low fixed charge concentration and a low modulus of elasticity. We do not see such a trend for islets as seen in Benson et al [12], but we expect there to be a threshold of the fixed charge concentration at which no rebound of the tissue volume is seen (at least without a time scale on a different order of magnitude). Even though islets have a relatively low fixed charge concentration when compared to cartilage, the concentration is high enough to induce a rebound in tissue volume. A tissue that does seem to show no rebound in volume is that of ovarian tissue. A prime example is the first panel of Figure 3 of Han et al [64] where they expose ovarian tissue to several different CPAs. The rebound in tissue weight (volume proxy) was on a time scale of a day when initial tissue shrinkage was on a time scale of an hour. We hypothesize that the fixed charge concentration could be behind such a phenomenon. In the limit of a very small fixed charge concentration for a non-stiff tissue, the osmotic response is only governed by the equilibration of CPA concentrations across the tissue boundary which happens relatively quickly. There is very little driving force for the tissue to rebound in volume since an unequal salt concentration across the tissue boundary is absent without fixed charges. An interesting analog at the single cell level is to consider the two-parameter model in the absence of a nonpermeating solute.

Understanding the effect that fixed charges has on volume responses in tissues is important, but we haven’t seen many parameters that have an influence on CPA concentration. The effect of cell density, though, is expected to have an impact on the CPA concentration. In Figure 3.4, we show the effect that cell density has on CPA concentration as well as the volume response for a cartilage slab exposed to 6.5 M

DMSO. Figure 3.4 provides a direct comparison between the model of Abazari et al [1] and our cell augmented model. In Abazari et al [1] they consider a cartilage slab with 20% solids, and we consider a cartilage slab with 20% solids and 5.9% cells (intracellular water) initially (see Table 3.1). We also provide a comparison using 25.9% solids and a comparison using 20% solids and 30% cells to highlight the cell effect.

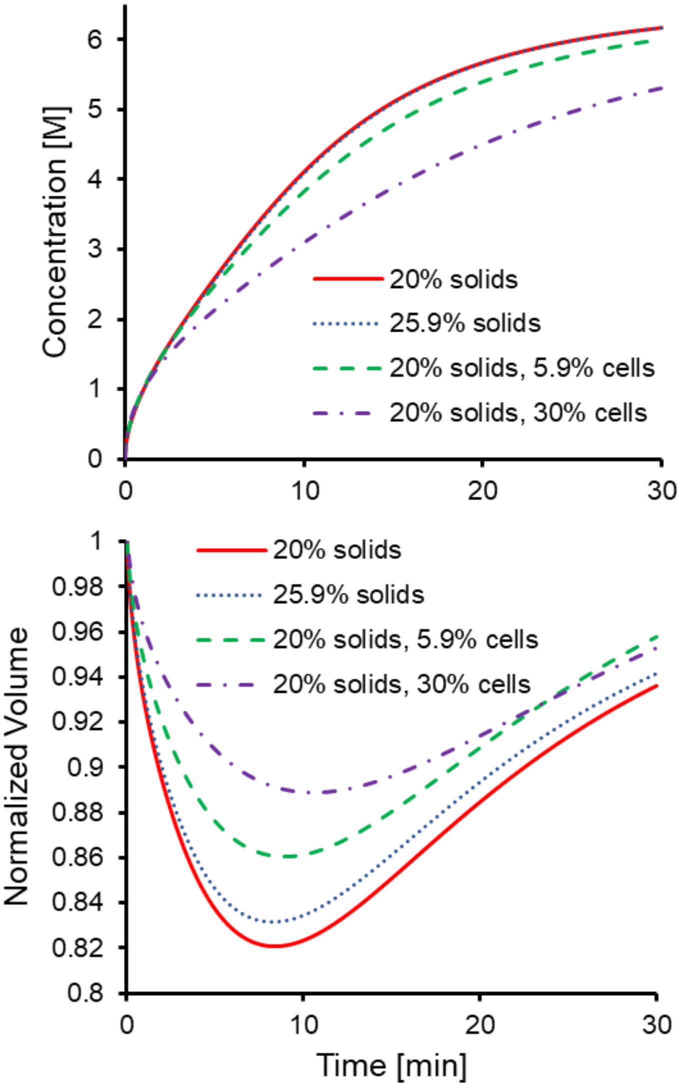

Figure 3.4. A parametric analysis on the CPA concentration and volume response of a cartilage slab exposed to a 6.5 M DMSO solution when changing the cell density. A baseline comparison is drawn between the 20% solids reported in Abazari et al [1] and our addition of 5.9% cells . We also compare a case of using 25.9% solids to isolate the cell effect and show a case of 30% cells to highlight the effect. Parameters are kept the same as in Abazari et al [1] (see Table 3.1), unless otherwise noted.

In Figure 3.4, we show that the presence of cells decreases CPA concentration predictions. In standard diffusion modeling of the extracellular space, cells pose an additional barrier to diffusion by limiting the volume fraction of extracellular space available for diffusion and also creating a more tortuous path for diffusion. As a result, the effective diffusion coefficient in the porous network is smaller when compared to the diffusion coefficient in free solution [99]. In the model formalism we have presented, this phenomenon would be accounted for in the dependence of the frictional coefficients of CPA and salt (see Eqs 3.12a-3.12b) on the void fraction of the tissue. In conjunction with adding a barrier to mass transfer in the extracellular space, cells also influence the local concentration of fluid phase species around them. By exchanging CPA with the extracellular space, cells decrease the local concentration of CPA around them and decrease the driving force for CPA transport in the extracellular space. This effect is directly isolated in Figure 3.4, as there is a more pronounced effect in CPA concentration when cells account for part of the excluded volume (20% solids, 5.9% cells) compared to only solids excluding volume (25.9% solids). Figure 3.4 also shows that cells decrease the overall osmotic response. This can be attributed, again, to both a decrease in D_{cw} and a decrease in extracellular CPA concentration which decreases a driving force of the osmotic response.

3.4.3 Model Applications – Pancreatic Islets

When surveying the effects of the many parameters of this model, it becomes clear that there are many intertwined effects that have varying impacts on predictions. In just exploring the two parameters of fixed charge concentration and cell density, we have covered the tissue-specific phenomena of fixed charges and the coupling of extracellular and cell membrane transport, and how both phenomena influence tissue size changes. Overall, using cartilage parameters and just assessing the fixed charge concentration allowed us to show an interesting osmotic response seen in the literature for ovarian tissue. As such, the application of this model to tissues in general is a real possibility. In this investigation, we will explore the pancreatic islet, which has very different parameters than cartilage but also has a much shorter length scale. Such a short length scale combined with a high cell density tests the framework of our proposed continuum-based modeling approach for tissues in general.

As shown in Table 3.2, we were able to reduce the pancreatic islet model down to three fitted parameters, with the fixed charge concentration being included as a fitted parameter due to uncertainty in its value. The parameters were fit from islet size change data reported in the second panel of Figure 3 of Benson et al [12] for an islet exposed to 1.5 molal DMSO. Figure 3.5 compares the data and model fit of Benson et al [12] to our current model reported in this work.

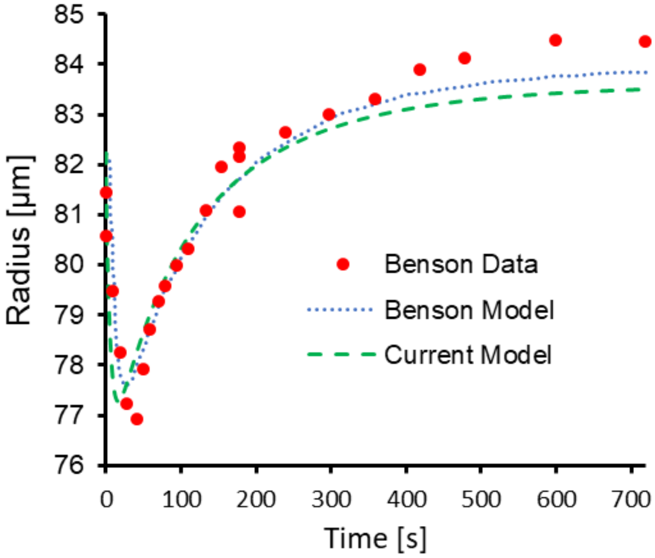

Figure 3.5. Size change data of a pancreatic islet exposed to 1.5 molal DMSO in 1x PBS as reported in the second panel of Figure 3 of Benson et al [12]. Model predictions of Benson et al [12] are also shown as well as predictions from the model described in this current work.

As shown in Figure 3.5, we were able to match islet size predictions in a comparable way to that of the model developed by Benson et al [12]. For CPA addition and removal protocol design, we want to know the volume response of the cells in conjunction with that of the tissue, as well as the CPA concentration predictions. In Figure 3.6, we show the volume response of not only the islet but of a surface cell (closest to the CPA bath) and an interior cell (farthest from the CPA bath). We also show the intracellular DMSO concentration for the surface and interior cell. Both the extracellular and intracellular concentrations are nearly identical in these simulations with the intracellular concentration slightly lagging the extracellular concentration (not shown) due to the short time scale of CPA transport across the cell membrane. Also shown in Figure 3.6 are the same predictions but for the standard 6.5 M DMSO exposure of a cartilage slab.

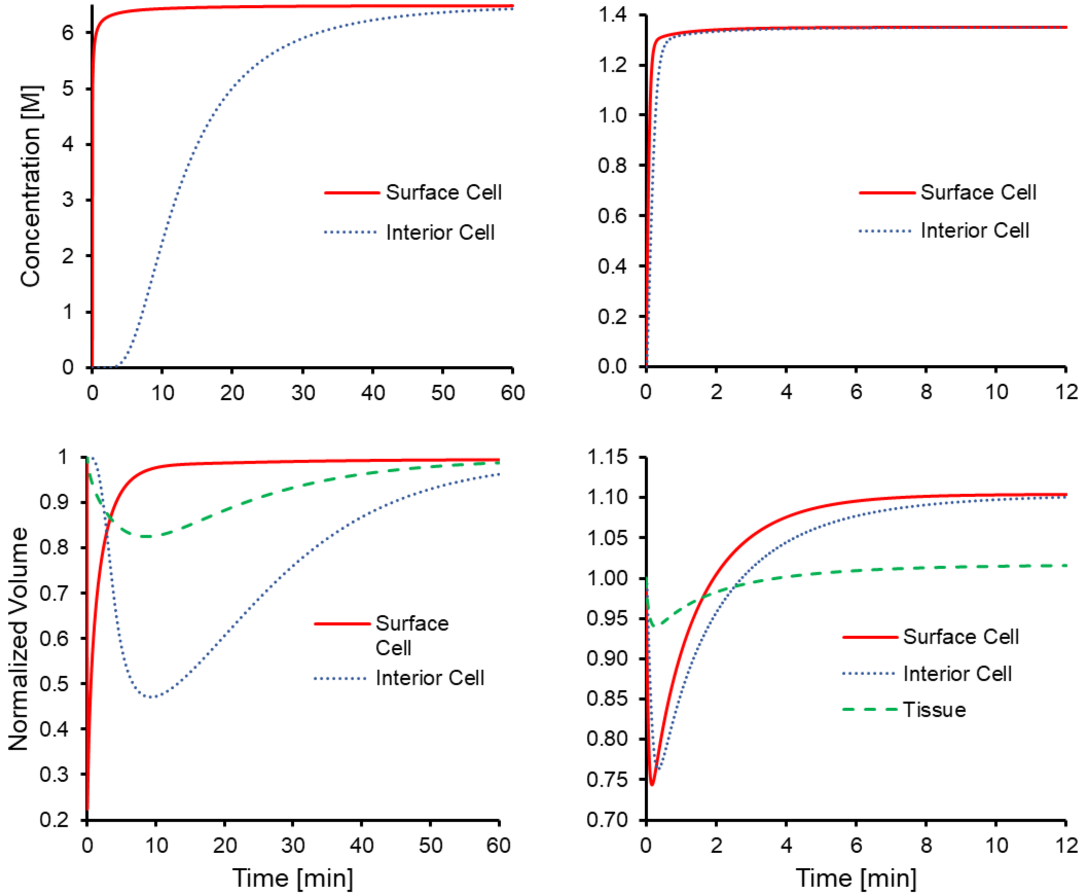

Figure 3.6. Left Panels: Intracellular DMSO concentration and volume predictions for a slab of cartilage exposed to 6.5 M DMSO (see Table 3.1 for parameters). The surface cell is closest to the exposure bath and the interior cell is furthest away. Right panels: The same predictions as in the left panels but for a pancreatic islet exposed to 1.5 molal DMSO in 1x PBS (see Table 3.2 for parameters).

The predictions for the pancreatic islet in Figure 3.6 match the predictions made in Figure 5 of Benson et al [12]. In Figure 5 of Benson et al [12], they use 1.5 molal ethylene glycol, but predictions will be very similar to DMSO since they used the same diffusion coefficient for both. When surveying Figure 3.6, one of the biggest differences between cartilage and an islet is that of the time scale of transport, which is directly related to the difference in length scale between the two specimens. There is a finite time it takes CPA to move from the surface of a tissue to the interior, resulting in a more pronounced spatial gradient in the CPA concentration across the tissue as the tissue’s characteristic length increases. Depending on the characteristic length of a tissue, this CPA gradient can greatly influence the osmotic response of cells on the surface of a tissue compared to those within the interior. The bottom panels of Figure 3.6 show that the osmotic response of a chondrocyte is a larger function of tissue position than that of a pancreatic islet cell. That being said, Abazari and colleagues [2] explored the applications of the modified triphasic theory considering initial spatial distributions of parameters—fixed charge concentration being one of them. As such, the osmotic response of a cell as a function of tissue position is also a function of potential tissue inhomogeneities, but the osmotic response of an interior cell, regardless of the magnitude of the response, will lag behind that of a surface cell due to time scale of transport across a tissue.

Setting aside tissue inhomogeneities, Figure 3.6 shows that the difference in magnitude of the osmotic response between a surface and interior cell of cartilage is more pronounced than in the islet case. The islet of Langerhans study of de Freitas et al [30] also predicts a minimal difference in the osmotic response of islet cells. This difference between tissues is again attributed to the time scale of transport across the tissue. Since CPA takes much longer to reach the interior of cartilage, the interior cells are exposed to smaller CPA concentration gradients across the cell membrane through time. The surface cell experiences a similar volume excursion to what a cell in free solution would experience with an abrupt change in CPA concentration, but the interior cell sees a slow continuous increase in CPA concentration. In the end, a shorter time scale of transport leads to less differences in cell predictions as a function of tissue position. This is a key consideration when devising a CPA addition and removal protocol for one tissue over the other, and we have shown that our continuum-based modeling approach is able to describe two vastly different tissues.

3.4.4 Implications for CPA Addition and Removal

In our results presentation, we have shown an interconnectedness of several model parameters as well as a large difference between predictions for the two different tissues investigated. As such, there are several CPA addition and removal implications that should be considered. To start, we have shown that different tissue types can have very different time scales of transport stemming from different characteristic length scales. For islets, CPA concentration equilibration occurs on the order of ∼1 min, while cartilage is on the order of ∼1 h. The osmotic response is also comparable, with islets being on the order of ∼10 min and cartilage being on the order of ∼1 h. We have also discussed a much longer response of ovarian tissue with a response being on the order of ∼1 day. Such a difference in time scale draws attention to CPA exposure times. A cartilage slab will have to be exposed to CPA for a longer amount of time than a pancreatic islet for entire tissue equilibration to occur. This leads down the path of minimizing exposure time in order to minimize toxicity. However, we have shown that minimizing exposure time for CPA equilibration does not always render the least toxic approach [13]. In contrast, for example, Shardt et al [119] proposes a cartilage vitrification protocol by minimizing exposure time. When considering any specimen, especially a tissue such as cartilage with a large time scale of transport, the time difference between the least toxic equilibration protocol and the protocol that minimizes exposure time could be vast. In our previous work looking at the three different tissue types of skin, fibroid, and myometrium [13], we showed that the least toxic protocol can be almost twice as long as the protocol that minimizes exposure time.

Moving on from CPA concentration predictions, the osmotic response of the cells and perhaps the tissue are important to consider when comparing against osmotic tolerance limits—the volume range a cell can move though before mechanical damage is induced [29,59,98]. The same principal could apply for the tissue itself and the strain of the model provides a metric for potential mechanical damage. A strategy to prevent osmotic damage of cells is to slowly add or remove CPA [29,38,59,86,98], but the idea is harder to extend to tissues due to transport complexities introduced by the extracellular space. As we have discussed in this work, cells at the surface of the tissue will experience a greater osmotic response when compared to interior cells. As such, and also considering that surface cells will experience greater toxicity from prolonged CPA exposure [13,76,119], surface cells can be a constraint in CPA addition and removal protocol design.

Both CPA concentration and osmotic responses are inherently linked. The presence of CPA can induce an osmotic response and the osmotic response can influence the CPA concentration due to a change in volume. Since the osmotic response can influence CPA concentration, it can also influence toxicity. In a previous work [29], we were able to leverage the osmotic response of endothelial cells to reduce toxicity. Specifically, we were able to leverage the swelling induced by loading cells with CPA in hypotonic buffer, which is in contrast with conventional protocols that rely on loading in isotonic buffer and primarily try to avoid excessive cell shrinkage. By manipulating the buffer tonicity, we were able to influence CPA loading kinetics and were able to load more CPA in a shorter amount of time, resulting in a low toxicity novel protocol. The same strategy is hypothesized to extend to tissues. The overall process is more complicated due to extracellular mass transfer, but the presence of fixed charges will influence both transient and equilibrium volume predictions for the tissue (and cells inside). A good way to visualize the phenomenon is to consider Boyle van’t Hoff plots for both cartilage and an islet. In Figure 3.7, we show Boyle van’t Hoff plots for both cartilage and an islet based on predictions of the model presented in this work, as well as data for both tissues found in the literature.

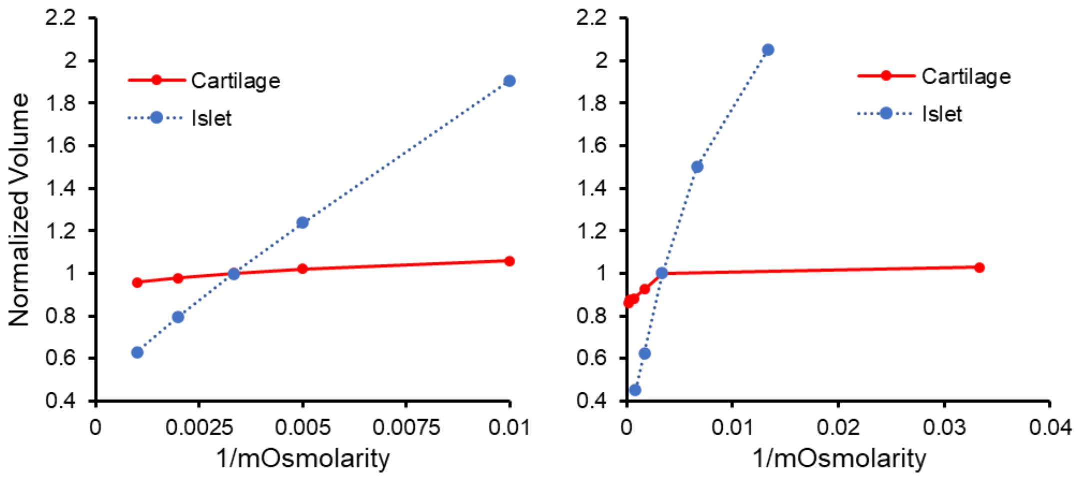

Figure 3.7. Left panel: A Boyle van't Hoff plot for both cartilage and an islet using the model presented in this work (see Tables 3.1 and 3.2 for model parameters). The five concentrations of salt in the bathing solution are 100, 200, 300, 500, and 1000 mOsmolar. Right panel: A Boyle van't Hoff plot for both cartilage and an islet from data presented in the literature. The bovine articular cartilage data is presented as strain by Lai et al [82] and has subsequently been converted to volume. The concentrations of NaCl in the bathing solution are 30, 300, 600, 1500, 3000, and 5000 mOsmolar. For the human pancreatic islet, normalized volume data is presented in Woods et al [133]. The concentrations of NaCl in the bath solution are 75, 150, 300, 600, and 1200 mOsmolar.

As Figure 3.7 shows, islets show a Boyle van't Hoff relationship [101] that can be used to predict the solids volume fraction (infinite salt concentration) while cartilage does not. This can be attributed to differing mechanical properties of the tissue and has been captured in the model with the modulus of elasticity. As such, manipulating the buffer tonicity for an islet CPA addition and removal protocol would be expected to have a greater impact on toxicity reduction when compared to cartilage. It is worthy to note that the tensile and compression moduli are different for cartilage, with the tensile modulus being about one order of magnitude greater than the compression modulus [6,97], which explains the right panel of Figure 3.7. As the modulus is kept as a constant for compression and tensile deformations in this work, it might be necessary to account for the two different moduli in the limit of leveraging very hypotonic buffers. Nevertheless, we have shown that the same model framework used in this work can describe the widely varying size change phenomenon of different tissues.

3.5 Conclusions and Future Directions

In this work, we sought to develop a general model for mass transfer in tissues. The current state of tissue mass transfer modeling within cryobiology is lacking, since each modeling approach captures some tissue-based phenomena but not all. In order to find the least toxic CPA addition and removal protocol for tissues, we postulate that a mass transfer model needs to account for all phenomena. We have established these phenomena as non-dilute mass transfer in the extracellular space, coupling between extracellular and cell membrane mass transfer, fixed charges, and tissue volume changes [132]. To incorporate all of these phenomena in one model, we turned to the modified triphasic theory of articular cartilage as presented by Abazari et al [1], with the only lacking phenomenon being that of coupled mass transfer between the extracellular space and the cell membrane. To address this lack of such a representation, we incorporated the classic two-parameter membrane transport model into the overall model formalism. With such a formalism, we were able to address all of the tissue-based phenomena in one model and parameters could then be changed to represent any tissue of interest. To test the applicability of this general formalism, we investigated a very different tissue than cartilage—pancreatic islets.

In the process of model development, we showed that we can similarly match the predictions of Abazari et al [1], and we conducted a parametric analysis of the fixed charge concentration as well as the cell density. As the fixed charge concentration increases, so too does the magnitude of the osmotic response of the tissue, but the mechanical properties of the tissue serves as a countering effect to the osmotic response. Such an inherent coupling of two parameters on one tissue response shows the interconnectedness of the many parameters of the model described, leading to the interconnectedness of the tissue-based phenomena—fixed charges and tissue size changes in this case. Cell density influenced both CPA concentration predictions and the osmotic response, with increasing cell density leading to lower CPA concentration and osmotic response predictions. The cell density also shows an interconnectedness of the tissue-based phenomena—extracellular mass transfer, the coupling of extracellular and cell membrane transfer, and tissue size changes. We can then take this a step further and consider that tissue size changes will affect the concentration of fixed charges due to a change in volume. Altogether, if any tissue is to be accurately represented by one model, that model needs to account for all phenomena. As such, we were able to show that the cell-augmented cartilage model presented in this work can be extended to pancreatic islets and we were able to match islet predictions found in the literature. Overall, we have shown a generality of our proposed model which can be applied to two very different tissues in cartilage and pancreatic islets, with a distinct possibility of extending the approach to more tissues.

With our general model, we can assess its applicability to other tissues with size change and/or CPA concentration data found in the literature such as decellularized heart valve [127] and the high cell density of ovarian tissue discussed earlier [64]. In the end, though, we want to use this model within our toxicity cost function approach [11,28,29]. Specifically, we proposed a way to scale our toxicity cost function to the tissue level but used a conventional mass transfer model built upon the framework of Fick’s second law, which only covers the tissue phenomenon of extracellular mass transfer [13]. In the future, we can use the model proposed in this work to develop less toxic CPA addition and removal protocols by accounting for more phenomena that affect the CPA concentration and osmotic response of both the tissue and the cells embedded within it. We will also consider the application of such a model formalism at the organ level by pairing the tissue-based model proposed in this work with a vasculature representation for perfusions. To do so, and to more accurately account for high cell density tissues, we will revisit our modes of mass transfer. In its current formalism at the upscaled level, our model accounts for mass transfer across a cell membrane only in each control volume individually. In reality, cells on the border of a control volume can exchange fluid with the extracellular space of a neighboring control volume and cells can exchange fluid with one another. Accounting for these modes of transport will further the generality of our model and its applications. Overall, we have presented a general model for mass transfer within tissues of varying cell density that can be added to and be used for the design of less toxic CPA addition and removal protocols.

3.6 Conflicts of Interest

The authors have no conflicts of interest.

3.7 Acknowledgements

This work was partially supported from funding from the National Institutes of Health (R01 EB027203).

PROBING THE EFFECTIVENESS OF SINGLE CELL TOXICITY REDUCTION STRATEGIES AND SUBSEQUENT MODEL-INFORMING EXPERIMENTAL METHODS IN SLAUGHTERHOUSE PORCINE KIDNEYS

In-Preparation

4. PROBING THE EFFECTIVENESS OF SINGLE CELL TOXICITY REDUCTION STRATEGIES AND SUBSEQUENT MODEL-INFORMING EXPERIMENTAL METHODS IN SLAUGHTERHOUSE PORCINE KIDNEYS

4.1 Abstract

The successful cryopreservation of organs serves as the pinnacle achievement and hardest problem of the cryobiology field. A promising solution to the problem is vitrification. However, the toxicity associated with the high concentration of cryoprotectants (CPAs) needed to vitrify has proven to be the technique's greatest challenge. In previous works, our group has proposed a mathematical optimization strategy to minimize the toxicity of single cell CPA equilibration protocols. This strategy involves the minimization of a toxicity cost function, and we have recently expanded its applicability to tissues. In this work, we investigated some experimental techniques that can be used to expand the applicability of the toxicity cost function to organs. To start, we probed the effectiveness of loading CPA in a hypotonic buffer during slaughterhouse porcine kidney perfusion, as hypotonic loading reduced toxicity for single cells in our previous work. To evaluate hypotonic loading, we leveraged several experimental techniques including taking mass and effluent flowrate change data, evaluating CPA distributions within the kidney using computed tomography (CT), and evaluating osmotic damage using a lactate dehydrogenase (LDH) assay. Our mass data indicated promising CPA loading results and was comparable to that of a single cell. However, effluent flowrate results indicated greater vascular resistance, and CT results indicated no discernable benefit with a hypotonic buffer, although LDH results indicated no discernable increase in cell death. Overall, loading CPA in hypotonic buffer needs further evaluation at the organ level, but we have laid an experimental foundation for informing an organ toxicity cost function.

4.2 Introduction

Cryopreservation addresses the long-term storage problem of biological specimens that have a limited shelf life ex vivo by arresting all cellular metabolic processes. Although a still wide-open research field, cryopreservation has had many successes. Some of the most reliable success in the field can be seen at the single cell level. For decades, successfully cryopreserved single cells have had immense beneficial impacts on scientific research, as well as animal breeding and human reproduction [9,34,68,92,107,110]. Moving past single cells, though, into more complex specimen regimes such as tissues and organs, cryopreservation becomes much more challenging and successful examples are much more sparse [47,48]. Despite the difficulty of the complex specimen cryopreservation problem, a reliable solution would forever change many research fields, as well as beneficially impacting public health. For example, the successful banking of complex specimens would forever change the face of regenerative and transplantation medicine, especially with the promise of a consistent supply from tissue engineering [48,61,90].

In this work, we will be investigating the organ regime, specifically focusing on the kidney. Although cryopreservation is not the only technique for organ preservation, it does promise to be the end all method if it can be successfully achieved when surveying the scope of techniques available [31]. The progression of research within organ cryopreservation can be traced back as far as the 1950’s, and the field has been looking for promising protocols ever since [47]. The work of Fahy and colleagues throughout the decades on rabbit kidneys has been the archetypical example of organ cryopreservation research progression [39-44,47-52]. From the decoupling of osmotic and toxicity damage in 1984, we see the identification of the main problem in organ cryopreservation to be toxicity [40]. In the same year, we see the postulation that vitrification, where the specimen is kept ice-free, is the most likely avenue to successful cryopreservation [41]. More recently, Fahy and colleagues reported on the long-term survival of a single rabbit kidney after vitrification [49]. However, the success has yet to be replicated, and there is more work to be done to overcome the toxicity problem associated with vitrification.

Toxicity is inherently tied to vitrification due to the high concentration of CPAs required to suppress ice formation. Mechanical (osmotic) damage is also a concern as the high concentration of CPAs can cause excessive volume excursions of the specimen and subsequent death. Osmotic damage is a simpler problem than toxicity and can be mitigated by incrementally increasing the CPA concentration to the maximum concentration desired and then incrementally removing the CPA [29,38,59,86,98]. Toxicity is a much more challenging problem and is a complex function of the CPA addition and removal process [5,46,47,75]. As such, any combination of the protocol variables of perfusion pressure, temperature, exposure time, CPA type, and CPA concentration will result in a different toxicity.

In order to find the least toxic protocol, one of two strategies can be employed. Most strategies in the field have employed an empirical approach where the researcher experimentally iterates through potential protocols, such as the work of Fahy [39-44,47-52]. From large data repositories, new protocols can be proposed and tested, and useful empirical relationships can be proposed such as the one proposed by Fahy and colleagues [46] that links the toxicity of a vitrification solution to its composition. However, this empirical relationship lacks an exposure time and temperature dependency and is therefore limited to a small region of the protocol space, as are most empirical approaches. Overall, there are too many protocol combinations to exhaustively test experimentally. As such, we have proposed a mathematical toxicity minimization strategy to theoretically test a protocol space while reducing the amount of necessary experiments.

Starting with the single cell vitrification problem, our group has sought to design minimally toxic CPA equilibration protocols [11,28,29]. This approach is rooted in CPA transport predictions based on cell membrane permeabilities. In conjunction, we have also quantified the toxicity imparted on the cells and have created a toxicity cost function that we seek to minimize during a CPA addition and removal protocol. In the application of this approach to adherent endothelial cells [29], mathematical optimization showed greater cell survival when CPA addition methods leveraged CPA in hypotonic buffer solution causing cell swelling, which is in contrast to typical CPA exposures that leverage isotonic exposure and try to avoid excessive cell shrinkage. This novel result is counterintuitive to the standard CPA addition paradigm but shows promise for mathematical modeling and optimization to showcase new modes of investigation. The hope is that such a technique can be scaled up to the organ regime.

Recently, Benson et al [13] scaled up the toxicity cost function approach to tissues, whereby the spatial dependence in a tissue was accounted for in the accumulated CPA toxicity. It was shown at the tissue level that there is a distinct difference between the toxicity imparted to a tissue that has the CPA exposure time minimized versus a tissue that has the toxicity cost function minimized, where the minimization of exposure time actually imparted more toxicity. This highlights that the quickest equilibration procedure is not always the best. Mathematical modeling at both the single cell and tissue levels has shown the most effective CPA equilibration procedures to not be the most intuitive. As such, we seek to apply such a toxicity cost function approach at the organ level.

In this work, we begin to build a foundation of experimental methods that can be used to inform an organ transport model, which would be the cornerstone of the toxicity cost function approach. To start, we assessed the impact of perfusing slaughterhouse porcine kidneys with isotonic and hypotonic buffer as well as CPA in isotonic and hypotonic buffer. We leveraged swelling at the single cell level to reduce toxicity but swelling is part of the larger phenomenon that is specimen size change. Size changes can be seen at the single cell level [29], the tissue level [1,12,64], and the organ level [16,78]. We hypothesize that size changes are important to consider when reducing toxicity at the organ level and every biological specimen for that matter. In conjunction with assessing kidney size changes, we also evaluated two other experimental methods for informing the toxicity cost function approach. The first is a CT method that we used to evaluate the distribution of dimethyl sulfoxide (Me_2SO) both spatially and temporally during a perfusion. Me_2SO is radiopaque enough to be visible on CT scans and the phenomenon has been leveraged before to track Me_2SO in organs [15,23]. Such a method will be able to provide data that can be compared against the predictions of an organ transport model. We also adapted a LDH cell death assay to evaluate osmotic damage in the kidney. Osmotic tolerance limits are a defined concept at the single cell level [29], but the idea needs to be scaled to the organ level to provide limits on acceptable volume excursions. Finally, we comment on the limitations of the slaughterhouse model and the uncertainty introduced by varying specimen quality. Overall, we have described an experimental framework that can be applied to the toxicity cost function at the organ level.

4.3 Methods and Materials

4.3.1 Solution Preparation

The base solution used in all experiments comes from Hauet et al [66] who proposed an isotonic extracellular-like hypothermic preservation solution for porcine kidneys. We adopted the solution due to its reported success [53,66] and simplicity. As the tonicity of the solution is our primary manipulation variable of interest, it is easiest to use a simple solution, and its composition can be found in Table 4.1. Given that the solution makes use of a bicarbonate buffer, solutions were prepared within a 24-hour timeframe before an experiment took place. Solutions were stored in vessels with a small head space and refrigerated until the time of the experiment, at which time they were warmed to room temperature.

Table 4.1. Composition of the isotonic extracellular-like base solution [66].

Constituent	Concentration	Vendor
NaCl	118 mmol/L	EMD Millipore, Burlington, MA VWR Chemicals BDH, Radnor, PA
KCl	5 mmol/L	EMD Millipore, Burlington, MA
$NaHCO_3$	25 mmol/L	EMD Millipore, Burlington, MA
$MgCl_2$	1.2 mmol/L	VWR Chemicals BDH, Radnor, PA
$CaCl_2$	1.75 mmol/L	Fisher Chemical, Waltham, MA
20 kDa PEG[a]	30 g/L	Alfa Aesar, Haverhill, MA Bean Town Chemical, Hudson, NH
7.3 ± 0.1 pH		
330 ± 20 mOsm		

[a] Polyethylene glycol

In each experiment, we tested two different versions of the solution listed in Table 4.1. The first is the isotonic version of the solution which was unmodified and the second is a hypotonic version. The hypotonic version only includes the buffer (bicarbonate) and oncotic agent (PEG), and the solution was measured at ∼50 mOsm on an Advanced Micro Osmometer Model 3300 (Advanced Instruments, Norwood, MA).

For our physical change data experiments where we measured kidney mass and effluent flowrate, we perfused kidneys with 10% (m/v) ethylene glycol (EG) (Macron Fine Chemicals, Radnor, PA) in either the isotonic or hypotonic versions of the buffer solution. For CT experiments, we perfused kidneys with 15% (m/v) Me_2SO (Fisher Chemical, Waltham, MA) in either buffer. Moving to LDH experiments, we added a Triton X-100 solution to the end of our perfusions. The solution was made with 10% (v/v) Triton X-100 (EMD Millipore, Burlington, MA) in isotonic buffer. For all solutions, the concentration is reported on a solvent basis (e.g. 10% by mass EG and 90% by mass water for a given volume). The volume of mixing was considered negligible for all solutions with the largest change in volume being 3%, and extra solutes (constituents of Table 4.1) were added to all solutions to counteract the dilutive effects of either CPA or Triton X-100 to obtain the concentrations in Table 4.1.

4.3.2 Kidney Acquisition

Kidneys were obtained from three different sources. Porcine kidneys were obtained from two different slaughterhouses, and we also obtained human kidneys that were transplant rejects. Table 4.2 shows the physical details of kidneys obtained from each different source. In conjunction with the different kidney sources, Table 4.2 also shows the three different experiments we conducted and where the kidneys were obtained from for each experiment.

Table 4.2. Physical details of kidneys obtained from one of three sources. The experiments conducted with each kidney source are also shown.

	Porcine Source 1[a]	**Porcine Source 2[b]**	**Human Source[c]**
Breed	Red Duroc	Unknown Mix	N/A
Sex	Female	Female	Unknown
Weight	200-250 lbs	250-350 lbs	Unknown
Age	Unknown[d]	Unknown[d]	Unknown
Physical Change Experiment	**X**	**X**[e]	**X**
Warm Ischemia Time	20 min	25-40 min	Unknown
Cold Ischemia Time	3-5 hr	2-4 hr or ~5 d	~3 d
CT Experiment		**X**	
Warm Ischemia Time		25-40 min	
Cold Ischemia Time		~18 hr	
LDH Experiment		**X**	
Warm Ischemia Time		25-40 min	
Cold Ischemia Time		3.5-5.5 hr or 19-21 hr	

[a] Porcine kidneys obtained from Stanton's Slaughter House (Albany, OR).
[b] Porcine kidneys obtained from Mohawk Valley Meats (Springfield, OR).
[c] Human kidneys obtained as transplant rejects from the Pacific Northwest Transplant Bank (Portland, OR).
[d] Ages of the pigs are not precisely known but best estimates are ~6 mo.
[e] For some physical change experiments, LDH experiments were conducted as well.

We obtained all porcine kidneys at the time of slaughter and obtained all human kidneys after rejection from the Pacific Northwest Transplant Bank, rendering little information for their warm ischemia time. For porcine source 1 in Table 4.2, we resected one kidney per animal, but for porcine source 2, we resected both kidneys per animal which led to a longer warm ischemia time. For all kidneys obtained, the initial 10-15 min of the warm ischemia time was due to the kidneys remaining in the animal during initial slaughterhouse processing. After an animal had been initially processed by the slaughterhouse, the kidney(s) were resected from the renal fascia, such that the renal capsule was not punctured, and as much of the adipose capsule was removed as possible, except in the immediate vicinity of the renal hilum. Approximately two inches of the renal artery was kept with a specimen, as measured from the renal hilum, for perfusion setup purposes. After resection, the renal artery was cannulated, and the kidney was cold-flushed with 500 mL of the isotonic extracellular-like solution of Table 4.1, and the flush represents the remainder of the warm ischemia time. Overall, our warm ischemia times are comparable to warm ischemia times reported in the literature [33,63,126]. After the cold flush, the kidneys were placed in a cooler and brought to the laboratory where they were kept at 4 ^oC until they were used for a particular experiment. For porcine source 2 kidneys with a cold ischemia time of 5 d used for the physical change experiment (see Table 4.2), we augmented the flush solution with 200 IU/mL penicillin (Alfa Aesar, Haverhill, MA). At the time of an experiment, the kidneys were removed from the 4 ^oC environment and brought to room temperature.

4.3.3 Perfusion Apparatus

A gravity-fed perfusion apparatus was fabricated to conduct all experiments. The system was designed to maintain a constant hydrostatic pressure head of 100 mmHg at the arterial inlet. This pressure is at the upper range of inlet arterial pressures listed in the literature [47,63,108,126]. We chose a higher pressure due to potential pressure drops in the perfusion system upstream of the kidney, and to overcome a higher than physiological pressure drop in the kidney due to hypothesized random coagulation patterns in the capillary beds. With our slaughterhouse model, we were not able to heparinize the animal and some clots were part of the experiment as we will discuss later. As such, most of the flow resistance was in the kidney, which decreases the pressure drop across the perfusion system.

For all experiments, there were at least two perfusates introduced to the kidney. As such, the design of a gravity-fed system incorporated dedicated solution reservoirs for each unique perfusate. The general design is to raise each solution reservoir above the arterial inlet to some height, much like that of an IV, as to obtain the pressure head of interest. The fluid level in each reservoir was maintained at a constant height by pumping in fluid to the reservoir and having a constant overflow. Each experiment required a quick change between perfusates, which required the effluent line of each dedicated reservoir to be connected. This connection was made through a series of Y joints until all effluent lines were condensed into one line, which could then be connected to the arterial cannula. Upstream of each Y joint, a check valve was placed on each effluent line. With a valve on each line, the type of perfusate could be quickly switched.

The physical change data sought for some experiments was the time dependent mass of the kidney and the effluent flowrate from the kidney. The mass of the kidney gives us an indication of the internal mass transfer as it serves as a proxy for volume, and the effluent flowrate gives us an indication of the change of vasculature geometry, namely vascular resistance. To obtain the data, a kidney platform was fabricated that rested on a scale (Ohaus, Model V11P3, Parsippany, NJ), which allowed for the time dependent mass measurement to be taken. For the effluent flowrate measurement, the top of the kidney platform consisted of a grate which the kidney rested on. The grate allowed the effluent to quickly pass through the platform from which it could be collected. Perfusate was collected every minute and its mass was measured, giving an estimate to the effluent flowrate under the assumption that its density was equal to that of water. Figure 4.1 shows a schematic of the perfusion apparatus and kidney platform. The schematic shows a two-reservoir setup, but the system can be generalized to any number of reservoirs through the inclusion of more Y joints.

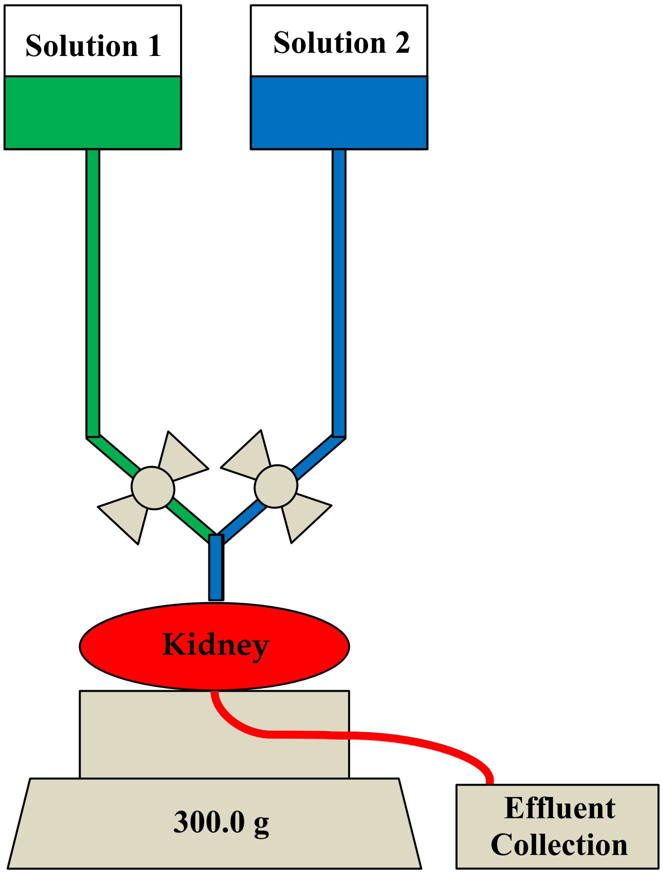

Figure 4.1. A schematic of the gravity-fed perfusion system used, including the kidney platform. In this system variant, two separate solution reservoirs can be seen, but the system can be generalized to any number of reservoirs. The system is connected to the renal artery of the kidney, and a hydrostatic pressure head of 100 mmHg is maintained. The kidney rests on a grate from which the effluent can be readily collected. The platform rests on a scale from which the mass of the kidney can be recorded.

To fully characterize the pressure drop of the perfusion system, we obtained a correlation for the pressure drop as a function of flowrate for each perfusate and system variant tested. As we have several minor losses from fluid network features such as step-down connectors and valves, we decided to simplify the calculation rather than obtain a minor loss coefficient for each feature. Given the complex flow path of the system, the pressure drop is not proportional to the flowrate (laminar) nor to the square of flowrate (turbulent). Instead, there is a middle ground between the two flow regimes, and the pressure drop can be described as a power law in flowrate with an exponent between 1 and 2. With the pressure drop correlation and using the effluent flowrate and kidney mass change to find the influent flowrate, the inlet arterial pressure was calculated using Bernoulli's equation. For all kidneys, excluding the Triton X-100 perfusion times, the lowest pressure calculated was about 60 mmHg. Looking at just the Triton X-100 perfusion times, we did have some instances where the pressure dipped to about 40 mmHg. For Triton X-100, we found a linear correlation between pressure drop and flowrate.

4.3.4 Physical Change Experiment

Given the success of the optimization strategy presented in Davidson et al [29] at the single cell level, we wanted to explore applicability of the strategy to the organ regime. Specifically, we wanted to see if the use of hypotonic buffer for CPA loading led to reduced toxicity. To do so, we compared a one-step loading procedure of 10% (m/v) EG in either isotonic or hypotonic buffer and measured the kidney mass and effluent flowrate throughout the entire experiment. The kidney's mass was measured every 30 seconds and the effluent flowrate was approximated by taking the mass of the volume of effluent collected every minute. Such an experimental setup also provides data that can help to inform a future organ mass transport model for the toxicity cost function approach.

Before EG was introduced to the kidney, the kidney was first equilibrated on a mass basis with isotonic buffer. Although the buffer is isotonic, there is still some swelling imparted, as the buffer is hypotonic in regards to a global kidney tonicity—some areas of the kidney are quite hypertonic due to the kidney's physiology. Equilibrating the kidney on a mass basis established a consistent reference point at which CPA could be introduced. The metric used to switch to a CPA solution was the appearance of the asymptotic approach of the kidney mass to some steady state value. Specifically, we looked for three consecutive mass values to be equal (or one value to be only slightly different) before a switch was made. The time scale for such a steady state approach was found to vary among the kidneys of porcine source 1 (see Table 4.2), varying from 12 to 27 min. As a result, for all other physical change experiments, we used a 30 min equilibration period. During the equilibration period, the isotonic buffer was recycled, where the kidney effluent was placed back in the isotonic buffer reservoir of the perfusion system as to reduce the amount of solution needed. For all isotonic equilibration periods, 2 L of solution was used and recycled.

At the time of the solution switch, the EG valve was opened and then the isotonic buffer valve was closed, as to maintain the pressure head throughout the transition period of less than 5 s. Unlike the isotonic buffer perfusion, we ran the EG perfusion until we captured the classic shrink-swell phenomenon when a specimen is introduced to CPA. It was found that a time frame of 10 min captured the EG loading kinetics of interest for the kidneys of porcine source 1 (see Table 4.2), and the 10 min time frame was used for all other physical change experiments. Unlike the experiments using kidneys from porcine source 1, both kidneys from the same animal were used for experiments using porcine source 2.

4.3.5 CT Experiment

To assess the CPA distribution within the kidney to inform a future organ mass transport model and to address CPA distribution concerns raised from an increase in vascular resistance due to the use of hypotonic buffer (as will be described later), we turned to medical imaging in the form of CT. To do so, we adopted a CT method from the literature found in the work of Corral et al [23]. In their paper they show a linear relationship between X-ray attenuation and Me_2SO concentration. In one experiment, they submerge rabbit kidneys in varying concentrations of Me_2SO and watch the kidney's equilibration with the solution over the timescale of days. For our purposes, we are interested in the shorter time scales of perfusion.

To achieve a CT perfusion, we turned to the radiology department in the College of Veterinary Medicine at Oregon State University. They have an Aquilion 64 CT scanner (Toshiba, Tokyo, JP) and the voltage of the scanner was lowered as much as possible as suggested by Corral et al [23], and a final value of 100 kV was used compared to 75 kV in Corral et al [23]. The voltage could not be lowered any more due to field of view constraints. The use of a lower voltage has also been reported in the work of Bleisinger et al [15]. The current used was 200 mA with a scan time of 0.5 s and an image analysis spatial resolution of 2 mm.

As with Corral et al [23], we established a linear trend between X-ray attenuation and Me_2SO concentration through the development of a standard curve. We tested varying concentrations of Me_2SO in three different solutions: water, isotonic buffer, and hypotonic buffer. The linear range extended to about a 25% (m/v) Me_2SO solution for our particular setup. To make the measurements for the standard curve, 2 mL of each solution was placed in a well of a 24-well plate. We varied the concentration of Me_2SO by 5% in each well, with one well plate being dedicated to each background solution. In total, we imaged 9 different well plates for the 3 different solutions tested in triplicate at the varying Me_2SO concentrations. To make the standard curve, we measured the average grayscale value of the top cross-section of each well from the obtained CT images. Before the images were taken, each well plate was well mixed.

For the perfusion experiment, we used our base perfusion methodology as in our physical change experiment, where we equilibrated the kidney for 30 min with isotonic buffer and recycled the buffer as before. However, the CPA we switched to was 15% (m/v) Me_2SO in either isotonic or hypotonic buffer. We increased the concentration of the CPA over the physical change experiment to 15% (m/v) after looking over the range of attenuation of our standard curve. We did not want to obtain maximum attenuation with a high concentration of Me_2SO in addition to background tissue attenuation. However, we also wanted to obtain the largest range of attenuation between background tissue and maximum Me_2SO concentration in that tissue, while still staying in the range of a realistic concentration used for a first step of CPA addition.

The perfusion itself was slightly different than the physical change experiment in that two kidneys were perfused in parallel in the CT scanner. Two of the three CT experiments conducted used both kidneys from the same animal, where one kidney received an isotonic Me_2SO perfusion and the other kidney received a hypotonic Me_2SO perfusion. In the third experiment, kidneys from different animals were used due to acquisition constraints. For all experiments, one left kidney and one right kidney was used, with the isotonic and hypotonic treatments being randomly assigned to the right or left kidney for each experiment. With a parallel perfusion setup, both kidneys were captured in the CT field of view for each scan conducted and were at the same time point of their respective perfusions. For two of the CT experiments, we perfused the kidneys for 20 min with Me_2SO (slightly longer than the time scale identified in the physical change experiment), but for the third CT experiment, we perfused the kidneys for 60 min with Me_2SO in the hope of capturing steady-state within the kidneys. The time points imaged were: 0 min (initial scan), 30 min (scan after isotonic equilibration), 31 min, 32 min, 33 min, 34 min, 35 min, 40 min, 45 min, 50 min, 60 min (for one experiment), and 90 min (for one experiment).

For image analysis, we broke the kidney down into two coarse spatial regions designated as the cortex and medulla. The medulla has been difficult to reach with CPA as discussed by Fahy [47,49]. As such, as a first pass analysis, we wanted to investigate a coarse designation between the more easily reached cortex versus the medulla. At every time point and for each kidney, we manually segmented the cortical and medullary regions. All image analysis was conducted using MATLAB, and we limited our analysis to only the coronal plane of the kidney—the simplest plane to determine the boundaries of the cortex, medulla, and pelvis by inspection. For each kidney, the three middle image slices were analyzed and averaged. The use of three slices creates a larger sample size of both the cortex and medulla. In a coronal plane analysis, the designation between cortex and medulla for far anterior and far posterior slices is not as apparent.

As a first step in image analysis, the boundaries of each kidney were found using appropriate thresholding beforehand to remove any periphery adipose tissue (low attenuation) in the image and to separate both kidneys into separate objects. Another round of thresholding was also used to remove any air bubbles (zero attenuation) in the kidney. Once a kidney had been isolated, the void space of the pelvis was manually segmented out, and then the cortex and medulla were manually segmented. The void space of the pelvis is easily segmented out by inspection due to its low attenuation. However, the border between the cortex and medulla is more difficult to visualize. As a uniform approach to manual segmentation, the final time point image for each kidney was visualized at the time of segmentation. Given that the medulla is harder to be reached with CPA, we can observe this with a contrast agent (Me_2SO) at longer perfusion times. The edge of the renal pyramids with the cortex starts to become distinct as they have a lower attenuation than the neighboring cortex. Using the last time point image for each kidney, we can estimate the medulla/cortex border of earlier time points. Figure 4.2 shows a typical segmentation of a kidney in the coronal plane.

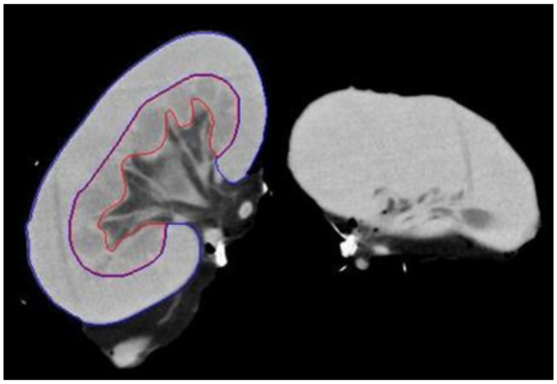

Figure 4.2. A standard image collected with the borders of both the cortex and medulla superimposed on the image after segmentation for the left kidney in the image. The red border indicates the medullary region, and the blue border indicates the cortical region.

For one kidney analyzed, specifically the right kidney of Figure 4.2, the alignment of the kidney was such that we did not obtain a clear coronal plane. Instead we obtained a slight rotation out of the coronal plane about a sagittal line, resulting in an oblique plane. However, the same segmenting technique was still able to be used. The only difference was that the pelvis was not segmented out as it was difficult to determine its border and was deemed negligible to the slices analyzed. Figure 4.3 shows a standard segmentation of a kidney in an oblique plane. On that kidney, there was also a lower attenuating abnormality in the cortical region, which was segmented out.

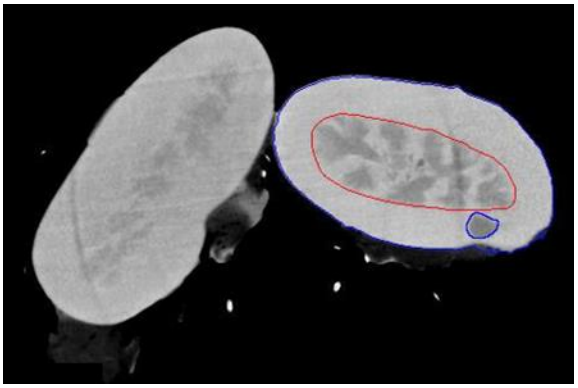

Figure 4.3. A standard image collected with segmentation of a kidney in an oblique plane. Within the red medullary border, it can be seen that there is perhaps some pelvis within the plane at the very center of the image, but this region was deemed insignificant to the analysis. The darker region in the blue cortical border was identified as an abnormality and was segmented out according to the smaller blue border.

Once all images were segmented, the grayscale value of every pixel in a given spatial region for a time point could be averaged, giving a spatial and temporal distribution of X-ray attenuation. By using the standard curve generated, we converted attenuation values to Me_2SO concentration. However, the solids content of each spatial region needs to be known in order to use a fluid phase standard curve. Equation 4.1 shows the individual contributions to the total attenuation in grayscale of a given voxel, assuming additive contributions from each component:

$$Total\ Attenuation = x_s \varepsilon_s c_s + (1 - x_s)\varepsilon_{Me_2SO} c_{Me_2SO} + (1 - x_s)\varepsilon_{fb} c_{fb} \qquad 4.1$$

where x is the volume fraction, ε is the mass attenuation coefficient, c is the mass concentration, subscript s represents the solids, and subscript fb represents the fluid background. The attenuation coefficient of Me_2SO can be found through the standard curve made when the fluid background attenuation is subtracted off at a Me_2SO concentration of zero. For a given kidney voxel attenuation measurement, the volume fraction of solids is unknown. Of course, the solids will be a function of space as well as evolve throughout a given treatment. For the analysis, we assumed those variations to be negligible, thus assuming a constant average volume fraction of solids in the medulla and cortex. To prime the analysis, we used a value of 15% solids in the medullary region as an estimate based on the range reported in Gardner and Vierling [60] for the papillary region of the rat kidney on a volume basis. This value is reasonable when considering the solids mass fraction estimates in the medulla of Bulger [19] (10% at the inner and outer medullary border of the rat medulla) and Levitin et al [89] (~15% for the dog medulla). Also, this value is reasonable considering the solids mass fraction estimate of an entire porcine kidney from Blum et al [17] (13%-19%), and the estimates of entire rat, rabbit, and human kidneys (19%-29%) [54,88,109]. From this 15% medullary value, we can then estimate the solids content of the cortex based on the difference in background attenuation before Me_2SO addition. Specifically, the ratio of background attenuation of the cortex to the medulla is equal to the ratio of the solids volume fraction of the cortex to the medulla, and we find a value of 15.5% for this particular analysis. The mass attenuation coefficient of the solids is a constant as well as the mass concentration of solids, since in this context the mass concentration of solids is estimated as the pure component density. In the end, based on background attenuation before Me_2SO addition, the fluid phase standard curve, and an estimate of solids from the literature, we can estimate the concentration of Me_2SO in the fluid phase as a function of space and time.

4.3.6 LDH Experiment

To establish osmotic tolerance limits for use in an organ level toxicity cost function and to characterize osmotic damage induced by the hypotonic buffer, we turned to assaying the kidney’s effluent during perfusion. Osmotic damage in an organ is a multifaceted concept that is not well defined. In our mathematical framework, we would like to describe it as the combination of mechanical damage at both the cell and tissue level. To start, we sought to address the osmotic damage incurred by cells. To do so, we augmented our established base perfusion methodology. We still equilibrated kidneys with isotonic buffer for the first 30 min before switching solutions. However, we did not switch to a CPA solution. Instead, the solution was switched to either hypotonic or isotonic buffer for 10 min. Switching to pure hypotonic buffer without a permeating CPA provides an upper limit on the osmotic damage that can be incurred. The switch to an isotonic buffer provided a baseline control as with switching to CPA in isotonic buffer in previous experiments. As with our CT experiment, we conducted an isotonic and hypotonic experiment by using both kidneys from the same animal. One side note of the LDH experiment is that we conducted an LDH analysis for the physical change experiments of porcine source 2 as well (see Table 4.2). These experiments gave insight into osmotic damage but also tested the assay for potential to be used as a cytotoxicity assay as will be described later.

To estimate the cellular osmotic damage, we introduced another perfusate switch after the pure buffer perfusion period. In both perfusion experiments, we introduced 10% (v/v) Triton X-100 (positive control for cell death) in isotonic buffer for 10 min. The switch to Triton X-100 acted as an internal control for each kidney, where any remaining viable cells after buffer treatment were lysed, at least viable cells that could be affected by a perfusate on our time scale of interest. A relatively high Triton X-100 concentration was used above standard concentrations in LDH protocols as to maximize the driving force for Triton X-100 transport into the interstitium in the hope that the Triton X-100 would reach the same interstitial space as with a CPA within the time scale of interest. We conducted endothelial cell experiments that showed the same amount of LDH was released from single cell cultures when exposed from 1% (v/v) Triton X-100 to 10% (v/v) Triton X-100 (data not shown). To assess osmotic damage, the effluent was collected from each perfusion period and assayed for LDH content (BioAssay Systems, Catalog No. D2DH-100, Hayward, CA). It is hypothesized that the sum of all LDH released throughout an experiment equals the total LDH that can be released during a perfusion on the time scale of about 10 min. As such, cell death can then be estimated by the LDH released during the pure buffer perfusion. The cell death estimate is calculated by dividing the LDH released during the pure buffer perfusion by the total LDH released in the experiment.

For the hypotonic perfusion, one slight change was made. As the swelling from the hypotonic buffer reduces flowrate, we hypothesized that some LDH might still be trapped in the kidney after the hypotonic perfusion period. As such, we added a 5 min isotonic perfusion period after the 10 min hypotonic perfusion period to increase the flowrate and allow us to capture any trapped LDH from the hypotonic perfusion and not underestimate the damage incurred by the hypotonic treatment. The switch also showcases the ability to recover flowrate after hypotonic treatment as will be described later. Figure 4.4 shows a schematic of the timeline of each experiment.

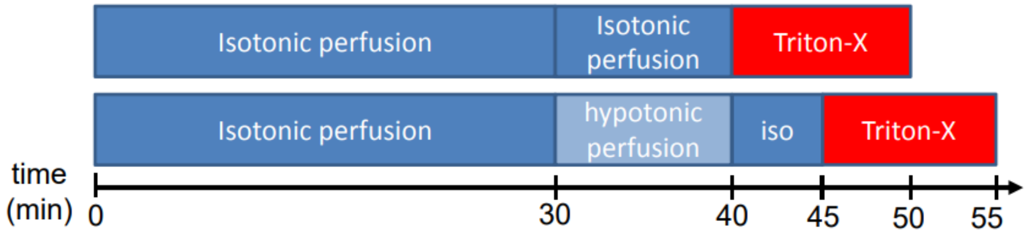

Figure 4.4. A schematic detailing the timing of each experiment. The top bar represents the timing of the isotonic buffer perfusion, and the bottom bar represents the timing of the hypotonic buffer perfusion. There is an additional isotonic perfusion period after the hypotonic perfusion period to allow the flowrate to recover and for any trapped LDH to be recovered.

4.4 Results and Discussion

4.4.1 Kidney Physical Change Data

4.4.1.1 Mass Change

One of the two main physical change variables that we measured during perfusion was the change in mass of a kidney. The change in mass is a good proxy for the change in volume of the kidney and is an easier experimental measurement to make. Upon addition of CPA to the kidney, we expect a transient decrease in mass, much like the classic osmotic response of a single cell [16,78]. In Figure 4.5, we show the mass change data for all four groups of kidneys perfused with 10% (m/v) EG in both isotonic and hypotonic buffer.

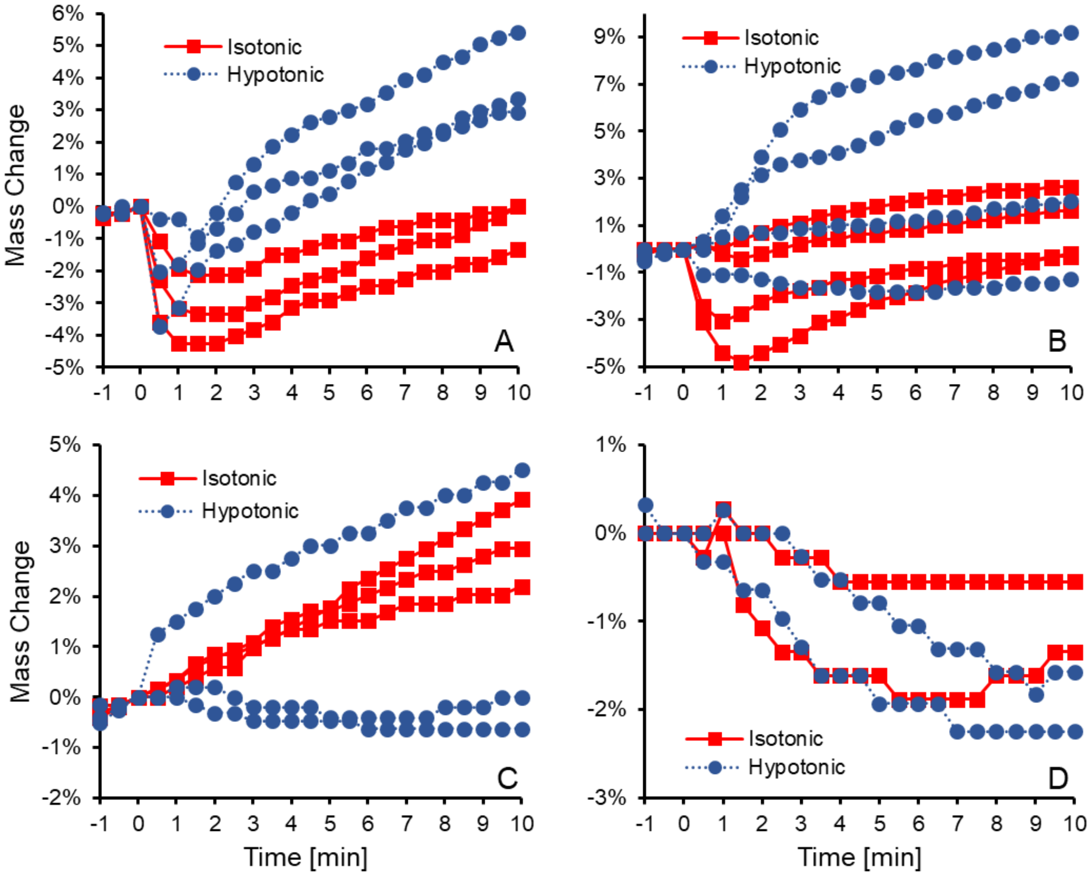

Figure 4.5. The normalized mass change of the four different kidney groups perfused with 10% (m/v) EG. Each group was perfused with EG in both isotonic and hypotonic buffer. All kidneys were equilibrated on a mass basis with the isotonic buffer for 30 min, and EG addition is represented by time = 0 min. The four different kidney groups are as follows: Panel A – porcine kidneys with an approximate warm ischemia time of 20 min and a cold ischemia time of 3-5 hr (n = 3 for each tonicity); Panel B – porcine kidneys with a warm ischemia time of 25-40 min and a cold ischemia time of 2-4 hr (n = 4 for each tonicity); Panel C – porcine kidneys with a warm ischemia time of 25-40 min and a cold ischemia time of 5 d (n = 3 for each tonicity); Panel D – human kidneys with an unknown warm ischemia time and a cold ischemia time of 3 d (n = 2 for each tonicity).

From Figure 4.5, we notice that the tonicity impact on the mass change is not consistent across kidney groups. We hypothesize that ischemia time influences the osmotic response of the kidney. In Panel A, we note a remarkably similar osmotic response of the kidney to that of the single cell. We see a mass decrease with both tonicities and a faster mass recovery with the hypotonic case in conjunction with swelling. This indicates that a hypotonic buffer could be leveraged to load more CPA in a shorter amount of time. However, this discernable trend becomes muddled as we move to Panel B.

In Panel B, we note some similar osmotic trends as with Panel A. Some isotonic replicates of Panel B show the same osmotic response as with Panel A, and some hypotonic replicates show greater swelling than their isotonic counterparts. However, some replicates show unexpected osmotic responses and do not deviate much in mass throughput the perfusion. For Panel B, we hypothesize that we are within a transition zone of warm ischemia time in regards to obtaining a kidney that shows expected osmotic behavior versus one that does not. As we move to Panels C and D, we note no real distinctive impact of the tonicity of a treatment. Again, we hypothesize that the ischemia time is a key contributor to this, as we note that Panels C and D have a much longer cold ischemia time than the normal transplantation window [33]. Overall, the results from Panel A are promising when considering the effectiveness of loading a kidney with CPA in a hypotonic buffer. The effectiveness of hypotonic loading though does seem to be dependent on the quality of the specimen, and later on we will comment on the precision of using a slaughterhouse model.

4.4.1.2 Volumetric Flowrate

The second physical change variable that we measured during perfusion was effluent flowrate from the kidney. This effluent flowrate is the sum of flowrates from both the renal vein and ureter. By measuring the flowrate as a function of time during the perfusion, we begin to understand the change in flow path geometry. As flowrate decreases, flow resistance in the kidney increases. If resistance is increasing, we can infer that the diameter of the capillaries in the kidney is most likely decreasing. In Figure 4.6, the effluent flowrate change data is shown for all four groups of kidneys perfused with 10% (m/v) EG in both isotonic and hypotonic buffer.

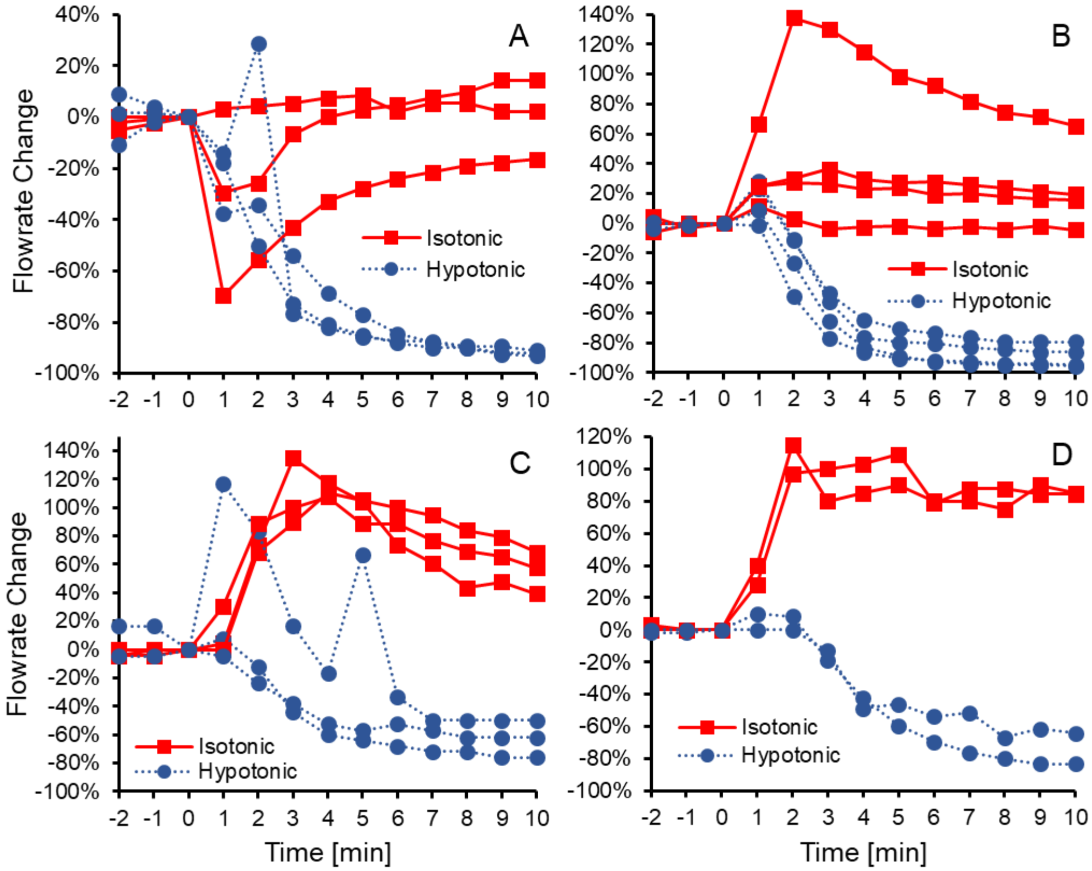

Figure 4.6. The normalized effluent flowrate change of the four different kidney groups perfused with 10% (m/v) EG. Each group was perfused with EG in both isotonic and hypotonic buffer. All kidneys were equilibrated on a mass basis with the isotonic buffer for 30 min, and EG addition is represented by time = 0 min. The four different kidney groups are as follows: Panel A – porcine kidneys with an approximate warm ischemia time of 20 min and a cold ischemia time of 3-5 hr (n = 3 for each tonicity); Panel B – porcine kidneys with a warm ischemia time of 25-40 min and a cold ischemia time of 2-4 hr (n = 4 for each tonicity); Panel C – porcine kidneys with a warm ischemia time of 25-40 min and a cold ischemia time of 5 d (n = 3 for each tonicity); Panel D – human kidneys with an unknown warm ischemia time and a cold ischemia time of 3 d (n = 2 for each tonicity).

From Figure 4.6, the transient flowrate period right after time = 0 for the isotonic case is somewhat difficult to decipher. When a CPA is introduced to the vasculature, we expect fluid from the tissue to move into the vasculature, analogous to the osmotic response of a single cell. From an initial inspection of the situation, it is reasonable to expect an increase in the effluent flowrate to accommodate the flux of fluid from the tissue to the vasculature due to an increase in the osmotic driving force. Also, the capillary radius has been suggested to increase due to the presence of CPA in the vasculature from the classic Krogh cylinder model of an organ [104,114]. In Figure 4.6, we do notice an increase in flowrate in some kidney groups. However, in Panel A, we see an initial decrease in flowrate for a couple replicates. This is somewhat puzzling and makes for the overall interpretation of the transient flowrate period muddled. First, we have kidneys of varying quality, and second, it is difficult to develop a full intuition about the problem when size changes of the tissue are not considered along with vasculature size changes as in the classic Krogh cylinder model [104,114]. Nevertheless, flowrate changes of the isotonic case either return to about their original values or stay elevated. Such a trend does not pose a challenge for perfusing the entire kidney, unlike what is seen for the hypotonic case.

In Figure 4.6, the transient flowrate response for the hypotonic case is minimal, with some cases of an increase in flowrate being seen. If we do expect the dominant trend during the transient period to be an increase in flowrate, then the hypotonic buffer should lessen that increase due to a reduction in the osmotic driving force from tissue to vasculature. Looking past the transient period though, all flowrates dramatically reduce to a fraction of their original value before CPA addition. As such, this is an important phenomenon to understand, as the resistance to flow is increasing with the capillary diameter presumably decreasing. We know that the decrease in flowrate is in part due to an increase in resistance and not only solution accumulation in the kidney, as solution accumulation only accounts for about 30% of the influent flowrate using the data of Panel A as an example (data not shown). As such, we can plot the resistance to flow over the course of the perfusion. Figure 4.7 shows the change in resistance for the perfusion using the data from Panel A again as an example.

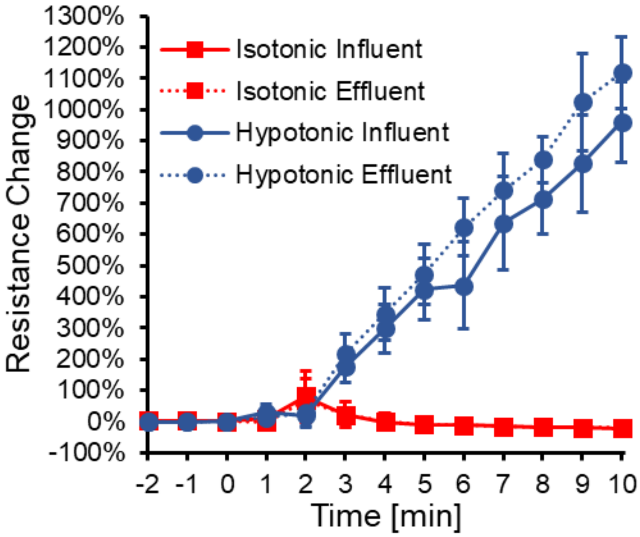

Figure 4.7. The normalized resistance to flow for porcine kidneys perfused with 10% (m/v) EG in either isotonic or hypotonic buffer. All kidneys were equilibrated on a mass basis with the isotonic buffer for 30 min, and EG addition is represented by time = 0 min. The kidneys have an approximate warm ischemia time of 20 min and a cold ischemia time of 3-5 hr (n = 3 for each tonicity). Resistance is calculated as per the definition in Pegg et al [104], and we are using both the influent and effluent flowrates to calculate resistance. Error bars represent the standard error of the mean.

Figure 4.7 indicates that we need to be aware of the increased vascular resistance to flow induced by a hypotonic buffer. Although a hypotonic buffer could load more CPA in a shorter amount of time as seen with Figure 4.5 in principle, certain regions of the kidney might not be effectively reached with CPA due to the increase in resistance, and these regions would have to rely on CPA diffusion in the tissue to reach a desired CPA concentration. To address this potential limitation of a hypotonic buffer and understand the CPA distribution within a kidney in general, we assessed both the spatial and temporal distribution of Me_2SO using CT, as will be discussed in the following section. Before we address the distribution, it should be noted that hypotonic buffer does not have to be used for the entire CPA loading protocol. In our previous work at the single cell level, hypotonicity of the buffer was varied across the two steps of the CPA loading protocol [29]. As such, the hypotonicity used at the organ level could be leveraged for certain steps while perhaps avoiding a large increase in vascular resistance. Swelling has often been overlooked during CPA addition due to the desire of vitrifying cells in their shrunken state and not diluting intracellular solutes and thus increase the probability of ice nuclei formation [51]. However, as we have mentioned, swelling is just one step of our single cell CPA loading strategy, and we did increase the tonicity of the buffer to shrink our cells down before vitrification [29]. The same strategy could be applied at the organ level and the first step to accomplishing this would be to show flowrate recovery after hypotonic loading by increasing the buffer tonicity. In Figure 4.8, we do show that we can obtain flowrate recovery after a flowrate decrease by switching the buffer tonicity from hypotonic to isotonic. Figure 4.8 details that edema does not have to be a detriment in protocols by only increasing vascular resistance [103], but it could potentially be leveraged during certain steps of a protocol and flowrate recovery is possible.

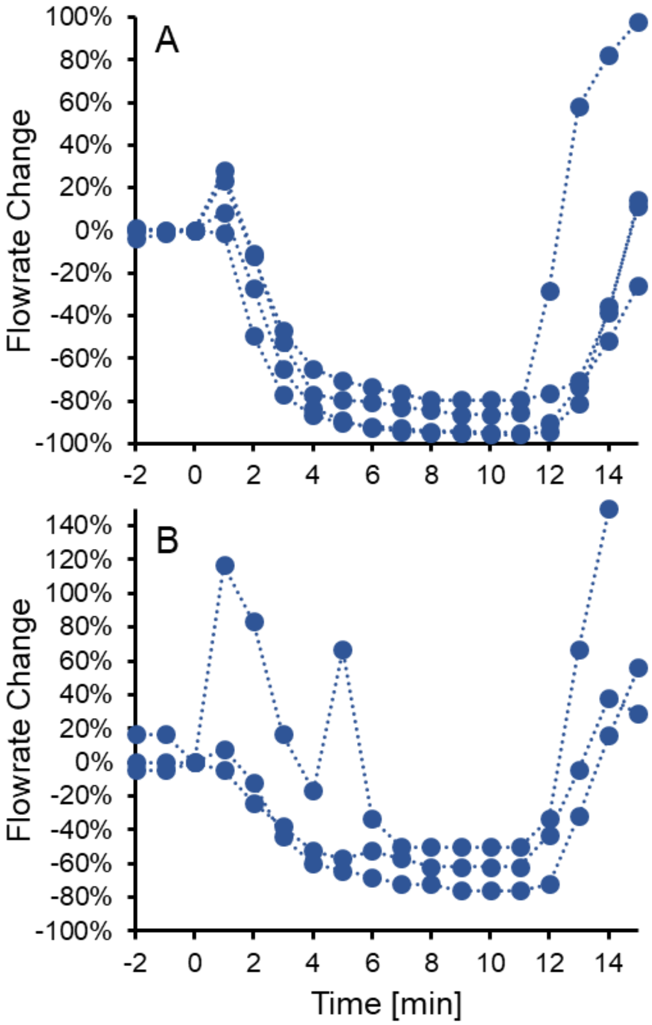

Figure 4.8. The normalized effluent flowrate change of two different kidney groups perfused with 10% (m/v) EG in hypotonic buffer. All kidneys were equilibrated on a mass basis with the isotonic buffer for 30 min, and EG addition is represented by time = 0 min. At time = 10 min, the perfusate was switched from EG in hypotonic buffer to EG in isotonic buffer. The two different kidney groups are as follows: Panel A – porcine kidneys with a warm ischemia time of 25-40 min and a cold ischemia time of 2-4 hr (n = 4 for each tonicity); Panel B – porcine kidneys with a warm ischemia time of 25-40 min and a cold ischemia time of 5 d (n = 3 for each tonicity). The data presented up until time = 10 min can be found in Figure 4.6 as well.

4.4.2 CPA Distribution within the Kidney

To assess the distribution of Me_2SO within the kidney, we adopted a CT method in the literature [23] that was subsequently used to develop cryopreservation protocols for bovine ovarian tissue [24,25]. We can also see CT being used to track the Me_2SO

distribution within rat hearts [15]. As Me_2SO itself is radiopaque, a foreign contrast agent is not needed and the Me_2SO distribution can be more accurately assessed. Also, since we are interested in buffer tonicity as a manipulation variable, a foreign contrast agent makes tonicity variable analysis more difficult. To begin our analysis, we first established a standard curve between X-ray attenuation and Me_2SO concentration in the fluid phase, which is shown in Figure 4.9.

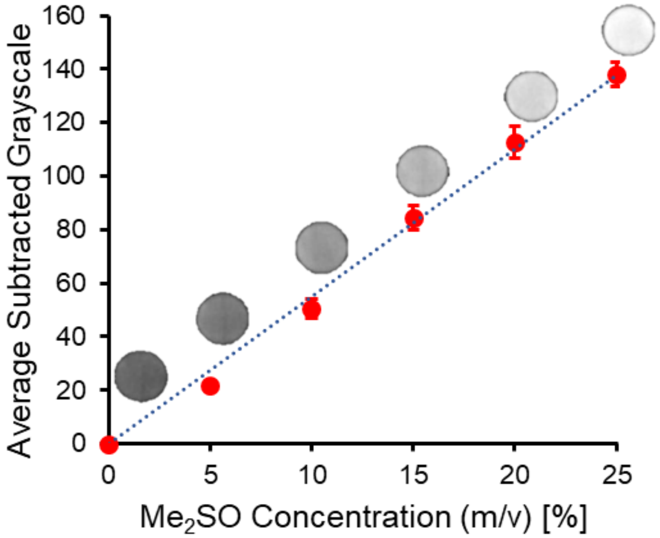

Figure 4.9. A standard curve established between X-ray attenuation represented as computer grayscale and the Me_2SO concentration in the fluid phase. The attenuation is a subtracted value where the background attenuation of the buffer is subtracted off. Three different solutions were tested at each of the Me_2SO concentrations: Me_2SO in water, Me_2SO in isotonic buffer, and Me_2SO in hypotonic buffer. Each solution was tested in triplicate, and since we're expressing the subtracted attenuation, all measurements can be combined at a given Me_2SO concentration. Error bars represent the standard deviation of the nine measurements for each concentration. The grayscale circles are examples of 24-well plate wells of Me_2SO in water for each Me_2SO concentration. For our setup, the linear range ends at about 25% (m/v) Me_2SO.

With a standard curve established, we were able to estimate the Me_2SO concentration of our perfusion experiments as a function of time and space. We perfused six kidneys total with 15% (m/v) Me_2SO, with three kidneys perfused with Me_2SO in isotonic buffer and three kidneys perfused with Me_2SO in hypotonic buffer. We also were able to separate the kidney into two different spatial regions through time—the cortex and the medulla. Overall, Figure 4.10 shows the Me_2SO concentration estimates of all six kidneys perfused for both the cortex and medulla.

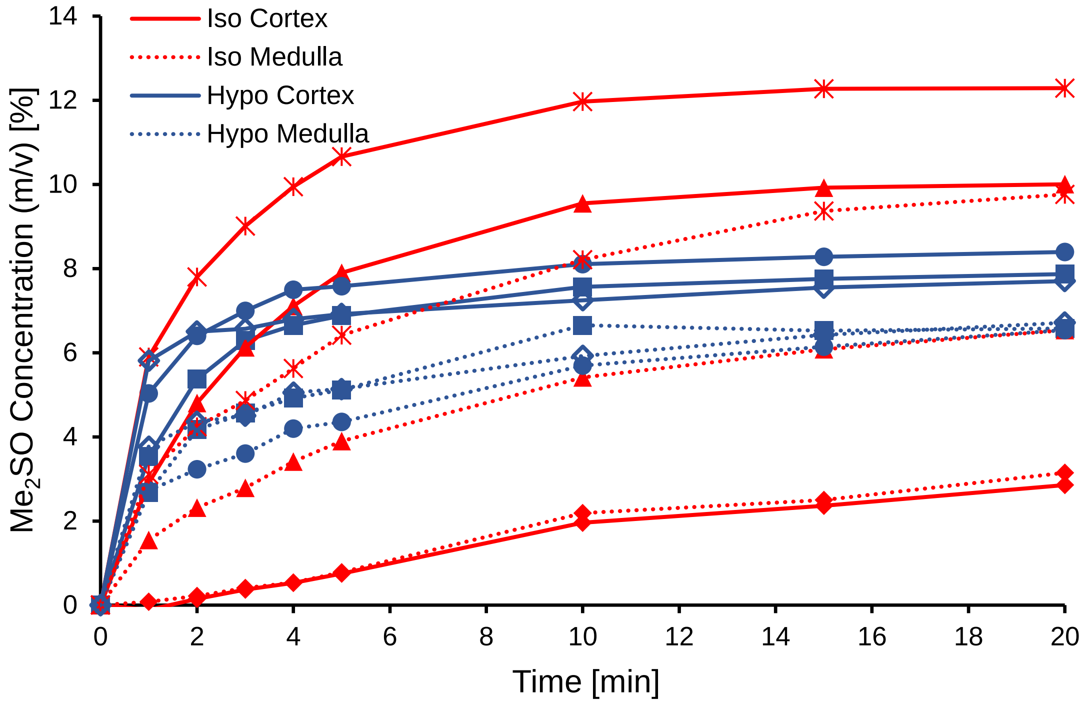

Figure 4.10. The Me_2SO concentration plotted as a function of time for porcine kidneys perfused with either 15% (m/v) Me_2SO in isotonic (n = 3) or hypotonic buffer (n = 3). For the six kidneys perfused, the Me_2SO concentration is plotted for both the cortical and medullary regions. Each kidney is represented by its own symbol, so both the cortical and medullary curves of the same kidney can be identified together. For the hypotonic curves, there is an uncertainty of ± 1.3% in the Me_2SO concentration due to a difference in the background attenuation between the isotonic and hypotonic buffer, where the hypotonic buffer has a lesser attenuation. Me_2SO was introduced after the standard 30 min equilibration period with isotonic buffer (time = 0 min). The kidneys have a warm ischemia time of 25-40 min and a cold ischemia time of approximately 18 hr.

From Figure 4.10, we can assess the impact of the tonicity variable but also the difference between the spatial regions of the cortex and medulla. Starting with the spatial variation, Fahy has described the difficulty of equilibrating the medullary region with CPA when compared to the cortex, and a leading explanation could be the difference in blood flow between the two regions with the cortex receiving about 90% of renal blood flow and the outer medulla about 10% [47,49]. In Figure 4.10, we note that most medullary curves are below that of their cortical counterparts. However, one isotonic kidney perfusion appears to confound the results. The cortical and medullary curves for this kidney are the bottom two curves of Figure 4.10. The difference between these two curves is small in comparison with the other paired curves, though. As such, a paired t-test yields a statistically significant difference between the Me_2SO concentration of the cortical and medullary regions for the 20 min timepoint with a p-value of 0.027. Overall, Figure 4.10 shows empirical evidence that we can make a distinction in Me_2SO concentration between different regions of the kidney and the majority of replicates indicate the historical reporting of the medullary region being more difficult to equilibrate. In addition, we see further evidence that specimen quality or the limitations of the slaughterhouse model could be at play for the confounding kidney in Figure 4.10, and we will discuss slaughterhouse model limitations later on, specifically drawing attention to the fact that the confounding kidney appeared to have more air bubbles from image inspection than the other kidneys.

Moving on to the tonicity variable, again, one kidney perfusion has the potential to confound results. Unlike the spatial region analysis that showed a statistically significant difference between the cortical and medullary regions at the 20 min timepoint, a paired t-test yields a p-value of 0.94 for comparing the two tonicities at the 20 min timepoint, yielding no statistical difference. However, if we set aside the confounding kidney, we note that most isotonic treatments yield a higher Me_2SO concentration at the 20 min timepoint. As we’ve mentioned earlier, the increase in vascular resistance for the hypotonic treatment yielded concern that some regions of the kidney might not be perfused. From inspection of the CT images, no large dark regions on the images were noted, indicating that Me_2SO appears to be reaching all regions to some extent and the extreme scenario of large regions not being perfused does not seem to be the case. Figure 4.10, however, indicates that the low flowrate induced by the hypotonic treatment could have a detrimental effect on the Me_2SO concentration. Perhaps the lower flowrate induced by the hypotonic treatment creates a difference in the Me_2SO concentration between the isotonic and hypotonic treatments that is analogous to the difference in cortical and medullary regions due to the difference in blood flow of the two regions. Overall, the low flowrate induced by a hypotonic buffer does appear to be a challenge that needs to be overcome if a hypotonic buffer is to be leveraged during perfusion.

Although no large regions on the CT images appeared dark, we still need to address the fact that the Me_2SO concentration is not approaching 15% (m/v). Even over a longer perfusion time as seen for a 60 min perfusion in Figure 4.11, we still do not see any concentrations approaching 15% (m/v). In Figure 4.11, we note that the cortical region of a kidney perfused with Me_2SO in isotonic buffer does appear to be at a steady-state Me_2SO concentration of slightly over 12% (m/v). There are two explanations for why the concentration is below 15% (m/v). The first could be too low of a solids estimate. We are using a rat papillary solids estimate for the medulla at 15% and then using the CT data at time = 0 min to estimate the solids content for the cortex (15.5%). In order for the isotonic cortex curve of Figure 4.11 to reach 15% (m/v) Me_2SO, we would need a medullary solids estimate of approximately 30%. Our solids estimate could be low, but this would not explain the low concentration predictions of the other curves, including the rest of the data from Figure 4.10. For example, in Figure 4.10, there is an isotonic cortex curve that appears to approach a steady-state concentration of 10% (m/v). Even if we considered a medullary solids content of 30%, we would not account for the lower than 15% (m/v) Me_2SO steady-state concentration. In fact, we would need a medullary solids content estimate of approximately 42%, which is outside of the range we discussed in the Methods and Materials section. The more likely scenario is that we are having trouble reaching all regions of the kidney for both tonicities. There were no large dark regions on the CT images but some small regions could be excluded from being perfused or the time scale of Me_2SO diffusing in the tissue to reach those regions is much longer than what we captured in our experiments. A potential explanation for this lower than expected Me_2SO concentration could be due to some capillary beds being blocked due to coagulated blood that could not be flushed. As we will describe later, there are pitfalls to using the slaughterhouse model and we also chose to forego an anti-coagulant in the perfusate to keep our perfusate composition simple and better isolate the tonicity variable. Nevertheless, the slaughterhouse model does seem to have an impact on the accuracy of results, but we have demonstrated a CT method including a unique spatial region analysis of the kidney that can be used to inform mass transfer models.

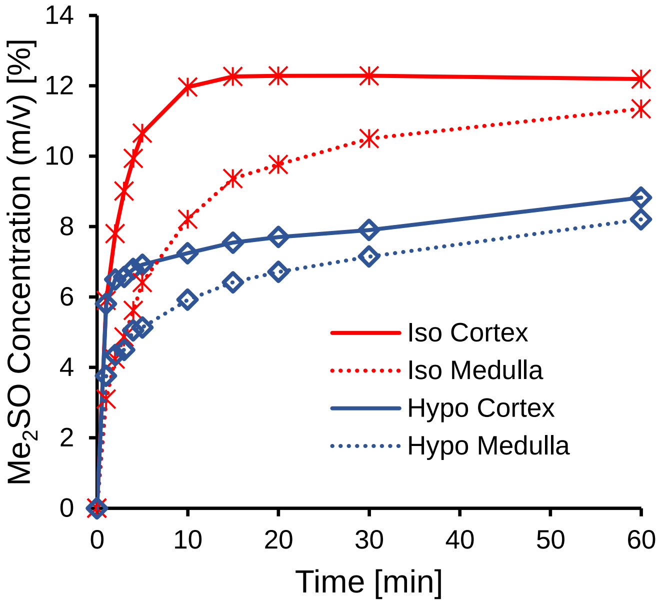

Figure 4.11. The Me$_2$SO concentration plotted as a function of time for porcine kidneys perfused with either 15% (m/v) Me$_2$SO in isotonic (n = 1) or hypotonic buffer (n = 1). For the two kidneys perfused, the Me$_2$SO concentration is plotted for both the cortical and medullary regions. For the hypotonic curves, there is an uncertainty of ± 1.3% in the Me$_2$SO concentration due to a difference in the background attenuation between the isotonic and hypotonic buffer, where the hypotonic buffer has a lesser attenuation. The data up until time = 20 min can also be found in Figure 4.10. Me$_2$SO was introduced after the standard 30 min equilibration period with isotonic buffer (time = 0 min). The kidneys have a warm ischemia time of 25-40 min and a cold ischemia time of approximately 18 hr.

4.4.3 Osmotic Damage Assessment of the Kidney

In addition to adopting a CT method to help inform a mass transfer model within the toxicity cost function framework, we also sought to develop a metric to assess osmotic tolerance limits. At the organ level during a CPA addition and removal protocol, volume excursions of both the tissue and cells are expected, and as such, those volume excursions can cause mechanical damage. Assessing the mechanical damage of the tissue independently of the cells is a difficult proposition. For this work, we focused on the mechanical damage experienced by the cells. Specifically, we conducted a LDH assay on the effluent during perfusion and estimated the cell death from the results. We conducted the LDH assay for several different experiments. The first experiment purely looked to isolate osmotic damage. To do this, we did not include any CPA in our perfusate but specifically looked at the difference in LDH content between a kidney perfused with isotonic buffer versus one perfused with hypotonic buffer. This experiment gave us the maximum amount of osmotic damage that could be incurred from the use of our hypotonic buffer. The other two experiments were perfusions of two different kidney groups of varying cold ischemia time with 10% (m/v) EG in either isotonic or hypotonic buffer. Figure 4.12 shows the estimated cell death of all three experiments.

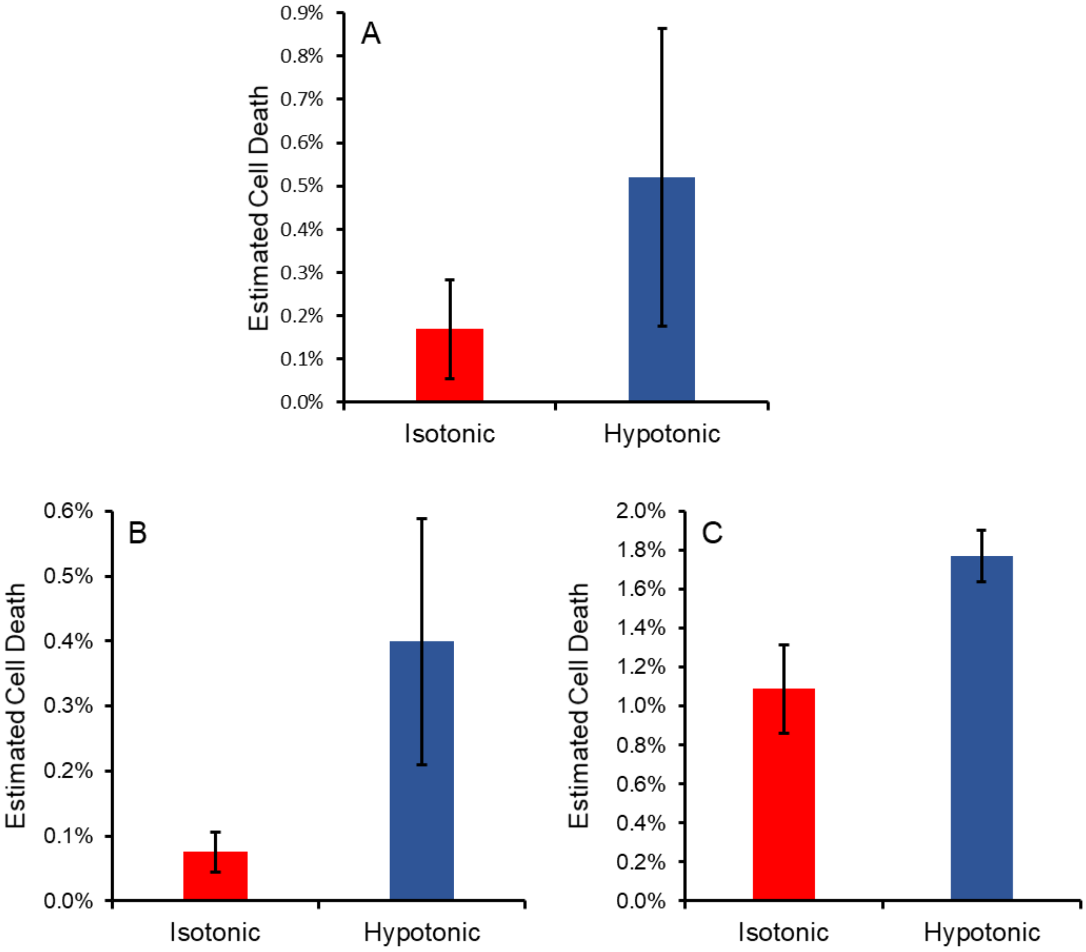

Figure 4.12. The estimated cell death between the isotonic and hypotonic buffer treatments for three different experiments. All kidneys were equilibrated on a mass

basis with the isotonic buffer for 30 min. After the equilibration, test solutions were introduced to the kidneys according to the strategy presented in Figure 4.4 for one experiment (Panel A). For the other two experiments (Panels B and C), we perfused the kidneys with 10% (m/v) EG in either buffer according to the strategy presented in Figure 4.4. The isotonic buffer equilibration and Triton X-100 introduction were kept the same as with the buffer only experiment. Panel A – porcine kidneys perfused with either isotonic or hypotonic buffer (see Fig. 4.4). The warm ischemia time was 25-40 min and the cold ischemia time was 3.5-5.5 hr (n = 1 for each tonicity) or 19-21 hr (n = 2 for each tonicity). Replicates were combined to make n = 3 for each tonicity. Panel B – porcine kidneys perfused with 10% (m/v) EG in either buffer with a warm ischemia time of 25-40 min and a cold ischemia time of 2-4 hr (n = 4 for each tonicity). Panel C – porcine kidneys perfused with 10% (m/v) EG in either buffer with a warm ischemia time of 25-40 min and a cold ischemia time of 5 d (n = 3 for each tonicity). Error bars represent the standard error of the mean.

From Figure 4.12, we see that the hypotonic treatment appears to be more damaging than the isotonic treatment. However, the magnitude of the estimated cell death of each treatment is fairly low, perhaps innocuous for a CPA addition and removal strategy that leverages either treatment. Focusing on Panel A where only buffer was perfused through the kidneys, we should theoretically obtain the most osmotic damage and not have any toxicity damage from a CPA that could confound results. The error bar for the hypotonic case is much larger than the isotonic case because one hypotonic kidney released much less LDH during the Triton X-100 exposure than its counterparts, which increases the estimated cell death. Nevertheless, there is no statistical difference between the isotonic and hypotonic cell death estimates using a 2-way ANOVA (without interaction) looking at the effect of tonicity and animal the kidneys were taken from (p-value of 0.28 for tonicity). Overall, we can use this LDH assay to find the hypotonicity at which cell death dramatically increases to set our upper osmotic tolerance limit. As we decrease the tonicity to find the osmotic tolerance limit, the swelling would become more of a problem. At some point, we would expect no effluent flowrate as we decrease tonicity. Perhaps flowrate becomes the limiting constraint rather than cell death when using a hypotonic buffer. If we do want to establish the limit in the future, we can use the technique as outlined in Figures 4.4 and 4.8 to recover the effluent flowrate and capture the LDH released during the hypotonic treatment. For very low tonicities, we might have to increase the isotonic perfusion time after the hypotonic treatment to recover the flowrate fully and capture the LDH released.

Overall, the LDH assay is a promising tool to establish osmotic tolerance limits at the organ level and limiting the CPA addition and removal protocol space to limit mechanical damage.

Looking at Panels B and C where EG was perfused through the kidneys, we notice a similar trend as with the buffer only experiment of Panel A. The hypotonic buffer imparts a slightly greater cell death than the isotonic buffer. From this result, we see that EG does impart a signal reduction to the LDH assay (comparison of Panels A and B reveals a ~55% signal reduction for the isotonic case and a ~25% signal reduction for the hypotonic case, assuming minimal CPA toxicity), but this signal reduction does not confound the result of the experiment. We have also seen a maximum signal reduction of ~40% for LDH assays conducted on endothelial cells in the presence of EG (results not shown). This is important, as we could use this same LDH assay to assess CPA toxicity. To do this, we could potentially save effluent samples during CPA loading and removal but not introduce Triton X-100, conduct hypothermic storage of the kidney to allow for apoptosis to occur, and then conduct an isotonic buffer perfusion followed by Triton X-100 introduction. We would estimate cell death in a similar manner as described in the Methods section, but the LDH released during the isotonic buffer perfusion after hypothermic storage would be attributed to apoptosis and add to our cell death estimate. In conjunction with the potential of extending the LDH assay to CPA toxicity, we also notice in Panel C that we estimate greater cell death for both buffers when compared to Panel B. We attribute this difference to the fact that the cold ischemia time is much greater in Panel C than Panel B, and the kidneys of Panel C would be considered to be of lesser quality either from more background LDH in the effluent from cells dying over the course of the cold ischemia period or from more cells dying during the actual perfusion. Regardless, the LDH assay captures this phenomenon and could be extended to characterizing specimen quality as we will discuss in the following section.

4.4.4 Comments on Specimen Quality and the Slaughterhouse Model

The slaughterhouse model is an attractive option for the researcher as it allows many specimens to be acquired for a low cost and it does not require the sacrifice of additional animals. However, in our experience using the slaughterhouse model for porcine kidney perfusions, we have encountered some pitfalls that can lead to less accurate and potentially confounding results. The first pitfall is potential variety in the specimens acquired as the animals can vary in sex, age, weight, and overall health. The researcher has potentially less background information on the animal before organ acquisition when compared to that of a research animal. As an example, we had one kidney confound our CT experiment, and we had one kidney exhibit a much smaller release of LDH during our osmotic damage experiment. With a slaughterhouse model, flagging outlier animals can be more difficult based on metrics of the animal's history. Also, the timing of the experiments can have greater variation resulting in varying ischemia times, as the scheduling of experiments is a function of slaughterhouse processing times. As an example, the cold ischemia times for our CT experiment were longer at about 18 hours when compared to the times of our mass and flowrate change experiments. This was due to a fixed slaughterhouse processing time and a fixed time window to take CT images. If a research animal is used, the researcher can control the time of organ acquisition and subsequently the cold ischemia time.

Regardless of the animal model used, we did develop some experimental techniques that can be used to probe the quality of the specimen. As mentioned previously, Figure 4.12 indicated that more LDH is released as cold ischemia time increases, as more cells will die as cold ischemia time increases and there will be a greater buildup in the specimen before a perfusion. To leverage this principle, we compared the LDH content of the 30 min isotonic equilibration period of all available experiments. The results are presented in Figure 4.13 by showing the total LDH released for three different cold ischemia times.

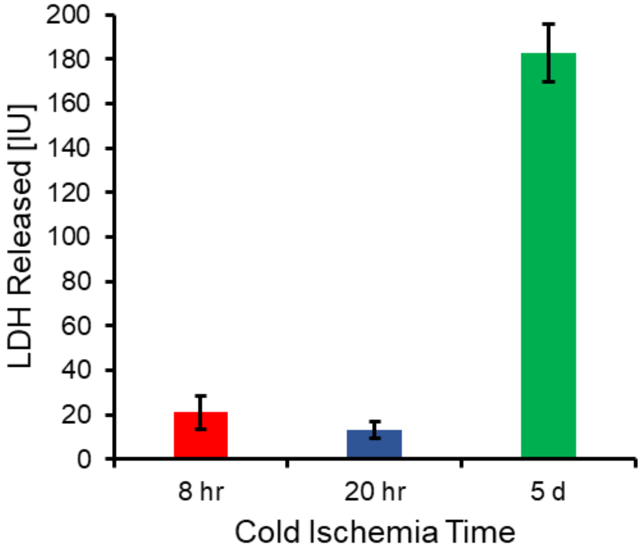

Figure 4.13. A comparison of the LDH released as a function of increasing cold ischemia time during the initial isotonic equilibration period of 30 min. All kidneys have a warm ischemia time of 25-40 min. The cold ischemia time groups are less than or equal to 8 hr, approximately 20 hr, and approximately 5 d. The error bars represent the standard error of the mean.

Figure 4.13 shows a large jump in LDH released between the 20 hr and 5 d cold ischemia time groups. Using this result alone, we would interpret both the 8 hr and 20 hr groups to be comparable in quality. However, we have seen confounding results from specimens that have about a 20 hr cold ischemia time, and we have also seen some confounding results from specimens that have less than a 20 hr cold ischemia time but have a 25-40 min warm ischemia time compared to a 20 min warm ischemia time. As such, another metric would be useful to try to understand why some kidneys respond in a seemingly atypical fashion. A potential metric that we propose comes from the 30 min isotonic equilibration period as well. During the 30 min equilibration period, we compared the difference between the effluent flowrate at the end and beginning of the equilibration period across experiments. Figure 4.14 presents the results of this comparison, and we found an interesting trend where kidneys with a greater ischemia time tended towards vasoconstriction (flowrate reduction), while kidneys with a shorter ischemia time tended towards vasodilation (flowrate increase). At normal physiological conditions, the kidney autoregulates blood flow through either vasoconstriction or vasodilation through complex feedback loops [69]. As we've previously mentioned, during perfusion, avoiding an increase in vascular resistance (i.e. vasoconstriction) is desirable, and some common techniques to avoid vasoconstriction involve adding a vasodilator [103] or leveraging pulsatile machine perfusion [33]. In our case, we used a simple perfusate composition and perfusion setup which should not bias the kidney towards either vasoconstriction or vasodilation. Instead, the particular condition of the kidney being perfused should drive the change in vascular resistance. As such, the change in flowrate for our experimental setup appears to correlate with ischemia time. This simple metric could be leveraged in the future to screen specimens and give a prediction of expected osmotic response when compared to our experimental group of the smallest ischemia times.

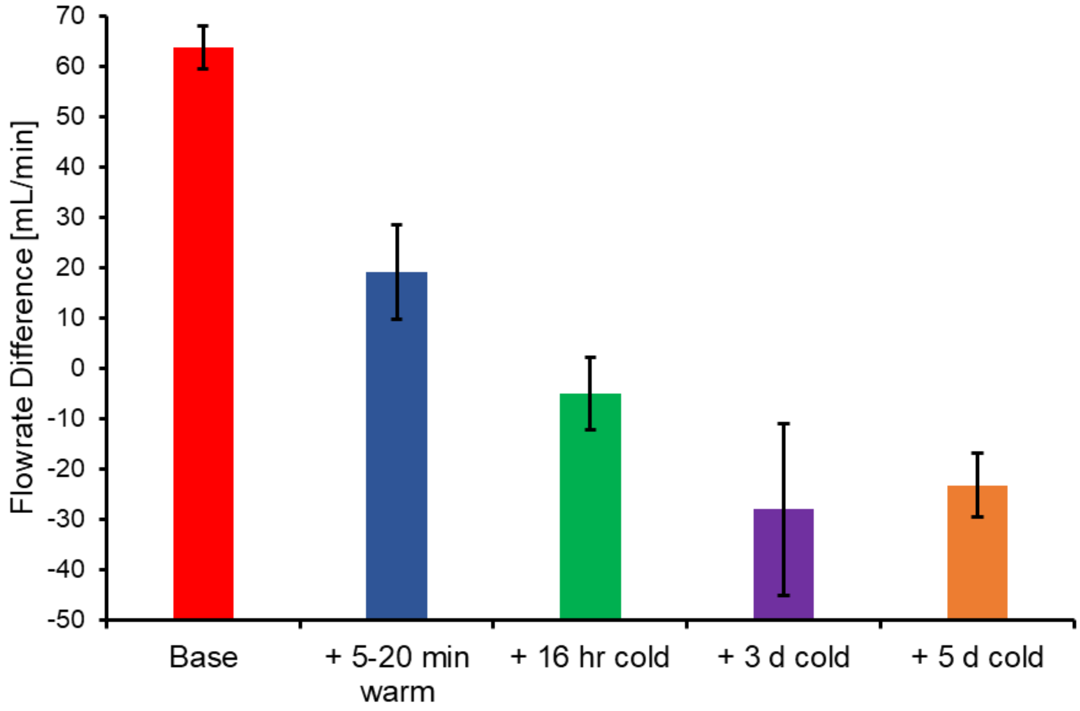

Figure 4.14. A comparison of the difference in effluent flowrate between the end and beginning of the 30 min isotonic equilibration period. The first bar represents the base change as seen for our porcine kidney group with a warm ischemia time of 20 min and a cold ischemia time of 3-5 hr. Moving to the second bar, we have a porcine kidney group where the warm ischemia time is increased by 5-20 min and the cold ischemia time is comparable to the base group. Moving past the second bar, each subsequent bar has the same warm ischemia time as the second but with an additional amount of cold ischemia time. One caveat is that the fourth bar represents our human kidney group and

the warm ischemia time is an unknown. Error bars represent the standard error of the mean.

Moving on from specimen quality, we did encounter some other pitfalls. Unlike some other porcine slaughterhouse studies [63,126] where they had complete control over the animal at the time of slaughter, we were only able to obtain kidneys in a way that did not change the timing of the slaughterhouse’s processing schedule. In the other slaughterhouse studies, they were able to harvest the kidneys via an en-bloc technique where a section of the abdominal aorta and inferior vena cava were removed with the kidneys. With our constraints, kidneys were resected individually as quickly as possible during the processing of the animal. Also, we did not include heparin within our flush solution unlike the other studies in order to better isolate the tonicity variable. Such an overall approach, when compared to the other studies, introduces some pitfalls, namely some coagulation within the kidney, introduction of air bubbles into the vasculature, and a cannula position that can be past the first arterial bifurcation. Even with flushing the kidneys with 500 mL of isotonic buffer after harvest (which is on the higher end of other studies [53,63,66,126]), we still saw blood in the effluent collected during the 30 min isotonic buffer equilibration period. In Figure 4.15, we show evidence of air bubbles in our kidneys as well as a cannula position that appears to be past the first arterial bifurcation on a CT image. Overall, these pitfalls can decrease the accuracy of an experiment and increase the probability of confounding results. However, the slaughterhouse model proposed in this work has shown the ability to help guide experimental techniques in the future and has established a proof of concept for the use of leveraging buffer tonicity in a CPA addition and removal protocol. The experimental methods outlined in this work can be further refined with our quick and cost-effective slaughterhouse model before we transfer to a research animal model to acquire final data for the toxicity cost function approach.

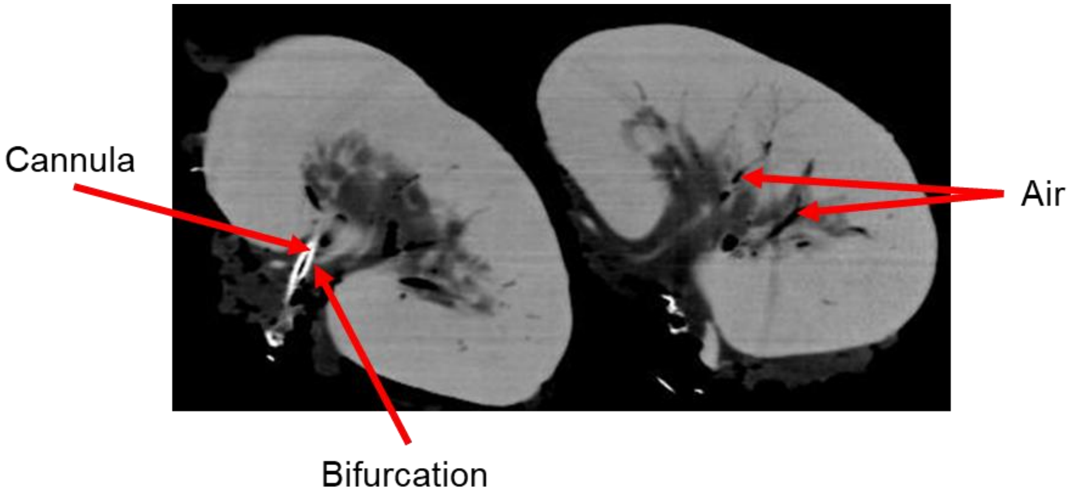

Figure 4.15. A CT image of two kidneys before a perfusion took place. The left kidney of the image details a cannula position that appears to be past the first arterial bifurcation. Lighter pixels of the image indicate greater X-ray attenuation, and the cannula is clearly visible on the image since a Me_2SO solution fills the cannula. The right kidney shows some pockets of air trapped in the vasculature, which will appear as black pixels.

4.5 Conclusions and Future Directions

In this work, we began to build a foundation of moving the toxicity cost function technique to the organ regime. To start, we assessed the idea of loading CPA in hypotonic buffer in porcine kidneys. In a previous study at the single cell level [29], the toxicity cost function approach identified loading CPA in hypotonic buffer as a less toxic method when compared to conventional protocols. At the organ level, we noted greater swelling of kidneys perfused with CPA in hypotonic buffer when compared with their isotonic counterparts for our porcine kidney group that had the lowest ischemia time. This is an encouraging sign, as greater swelling indicates loading more CPA in a shorter amount of time, at least at the single cell level. However, the delivery of CPA into an organ using perfusion is much different than exposing cells to an infinite reservoir of CPA. When looking at the use of a hypotonic buffer, we have to consider the increase in vascular resistance induced by swelling and the potential of not effectively perfusing the farthest downstream regions of the kidney due to lower flowrates. We saw a lower flowrate phenomenon in all kidneys perfused with a hypotonic buffer. As such, we conducted CT scans of perfused kidneys to assess the difference in the CPA distribution between perfusing a kidney with CPA in hypotonic buffer versus perfusing a kidney in isotonic buffer.

CT results indicated no statistical difference between the CPA distribution when using a hypotonic or isotonic buffer. However, one kidney appeared to produce outlier results and confounded the analysis. Nevertheless, we were able to identify several key takeaways from the study: 1) hypotonic buffer needs to be further evaluated as an effective method to load CPA at the organ level, 2) we can effectively quantify both the spatial and temporal CPA distribution within the kidney, and 3) the CT method can be leveraged to inform an organ level mass transport model that will serve as the cornerstone of our toxicity cost function approach. In conjunction with a hypotonic buffer increasing vascular resistance, we also considered the potential of osmotic damage. To assess osmotic damage, we performed a LDH assay on collected effluent. We also identified several key takeaways from the study: 1) there is no statistical difference between the estimated osmotic damage of the two buffer treatments, 2) the assay appears to be an effective technique to assess osmotic damage, and 3) the assay can be potentially expanded to assess CPA toxicity, which is another major component of the toxicity cost function approach.

Altogether, our slaughterhouse study provided some key learnings that we can leverage moving forward. We identified experimental techniques that can fulfill the necessary measurements of CPA concentration distribution, osmotic damage, and perhaps CPA toxicity. All of these measurements are key to developing a toxicity cost function at the organ level. We also were able to take physical change data of perfused kidneys which can help to inform a future mass transport model as well. Although some pitfalls and limitations of our slaughterhouse model were identified, we were able to identify key trends in our experiments. In the end, we have developed a solid experimental base from which we can build off in the future. The slaughterhouse model can be used to refine experimental techniques and rule out potential protocols before moving to a research animal model to inform a final version of our toxicity cost function.

4.6 Conflicts of Interest

The authors have no conflicts of interest.

4.7 Acknowledgements

This work was partially funded by the Cryonics Institute. We would like to thank both Stanton's Slaughter House (Albany, OR) and Mohawk Valleys Meats (Springfield, OR) for allowing us to acquire porcine kidneys for our studies, as well as the Pacific Northwest Transplant Bank (Portland, OR) for allowing us to acquire human kidneys. We would also like to thank Jason Wiest and Cynthia Viramontes for operating the CT scanner. Many thanks to Emi Ampo and Solomon Baez for laboratory assistance.

5. GENERAL CONCLUSION

5.1 Summary

Vitrification is a very exciting cryopreservation technique that completely suppresses ice formation and is one that could be applicable to complex biological specimens such as tissues and organs. The other cryopreservation technique of slow cooling allows extracellular ice to form and is thought to not be applicable to complex specimens, since they cannot tolerate extracellular ice formation. As such, vitrification is being pursued by the cryobiology field for complex specimen cryopreservation. The biggest obstacle for vitrification is toxicity, though, due to the large concentration of CPAs required. To minimize toxicity and allow the specimen to survive the cryopreservation process, there are many knobs of a CPA addition and removal protocol that can be turned. For example, we can manipulate the temperature and exposure time of a protocol in conjunction with the CPA type. One quickly realizes that there are so many different protocol combinations that it becomes impossible to test them all experimentally. To assess all possible combinations and find a global minimum of toxicity, a mathematical approach most likely needs to be employed. Our group has adopted a mathematical optimization strategy for the toxicity problem. We have proposed a toxicity cost function that can be minimized in order to find the least toxic vitrification protocol. However, the approach is still in its infancy and there are many research avenues to extend its applicability. In this work, we discussed research topics expanding on both the protocol complexity and specimen complexity of the toxicity cost function.

5.1.1 Chapter 2

In Chapter 2, we investigated the protocol complexity research front. Protocol variables such as temperature, exposure time, and CPA concentration are fairly well understood as far as general toxicity trends are concerned. However, CPA mixture type is a much vaster variable, since potentially any chemical could be a CPA. Finding the best CPA or combination of CPAs is then vary challenging. Even with our mathematical approach, we still need to characterize the toxicity of a vast chemical library to leverage the CPA mixture type variable in the attempt of reducing toxicity. Also, many current vitrification protocols leverage multi-CPA solutions, increasing the number of CPA mixture types. Chapter 2 focused on characterizing the toxicity of five of the most common CPAs along with their binary and ternary mixtures. To accomplish this, we leveraged automated liquid handling to expose BPAEC to the various CPA solutions of interest. In doing so, we established the most comprehensive toxicity dataset in the cryobiology literature, while establishing a high-throughput CPA toxicity screening pipeline.

5.1.2 Chapter 3

In Chapter 3, we moved on from the protocol complexity research front and started to move up the specimen complexity ladder from our single cell investigations of BPAEC. Specifically, we turned our attention to the cryopreservation of tissues. At the tissue level, our primary research attention turns to an adequate mass transfer model. At the heart of the toxicity cost function are spatial and temporal CPA concentration predictions based on a mass transfer model. At the single cell level, we rely on the classic 2P membrane transport model, but at the tissue level, we have to contend with extracellular mass transfer as well. There are many transport complexities that arise at the tissue level and all should be considered to give the most accurate mass transfer predictions. If all tissue-based phenomena that influence transport can be accounted for, we hypothesize that we can craft a general tissue transport model, and this is what we pursued in Chapter 3. By augmenting a comprehensive acellular tissue model in the literature with cells, we were able to show a generality in the developed model. We showed that the model could give CPA concentration predictions for two very different tissues—articular cartilage and pancreatic islets.

5.1.3 Chapter 4

For the last chapter of this work, we moved to the most complex specimen regime of organs. Specifically, we looked at kidneys. Unlike tissues, organs have much more complex geometries and various functional compartments that most likely render a general model unlikely. However, previously discussed modeling strategies can be a good starting point. In Chapter 4, though, we move away from the development of mass transfer models and take an overview look of how to apply the toxicity cost function to organs. The first step we took was to assess the osmotic response of the kidney using different perfusate compositions, drawing parallels with what we had seen in the past with single cells. At the single cell level, our toxicity cost function approach identified leveraging the osmotic response to reduce toxicity. After our initial osmotic response investigation, we turned to developing more model informing experimental methods. To accurately develop an organ level mass transfer model, we need to have some data to compare against the model predictions. As such, in Chapter 4, we developed a CT method to assess the distribution of DMSO within a kidney both spatially and temporally. We also developed an LDH assay to assess osmotic damage within the kidney. Developing osmotic tolerance limits outside of the single cell regime is a wide-open research front. Along with these experimental methods, we also investigated the quality of kidneys that can be obtained from a slaughterhouse source. Obtaining kidneys from a slaughterhouse is the cheapest option and the one that can provide a high volume of supply for the many experiments that need to be conducted. However, the specimen quality can vary due to the lack of control the experimenter has at the slaughterhouse.

5.2 Future Work Considerations and Conclusions

The toxicity cost function is still a relatively new approach to vitrification but it has shown much promise. As such, there are many investigations that need to be conducted to further its applicability as we move to more complex protocols and specimens. In this work, we have touched on several different research fronts of the toxicity cost function and there are multiple investigations that can be spawned from each one.

5.2.1 Chapter 2

With the Chapter 2 investigation, we generated a large toxicity data set and developed a high-throughput method for toxicity screening. Both of these accomplishments can be built upon. To start, we can use the data set obtained to start generating more complex toxicity models. In the past, we considered the simplest form of toxicity kinetics to describe the toxicity rate of a single CPA. However, with multi-CPA solutions, the toxicity kinetics are more complicated. As we have seen in Chapter 2, various multicomponent effects can be present, such as PG greatly increasing the toxicity of a mixture and Gly + FA solutions showing synergy. In a future work, we will build off of the simple toxicity kinetics described earlier to predict the toxicity rates of multi-CPA mixtures. Moving to the high-throughput method itself, our automated liquid handling methodology can continue to evolve. For a future work, we are designing a temperature-controlled platform that will allow us to conduct the same experiments discussed in this work but at varied temperature. With this capability, we can also consider performing complex CPA addition and removal protocols entirely with our automated liquid handler. Finally, we can use the method to screen vast chemical libraries (both single CPAs and mixtures) for toxicity—chemicals that are otherwise not considered conventional CPAs. Overall, we have developed a sound high-throughput pipeline that will further strengthen the toxicity kinetic modeling of the toxicity cost function.

5.2.2 Chapter 3

Chapter 3 provided a sound framework for future tissue modeling endeavors. The model we put forth for the tissue regime seems to have a general applicability to tissues, since we were able to model two very different tissues in articular cartilage and pancreatic islets. This model sets the stage for more investigations of different tissues, such as decellularized heart valve and ovarian tissue, among others. We can move past making predictions for many different tissues, though. The model can be directly applied to our toxicity cost function framework for tissues, and we can start making predictions for the least toxic CPA addition and removal protocols for many tissues. Also, since the model accounts for so many tissue-based phenomena, it could potentially be crafted into an organ-based model. Of course, each organ is uniquely complex, but we could start building complex geometries where transport in the organ's tissue is governed by the model we have proposed. The model could be effectively linked with a vasculature model for perfusion applications. Altogether, our proposed model could have a big impact on the vitrification protocols of many tissues, while providing learnings for even more complex specimens.

5.2.3 Chapter 4

In Chapter 4, we explored the most complex specimen regime of organs by investigating porcine kidneys obtained from a slaughterhouse. Organs are immensely complex, and we just wanted to probe the regime by looking at some basic trends and developing some experimental methods that could inform future models. That being said, we do have data that can be used to inform a potential model. We can either use our mass change and volumetric flowrate change data from our EG perfusions, or we can use the CT data from our DMSO perfusions. An initial starting point for modeling would be the classic Krogh cylinder model. The model is straightforward to implement and can be informed by the data we already have. An interesting aspect of the Krogh cylinder model is a variable vasculature diameter which can be directly informed by our volumetric flowrate change data. Moving past the Krogh cylinder model, we could consider more rigorous modeling approaches if needed, such as implementing the tissue model discussed in Chapter 3 for perfusion modeling. On more of the experimental side, we could investigate ways to measure the concentration of other CPAs within an organ. Outside of DMSO, and limiting our approach to CT, we would have to investigate the use of contrast agents in our perfusate. Also, we can further our LDH assay study. Our assay can give an indication of osmotic damage within the kidney, but to fully move the toxicity cost function approach to the organ regime, we need some endpoint metric for assessing toxicity. One possibility is using the LDH assay for measuring toxicity as well. Overall, we have established experimental methods at the organ level that can be built upon for future toxicity cost function applications.

6. REFERENCES

[1] A. Abazari, J.A. Elliott, G.K. Law, L.E. McGann, and N.M. Jomha, A biomechanical triphasic approach to the transport of nondilute solutions in articular cartilage. Biophys J 97 (2009) 3054-64.

[2] A. Abazari, R.B. Thompson, J.A. Elliott, and L.E. McGann, Transport phenomena in articular cartilage cryopreservation as predicted by the modified triphasic model and the effect of natural inhomogeneities. Biophys J 102 (2012) 1284-93.

[3] M.B. Albro, N.O. Chahine, M. Caligaris, V.I. Wei, M. Likhitpanichkul, K.W. Ng, C.T. Hung, and G.A. Ateshian, Osmotic loading of spherical gels: a biomimetic study of hindered transport in the cell protoplasm. J Biomech Eng 129 (2007) 503-10.

[4] J. Ali, and J.N. Shelton, Design of vitrification solutions for the cryopreservation of embryos. J Reprod Fertil 99 (1993) 471-7.

[5] K.A. Almansoori, V. Prasad, J.F. Forbes, G.K. Law, L.E. McGann, J.A. Elliott, and N.M. Jomha, Cryoprotective agent toxicity interactions in human articular chondrocytes. Cryobiology 64 (2012) 185-91.

[6] G.A. Ateshian, M.A. Soltz, R.L. Mauck, I.M. Basalo, C.T. Hung, and W.M. Lai, The role of osmotic pressure and tension-compression nonlinearity in the frictional response of articular cartilage. Transport in Porous Media 50 (2003) 5-33.

[7] K. Aukland, and G. Nicolaysen, Interstitial Fluid Volume - Local Regulatory Mechanisms. Physiological Reviews 61 (1981) 556-643.

[8] J.M. Baust, Properties of Cells and Tissues Influencing Preservation Outcome: Molecular Basis of Preservation-Induced Cell Death in: J.G. Baust, and J.M. Baust, (Eds.), Advances in Biopreservation, CRC Press, Boca Raton, 2007, pp. 63-87.

[9] A.F. Beier, J.C. Schulz, D. Dorr, A. Katsen-Globa, A. Sachinidis, J. Hescheler, and H. Zimmermann, Effective surface-based cryopreservation of human embryonic stem cells by vitrification. Cryobiology 63 (2011) 175-85.

[10] C.T. Benson, C. Liu, D.Y. Gao, E.S. Critser, J.D. Benson, and J.K. Critser, Hydraulic conductivity (Lp) and its activation energy (Ea), cryoprotectant agent permeability (Ps) and its Ea, and reflection coefficients (sigma) for golden hamster individual pancreatic islet cell membranes. Cryobiology 37 (1998) 290-9.

[11] J.D. Benson, A.J. Kearsley, and A.Z. Higgins, Mathematical optimization of procedures for cryoprotectant equilibration using a toxicity cost function. Cryobiology 64 (2012) 144-151.

[12] J.D. Benson, C.T. Benson, and J.K. Critser, Mathematical model formulation and validation of water and solute transport in whole hamster pancreatic islets. Math Biosci 254 (2014) 64-75.

[13] J.D. Benson, A.Z. Higgins, K. Desai, and A. Eroglu, A toxicity cost function approach to optimal CPA equilibration in tissues. Cryobiology 80 (2018) 144-155.

[14] S. Bhowmick, C.A. Khamis, and J.C. Bischof, Response of a liver tissue slab to a hyperosmotic sucrose boundary condition: Microscale cellular and vascular level effects. Annals of the New York Academy of Sciences 858 (1998) 147-162.

[15] N. Bleisinger, R. Dittrich, O. Strahl, R. Brauweiler, I. Hoffmann, M.W. Beckmann, and T. Volk, Me2SO perfusion time for whole-organ cryopreservation can be shortened: Results of micro-computed tomography monitoring during Me2SO perfusion of rat hearts. Plos One 15 (2020).

[16] G. Bloom, and J.A. Johnson, A Model for Osmotically Induced Weight Transient in the Isolated Rabbit Heart. Microvascular Research 22 (1981) 64-79.

[17] M.F. Blum, Q. Liu, B. Soliman, P. Dreher, T. Okamoto, E.D. Poggio, D.A. Goldfarb, W.M. Baldwin, 3rd, and C. Quintini, Comparison of normothermic and hypothermic perfusion in porcine kidneys donated after cardiac death. J Surg Res 216 (2017) 35-45.

[18] P. Bogacki, and L.F. Shampine, A 3(2) Pair of Runge - Kutta Formulas. Applied Mathematics Letters 2 (1989) 321-325.

[19] R.E. Bulger, Composition of renal medullary tissue. Kidney Int 31 (1987) 556-61.

[20] K. Carling, Resistant outlier rules and the non-Gaussian case. Computational Statistics & Data Analysis 33 (2000) 249-258.

[21] W.D. Comper, and T.C. Laurent, Physiological Function of Connective-Tissue Polysaccharides. Physiological Reviews 58 (1978) 255-315.

[22] R.M. Cordeiro, S. Stirling, G.M. Fahy, and J.P. de Magalhaes, Insights on cryoprotectant toxicity from gene expression profiling of endothelial cells exposed to ethylene glycol. Cryobiology 71 (2015) 405-12.

[23] A. Corral, M. Balcerzyk, A. Parrado-Gallego, I. Fernandez-Gomez, D.R. Lamprea, A. Olmo, and R. Risco, Assessment of the cryoprotectant

concentration inside a bulky organ for cryopreservation using X-ray computed tomography. Cryobiology 71 (2015) 419-31.

[24] A. Corral, M. Balcerzyk, M. Gallardo, C.A. Amorim, A. Parrado-Gallego, and R. Risco, An optimized controlled rate slow cooling protocol for bovine ovarian tissue cryopreservation by means of X-ray computed tomography. Theriogenology 119 (2018) 183-188.

[25] A. Corral, M. Clavero, M. Gallardo, M. Balcerzyk, C.A. Amorim, A. Parrado-Gallego, M.M. Dolmans, F. Paulini, J. Morris, and R. Risco, Ovarian tissue cryopreservation by stepped vitrification and monitored by X-ray computed tomography. Cryobiology 81 (2018) 17-26.

[26] W.L. Corwin, J.M. Baust, J.G. Baust, and R.G. Van Buskirk, The unfolded protein response in human corneal endothelial cells following hypothermic storage: Implications of a novel stress pathway. Cryobiology 63 (2011) 46-55.

[27] Z.F. Cui, R.C. Dykhuizen, R.M. Nerem, and A. Sembanis, Modeling of cryopreservation of engineered tissues with one-dimensional geometry. Biotechnology Progress 18 (2002) 354-361.

[28] A.F. Davidson, J.D. Benson, and A.Z. Higgins, Mathematically optimized cryoprotectant equilibration procedures for cryopreservation of human oocytes. Theoretical Biology and Medical Modelling 11 (2014).

[29] A.F. Davidson, C. Glasscock, D.R. McClanahan, J.D. Benson, and A.Z. Higgins, Toxicity Minimized Cryoprotectant Addition and Removal Procedures for Adherent Endothelial Cells. PLoS One 10 (2015) e0142828.

[30] R.C. De Freitas, K.R. Diller, C.A. Lachenbruch, and F.A. Merchant, Network thermodynamic model of coupled transport in a multicellular tissue the islet of Langerhans. Annals of the New York Academy of Sciences 858 (1998) 191-204.

[31] R.J. de Vries, M. Yarmush, and K. Uygun, Systems engineering the organ preservation process for transplantation. Curr Opin Biotechnol 58 (2019) 192-201.

[32] R.V. Devireddy, Predicted permeability parameters of human ovarian tissue cells to various cryoprotectants and water. Molecular Reproduction and Development 70 (2005) 333-343.

[33] B. Ekser, R.S. Mangus, C.A. Kubal, J.A. Powelson, J.A. Fridell, and W.C. Goggins, Excellent outcomes in combined liver-kidney transplantation: Impact of kidney donor profile index and delayed kidney transplantation. Liver Transpl 24 (2018) 222-232.

[34] H.M. El-Shewy, W.F. Kendall, M. Darrabie, B.H. Collins, and E.C. Opara, Polyvinyl pyrrolidone: A novel cryoprotectant in islet cell cryopreservation. Cell Transplantation 13 (2004) 237-243.

[35] J.A.W. Elliott, R.C. Prickett, H.Y. Elmoazzen, K.R. Porter, and L.E. McGann, A multisolute osmotic virial equation for solutions of interest in biology. Journal of Physical Chemistry B 111 (2007) 1775-1785.

[36] H.Y. Elmoazzen, A. Poovadan, G.K. Law, J.A. Elliott, L.E. McGann, and N.M. Jomha, Dimethyl sulfoxide toxicity kinetics in intact articular cartilage. Cell Tissue Bank 8 (2007) 125-33.

[37] H.Y. Elmoazzen, J.A. Elliott, and L.E. McGann, Osmotic transport across cell membranes in nondilute solutions: a new nondilute solute transport equation. Biophys J 96 (2009) 2559-71.

[38] M.D. Fahmy, K.A. Almansoori, L. Laouar, V. Prasad, L.E. McGann, J.A. Elliott, and N.M. Jomha, Dose-injury relationships for cryoprotective agent injury to human chondrocytes. Cryobiology 68 (2014) 50-6.

[39] G.M. Fahy, and D.R. Macfarlane, Recent Progress toward Vitrification of Kidneys. Cryobiology 19 (1982) 668-669.

[40] G.M. Fahy, Cryoprotectant Toxicity - Biochemical or Osmotic. Cryo-Letters 5 (1984) 79-90.

[41] G.M. Fahy, D.R. MacFarlane, C.A. Angell, and H.T. Meryman, Vitrification as an approach to cryopreservation. Cryobiology 21 (1984) 407-26.

[42] G.M. Fahy, The Relevance of Cryoprotectant Toxicity to Cryobiology. Cryobiology 23 (1986) 1-13.

[43] G.M. Fahy, T.H. Lilley, H. Linsdell, M.S. Douglas, and H.T. Meryman, Cryoprotectant toxicity and cryoprotectant toxicity reduction: in search of molecular mechanisms. Cryobiology 27 (1990) 247-68.

[44] G.M. Fahy, J. Saur, and R.J. Williams, Physical Problems with the Vitrification of Large Biological-Systems. Cryobiology 27 (1990) 492-510.

[45] G.M. Fahy, C. da Mouta, L. Tsonev, B.S. Khirabadi, P. Mehl, and H.T. Meryman, Cellular Injury Associated with Organ Cryopreservation: Chemical Toxicity and Cooling Injury. in: J.J. Lemasters, and C. Oliver, (Eds.), Cell Biology of Trauma, CRC Press, Boca Raton, 1995, pp. 333-356.

[46] G.M. Fahy, B. Wowk, J. Wu, and S. Paynter, Improved vitrification solutions based on the predictability of vitrification solution toxicity. Cryobiology 48 (2004) 22-35.

[47] G.M. Fahy, B. Wowk, J. Wu, J. Phan, C. Rasch, A. Chang, and E. Zendejas, Cryopreservation of organs by vitrification: perspectives and recent advances. Cryobiology 48 (2004) 157-178.

[48] G.M. Fahy, B. Wowk, and J. Wu, Cryopreservation of complex systems: The missing link in the regenerative medicine supply chain. Rejuvenation Research 9 (2006) 279-291.

[49] G.M. Fahy, B. Wowk, R. Pagotan, A. Chang, J. Phan, B. Thomson, and L. Phan, Physical and biological aspects of renal vitrification. Organogenesis 5 (2009) 167-75.

[50] G.M. Fahy, Cryoprotectant toxicity neutralization. Cryobiology 60 (2010) S45-53.

[51] G.M. Fahy, and B. Wowk, Principles of Cryopreservation by Vitrification. in: W.F. Wolkers, and H. Oldenhof, (Eds.), Cryopreservation and Freeze-Drying Protocols, Springer, 2015.

[52] G.M. Fahy, Cooling injury in rabbit kidneys below -22^{o}C. Cryobiology 81 (2018) 217-218.

[53] J.P. Faure, I. Petit, K. Zhang, D. Dutheil, C. Doucet, F. Favreau, M. Eugene, J.M. Goujon, J.P. Tillement, G. Mauco, A. Vandewalle, and T. Hauet, Protective roles of polyethylene glycol and trimetazidine against cold ischemia and reperfusion injuries of pig kidney graft. Am J Transplant 4 (2004) 495-504.

[54] R.M. Forbes, A.R. Cooper, and H.H. Mitchell, The composition of the adult human body as determined by chemical analysis. J Biol Chem 203 (1953) 359-66.

[55] M. Frigge, D.C. Hoaglin, and B. Iglewicz, Some Implementations of the Boxplot. American Statistician 43 (1989) 50-54.

[56] A.K. Fry, and A.Z. Higgins, Measurement of Cryoprotectant Permeability in Adherent Endothelial Cells and Applications to Cryopreservation. Cellular and Molecular Bioengineering 5 (2012) 287-298.

[57] R.M. Furzeland, A Survey of the Formulation and Solution of Free and Moving Boundary (Stefan) Problems, Brunel University, Uxbridge, United Kingdom, 1977.

[58] R.M. Furzeland, A Comparative Study of Numerical Methods for Moving Boundary Problems. IMA Journal of Applied Mathematics 26 (1980) 411-429.

[59] D.Y. Gao, J. Liu, C. Liu, L.E. Mcgann, P.F. Watson, F.W. Kleinhans, P. Mazur, E.S. Critser, and J.K. Critser, Prevention of Osmotic Injury to Human

Spermatozoa during Addition and Removal of Glycerol. Human Reproduction 10 (1995) 1109-1122.

[60] K.D. Gardner, Jr., and J.M. Vierling, Solids, water, and solutes in papillary region of the rat kidney. Am J Physiol 217 (1969) 58-64.

[61] S. Giwa, J.K. Lewis, L. Alvarez, R. Langer, A.E. Roth, G.M. Church, J.F. Markmann, D.H. Sachs, A. Chandraker, J.A. Wertheim, M. Rothblatt, E.S. Boyden, E. Eidbo, W.P.A. Lee, B. Pomahac, G. Brandacher, D.M. Weinstock, G. Elliott, D. Nelson, J.P. Acker, K. Uygun, B. Schmalz, B.P. Weegman, A. Tocchio, G.M. Fahy, K.B. Storey, B. Rubinsky, J. Bischof, J.A.W. Elliott, T.K. Woodruff, G.J. Morris, U. Demirci, K.G.M. Brockbank, E.J. Woods, R.N. Ben, J.G. Baust, D.Y. Gao, B. Fuller, Y. Rabin, D.C. Kravitz, M.J. Taylor, and M. Toner, The promise of organ and tissue preservation to transform medicine. Nature Biotechnology 35 (2017) 530-542.

[62] A.I. Glazar, S.F. Mullen, J. Liu, J.D. Benson, J.K. Critser, E.L. Squires, and J.K. Graham, Osmotic tolerance limits and membrane permeability characteristics of stallion spermatozoa treated with cholesterol. Cryobiology 59 (2009) 201-6.

[63] C. Grosse-Siestrup, V. Unger, M. Meissler, S. Nagel, A. Wussow, C. Peiser, A. Fischer, R. Schmitt, and D.A. Groneberg, Hemoperfused isolated porcine slaughterhouse kidneys as a valid model for pharmacological studies. Journal of Pharmaceutical Sciences 92 (2003) 1147-1154.

[64] J. Han, B. Sydykov, H. Yang, H. Sieme, H. Oldenhof, and W.F. Wolkers, Spectroscopic monitoring of transport processes during loading of ovarian tissue with cryoprotective solutions. Sci Rep 9 (2019) 15577.

[65] S.M. Hanson, S. Ekins, and J.D. Chodera, Modeling error in experimental assays using the bootstrap principle: understanding discrepancies between assays using different dispensing technologies. Journal of Computer-Aided Molecular Design 29 (2015) 1073-1086.

[66] T. Hauet, J.M. Goujon, H. Baumert, I. Petit, M. Carretier, M. Eugene, and A. Vandewalle, Polyethylene glycol reduces the inflammatory injury due to cold ischemia/reperfusion in autotransplanted pig kidneys. Kidney Int 62 (2002) 654-67.

[67] Y.M. He, and R.V. Devireddy, An inverse approach to determine solute and solvent permeability parameters in artificial tissues. Annals of Biomedical Engineering 33 (2005) 709-718.

[68] M. Hezavehei, M. Sharafi, H.M. Kouchesfahani, R. Henkel, A. Agarwal, V. Esmaeili, and A. Shahverdi, Sperm cryopreservation: A review on current molecular cryobiology and advanced approaches. Reproductive Biomedicine Online 37 (2018) 327-339.

[69] M. Hill, and M. Davis, Local Control of Microvascular Perfusion, Morgan & Claypool Life Sciences, 2013.

[70] A.R. Hipkiss, Proteotoxicity and the Contrasting Effects of Oxaloacetate and Glycerol on Caenorhbditis elegans Life Span: A Role for Methylglyoxal? Rejuvenation Research 13 (2010) 547-551.

[71] D.C. Hoaglin, B. Iglewicz, and J.W. Tukey, Performance of Some Resistant Rules for Outlier Labeling. Journal of the American Statistical Association 81 (1986) 991-999.

[72] S.A. Hodson, Corneal stromal swelling. Progress in Retinal and Eye Research 16 (1997) 99-116.

[73] S.W. Jacob, and J.C. de la Torre, Pharmacology of dimethyl sulfoxide in cardiac and CNS damage. Pharmacological Reports 61 (2009) 225-235.

[74] N.M. Jomha, G.K. Law, A. Abazari, K. Rekieh, J.A.W. Elliott, and L.E. McGann, Permeation of several cryoprotectant agents into porcine articular cartilage. Cryobiology 58 (2009) 110-114.

[75] N.M. Jomha, A.D. Weiss, J. Fraser Forbes, G.K. Law, J.A. Elliott, and L.E. McGann, Cryoprotectant agent toxicity in porcine articular chondrocytes. Cryobiology 61 (2010) 297-302.

[76] N.M. Jomha, J.A. Elliott, G.K. Law, B. Maghdoori, J.F. Forbes, A. Abazari, A.B. Adesida, L. Laouar, X. Zhou, and L.E. McGann, Vitrification of intact human articular cartilage. Biomaterials 33 (2012) 6061-8.

[77] J.O.M. Karlsson, A.I. Younis, A.W.S. Chan, K.G. Gould, and A. Eroglu, Permeability of the Rhesus Monkey Oocyte Membrane to Water and Common Cryoprotectants. Molecular Reproduction and Development 76 (2009) 321-333.

[78] M.R. Kellen, and J.B. Bassingthwaighte, Transient transcapillary exchange of water driven by osmotic forces in the heart. Am J Physiol Heart Circ Physiol 285 (2003) H1317-31.

[79] F.W. Kleinhans, Membrane permeability modeling: Kedem-Katchalsky vs a two-parameter formalism. Cryobiology 37 (1998) 271-289.

[80] V.A. Kot, Solution of the Classical Stefan Problem: Neumann Condition. Journal of Engineering Physics and Thermophysics 90 (2017) 889-917.

[81] S. Kutluay, A.R. Bahadir, and A. Ozdes, The numerical solution of one-phase classical Stefan problem. Journal of Computational and Applied Mathematics 81 (1997) 135-144.

[82] W.M. Lai, J.S. Hou, and V.C. Mow, A Triphasic Theory for the Swelling and Deformation Behaviors of Articular-Cartilage. Journal of Biomechanical Engineering-Transactions of the Asme 113 (1991) 245-258.

[83] D. Lansky, Validation of bioassays for quality control. Dev Biol Stand 97 (1999) 157-68.

[84] D. Lansky, Strip-plot designs, mixed models, and comparisons between linear and non-linear models for microtitre plate bioassays. Dev Biol (Basel) 107 (2002) 11-23.

[85] A. Lawson, H. Ahmad, and A. Sambanis, Cytotoxicity effects of cryoprotectants as single-component and cocktail vitrification solutions. Cryobiology 62 (2011) 115-22.

[86] A. Lawson, I.N. Mukherjee, and A. Sambanis, Mathematical modeling of cryoprotectant addition and removal for the cryopreservation of engineered or natural tissues. Cryobiology 64 (2012) 1-11.

[87] D. Lee, and L.C. Chang, Development of the pipetting error sensor. Sensors and Actuators B-Chemical 119 (2006) 150-158.

[88] K. Lee, K. Jeoung, S.H. Kim, Y.B. Ji, H. Son, Y. Choi, Y.M. Huh, J.S. Suh, and S.J. Oh, Measuring water contents in animal organ tissues using terahertz spectroscopic imaging. Biomed Opt Express 9 (2018) 1582-1589.

[89] H. Levitin, A. Goodman, G. Pigeon, and F.H. Epstein, Composition of the renal medulla during water diuresis. J Clin Invest 41 (1962) 1145-51.

[90] J.K. Lewis, J.C. Bischof, I. Braslavsky, K.G.M. Brockbank, G.M. Fahy, B.J. Fuller, Y. Rabin, A. Tocchio, E.J. Woods, B.G. Wowk, J.P. Acker, and S. Giwa, The Grand Challenges of Organ Banking: Proceedings from the first global summit on complex tissue cryopreservation. Cryobiology 72 (2016) 169-182.

[91] B.K. Lundholt, K.M. Scudder, and L. Pagliaro, A simple technique for reducing edge effect in cell-based assays. J Biomol Screen 8 (2003) 566-70.

[92] R.E. Lusianti, and A.Z. Higgins, Continuous removal of glycerol from frozen-thawed red blood cells in a microfluidic membrane device. Biomicrofluidics 8 (2014) 054124.

[93] K. Lyman, D. Fisher, Y. Han, and D.M. Chetkovich, A Novel Method for Reducing Human Pipetting Errors. Journal of Medical Laboratory and Diagnosis 6 (2015) 36-40.

[94] R. Malpique, R. Tostoes, A.F. Beier, M. Serra, C. Brito, J.C. Schulz, P. Bjorquist, H. Zimmermann, and P.M. Alves, Surface-based cryopreservation strategies for

human embryonic stem cells: a comparative study. Biotechnol Prog 28 (2012) 1079-87.

[95] L.E. McGann, M. Stevenson, K. Muldrew, and N. Schachar, Kinetics of osmotic water movement in chondrocytes isolated from articular cartilage and applications to cryopreservation. J Orthop Res 6 (1988) 109-15.

[96] A.R. MireSluis, T. Gerrard, R.G. Das, A. Padilla, and R. Thorpe, Biological assays: Their role in the development and quality control of recombinant biological medicinal products. Biologicals 24 (1996) 351-362.

[97] V. Mow, and X.E. Guo, Mechano-electrochemical properties of articular cartilage: Their inhomogeneities and anisotropies. Annual Review of Biomedical Engineering 4 (2002) 175-209.

[98] I.N. Mukherjee, Y.C. Song, and A. Sambanis, Cryoprotectant delivery and removal from murine insulinomas at vitrification-relevant concentrations. Cryobiology 55 (2007) 10-18.

[99] I.N. Mukherjee, Y. Li, Y.C. Song, R.C. Long, and A. Sambanis, Cryoprotectant transport through articular cartilage for long-term storage: experimental and modeling studies. Osteoarthritis and Cartilage 16 (2008) 1379-1386.

[100] N. Nagy, A. de la Zerda, G. Kaber, P.Y. Johnson, K.H. Hu, M.J. Kratochvil, K. Yadava, W. Zhao, Y. Cui, G. Navarro, J.P. Annes, T.N. Wight, S.C. Heilshorn, P.L. Bollyky, and M.J. Butte, Hyaluronan content governs tissue stiffness in pancreatic islet inflammation. J Biol Chem 293 (2018) 567-578.

[101] P.S. Nobel, The Boyle-Van't Hoff relation. J Theor Biol 23 (1969) 375-9.

[102] A.U. Parman, Quantitation of isolated rat islets of Langerhans on the basis of deoxyribonucleic acid content under metabolic conditions of altered protein synthesis. J Histochem Cytochem 23 (1975) 187-93.

[103] D.E. Pegg, and J. Farrant, Vascular resistance and edema in the isolated rabbit kidney perfused with a cell-free solution. Cryobiology 6 (1969) 200-10.

[104] D.E. Pegg, B. Rubinsky, M.P. Diaper, and C.Y.C. Lee, Analysis of the Introduction and Removal of Glycerol in Rabbit Kidneys Using a Krogh Cylinder Model. Cryobiology 23 (1986) 150-160.

[105] D.E. Pegg, and A.M. Karow, The Biophysics of Organ Cryopreservation, Springer, Boston, MA, 1988.

[106] M.E. Pero, G. Zullo, L. Esposito, A. Iannuzzi, P. Lombardi, C. De Canditiis, G. Neglia, and B. Gasparrini, Inhibition of apoptosis by caspase inhibitor Z-VAD-FMK improves cryotolerance of in vitro derived bovine embryos. Theriogenology 108 (2018) 127-135.

[107] E. Porcu, P. Ciotti, and S. Venturoli, Handbook of Human Oocyte Cryopreservation, Cambridge University Press, Cambridge, United Kingdom, 2012.

[108] I.C. Post, M.C. Dirkes, M. Heger, R. Bezemer, J. van 't Leven, and T.M. van Gulik, Optimal flow and pressure management in machine perfusion systems for organ preservation. Ann Biomed Eng 40 (2012) 2698-707.

[109] R.F. Reinoso, B.A. Telfer, and M. Rowland, Tissue water content in rats measured by desiccation. J Pharmacol Toxicol Methods 38 (1997) 87-92.

[110] R.L. Rivers, J.A. McAteer, J.L. Clendenon, B.A. Connors, A.P. Evan, and J.C. Williams, Jr., Apical membrane permeability of MDCK cells. Am J Physiol 271 (1996) C226-34.

[111] P.J. Roache, Perspective - a Method for Uniform Reporting of Grid Refinement Studies. Journal of Fluids Engineering-Transactions of the Asme 116 (1994) 405-413.

[112] P.J. Roache, Quantification of uncertainty in computational fluid dynamics. Annual Review of Fluid Mechanics 29 (1997) 123-160.

[113] K.A. Rodriguez-Wallberg, T. Tanbo, H. Tinkanen, A. Thurin-Kjellberg, E. Nedstrand, M.L. Kitlinski, K.T. Macklon, E. Ernst, J. Fedder, A. Tiitinen, L. Morin-Papunen, S. Einarsson, V. Jokimaa, M. Hippelainen, M. Lood, J. Gudmundsson, J.I. Olofsson, and C.Y. Andersen, Ovarian tissue cryopreservation and transplantation among alternatives for fertility preservation in the Nordic countries - compilation of 20 years of multicenter experience. Acta Obstetricia Et Gynecologica Scandinavica 95 (2016) 1015-1026.

[114] B. Rubinsky, and E.G. Cravalho, Transient Mass-Transfer Processes during the Perfusion of a Biological Organ with a Cryophylactic Agent Solution. Cryobiology 19 (1982) 70-82.

[115] J. Saragusty, and A. Arav, Current progress in oocyte and embryo cryopreservation by slow freezing and vitrification. Reproduction 141 (2011) 1-19.

[116] D. Savitz, and A.K. Solomon, Tracer determinations of human red cell membrane permeability to small nonelectrolytes. J Gen Physiol 58 (1971) 259-66.

[117] B. Schlain, H.S. Jethwa, M. Subramanyam, K. Moulder, B. Bhatt, and M. Molloy, Designs for bioassays with plate location effects. Biopharm-the Applied Technologies of Biopharmaceutical Development 14 (2001) 40-44.

[118] Z. Shaozhi, and D.E. Pegg, Analysis of the permeation of cryoprotectants in cartilage. Cryobiology 54 (2007) 146-53.

[119] N. Shardt, K.K. Al-Abbasi, H. Yu, N.M. Jomha, L.E. McGann, and J.A.W. Elliott, Cryoprotectant kinetic analysis of a human articular cartilage vitrification protocol. Cryobiology 73 (2016) 80-92.

[120] S.J. Silber, M. DeRosa, S. Goldsmith, Y.T. Fan, L. Castleman, and J. Melnick, Cryopreservation and transplantation of ovarian tissue: results from one center in the USA. Journal of Assisted Reproduction and Genetics 35 (2018) 2205-2213.

[121] Y.C. Song, B.S. Khirabadi, F. Lightfoot, K.G.M. Brockbank, and M.J. Taylor, Vitreous cryopreservation maintains the function of vascular grafts. Nature Biotechnology 18 (2000) 296-299.

[122] E.A. Szurek, and A. Eroglu, Comparison and avoidance of toxicity of penetrating cryoprotectants. PLoS ONE 6 (2011) e27604.

[123] A.D. Theocharis, M.E. Tsara, N. Papageorgacopoulou, D.D. Karavias, and D.A. Theocharis, Pancreatic carcinoma is characterized by elevated content of hyaluronan and chondroitin sulfate with altered disaccharide composition. Biochimica Et Biophysica Acta-Molecular Basis of Disease 1502 (2000) 201-206.

[124] R. Todd Allen, C.M. Robertson, F.L. Harwood, T. Sasho, S.K. Williams, A.C. Pomerleau, and D. Amiel, Characterization of mature vs aged rabbit articular cartilage: analysis of cell density, apoptosis-related gene expression and mechanisms controlling chondrocyte apoptosis. Osteoarthritis Cartilage 12 (2004) 917-23.

[125] J.W. Tukey, Exploratory Data Analysis, Addison-Wesley, Reading, MA, 1977.

[126] V. Unger, C. Grosse-Siestrup, C. Fehrenberg, A. Fischer, M. Meissler, and D.A. Groneberg, Reference values and physiological characterization of a specific isolated pig kidney perfusion model. J Occup Med Toxicol 2 (2007).

[127] A. Vasquez-Rivera, K.K. Sommer, H. Oldenhof, A.Z. Higgins, K.G.M. Brockbank, A. Hilfiker, and W.F. Wolkers, Simultaneous monitoring of different vitrification solution components permeating into tissues. Analyst 143 (2018) 420-428.

[128] H.K. Versteeg, and W. Malalasekera, An Introduction to Computational Fluid Dynamics, Pearson Education, Harlow, England, 2007.

[129] A.M. Vian, and A.Z. Higgins, Membrane permeability of the human granulocyte to water, dimethyl sulfoxide, glycerol, propylene glycol and ethylene glycol. Cryobiology 68 (2014) 35-42.

[130] V. Vuthiphandchai, B. Pengpun, and S. Nimrat, Effects of cryoprotectant toxicity and temperature sensitivity on the embryos of black tiger shrimp (Penaeus monodon). Aquaculture 246 (2005) 275-284.

[131] A. Walzl, N. Kramer, G. Mazza, M. Rosner, D. Falkenhagen, M. Hengstschlager, D. Schwanzer-Pfeiffer, and H. Dolznig, A Simple and Cost Efficient Method to Avoid Unequal Evaporation in Cellular Screening Assays, Which Restores Cellular Metabolic Activity. International Journal for Applied Science and Technology 2 (2012) 17-25.

[132] R.M. Warner, and A.Z. Higgins, Mathematical Modeling of Protectant Transport in Tissues. in: W.F. Wolkers, and H. Oldenhof, (Eds.), Cryopreservation and Freeze-Drying Protocols, Springer, 2020.

[133] E.J. Woods, M.A. Zieger, J.R. Lakey, J. Liu, and J.K. Critser, Osmotic characteristics of isolated human and canine pancreatic islets. Cryobiology 35 (1997) 106-13.

[134] K.Z. Wu, L. Laouar, R. Dong, J.A.W. Elliott, and N.M. Jomha, Evaluation of five additives to mitigate toxicity of cryoprotective agents on porcine chondrocytes. Cryobiology 88 (2019) 98-105.

[135] M. Wusteman, U. Rauen, J. Simmonds, N. Hunds, and D.E. Pegg, Reduction of cryoprotectant toxicity in cells in suspension by use of a sodium-free vehicle solution. Cryobiology 56 (2008) 72-79.

[136] X. Xu, Z. Cui, and J.P.G. Urban, Measurement of the chondrocyte membrane permeability to Me2SO, glycerol and 1,2-propanediol. Medical Engineering & Physics 25 (2003) 573-579.

[137] X. Xu, and Z.F. Cui, Modeling of the co-transport of cryoprotective agents in a porous medium as a model tissue. Biotechnology Progress 19 (2003) 972-981.

APPENDIX

A. Chapter 2: CPA Addition and Removal Step Design

CPA addition and removal steps were designed in order to stay within the osmotic tolerance limits as defined in our previous study [29]. The osmotic tolerance limits established in that study were conservatively set at a normalized osmotically active volume of 0.2 for the lower limit and 2 for the upper limit. In this study, we designed multi-step CPA equilibration methods using even more conservative limits for the lower and upper limit at 0.25 and 1.8, respectively. As such, we slightly modified the steps established in our previous work [29] to account for the more conservative limits. The time for each step (excluding the peak CPA exposure step) was minimized to the nearest 0.5 min while making sure that the osmotic tolerance limits were not crossed.

An osmotic tolerance limit refers to the normalized osmotically active volume of a cell that we do not want to cross, with the reference volume being that of the osmotically active volume of a cell in isotonic buffer. In order to calculate the normalized osmotically active volume of our cells through time, we used the classic two-parameter cell membrane transport model [29,79]:

$$\frac{d\bar{V}_w}{dt} = \frac{L_p A}{V_{w0}} \rho_w RT\left(M_s^i + M_n^i - M_s^e - M_n^e\right), \tag{A1}$$

$$\frac{d\bar{V}_s}{dt} = \frac{P_s A}{V_{w0}} \nu_s \rho_w \left(M_s^e - M_s^i\right), \tag{A2}$$

$$M_n^i = \frac{M_0}{\bar{V}_w}, \tag{A3}$$

$$M_s^i = \frac{\bar{V}_s}{\nu_s \rho_w \bar{V}_w}, \tag{A4}$$

where $\bar{V}_w$ and $\bar{V}_s$ are the normalized intracellular volumes of water and CPA, respectively, and the sum of the two gives the normalized osmotically active volume of a cell at time t. As such, we sought to satisfy the equation $0.25 \le \bar{V}_w + \bar{V}_s \le 1.8$ for all time. The effective water permeability ($L_pA/V_{w0} = 4.36 \text{ x } 10^{-8}$ [1/Pa/s]) and the effective glycerol permeability ($P_sA/V_{w0} = 6.02 \text{ x } 10^{-3}$ [1/s]) at 25 °C were found through a previous study [56]. Effective permeabilities were used for glycerol, as out of the five CPAs tested, glycerol has the lowest membrane permeability and causes the largest cell volume excursions. The remaining parameters in Equations A1-A4 are defined as follows: $\rho_w = 1$ kg/L is the density of water, R is the universal gas constant, T is the absolute temperature, $M_0 = 300 \text{ mOsm/kg}$ is the isotonic reference osmolality, $\nu_s = 0.071 \text{ L/mol}$ is the molar volume of glycerol, and M is osmolality with subscripts s and n referring to glycerol and the nonpermeating solute, respectively, and superscripts i and e referring to the intracellular and extracellular space, respectively.